COO-2107-12

CORRELATION OF SUBSTRUCTURE WITH MECHANICAL PROPERTIES OF PLASTICALLY DEFORMED REACTOR STRUCTURAL MATERIALS

Progress Report
for Period January 1, 1976 - June 30, 1977

J. Moteff

Materials Science and Metallurgical Engineering
University of Cincinnati
Cincinnati, Ohio 45221

July 8, 1977

Prepared For

THE U.S. ENERGY RESEARCH
AND DEVELOPMENT ADMINISTRATION

UNDER CONTRACT NO. E(11-1)-2107

DISTRIBUTION OF THIS DOCUMENT IS UNLIMITED

MASTER

DISCLAIMER

TABLE OF CONTENTS

Appendix A

Appendix B

Appendix C

ABSTRACT

Transmission electron microscopy used to evaluate the deformation (creep, fatigue and tensile) induced microstructure of 304 SS, Incoloy 800, 330 SS and three of the experimental alloys (E19, E23 and E36) obtained from the National Alloy Program clearly shows that the relationship between the subgrain size (λ) and the applied stress (σ) obeys the equation $\lambda = Ab\ (\sigma/E)^{-1}$ where A is a constant of the order of 4, b the Burgers rector and E is Young's modulus. Hot-hardness studies on 304 SS, 316 SS, Incoloy 800, 2 1/4 Cr - 1 Mo steels, 330 SS, Inconel 718, PE-16, Inconel 706, M-813 and the above three experimental alloys suggests that reasonable effective activation energies for creep may be obtained through the use of the hardness test as a strength microprobe tool. The ordering of the strength levels obtained through hot-hardness follows quite closely that obtained in tensile tests when that data are available.

I. OBJECTIVE

The objective of this program is to (a) evaluate the time, temperature and stress-dependent mechanical properties of reactor structural materials, (b) determine the relationship of these properties to the microstructure, (c) show the contribution of the microstructure to the internal stress fields and the subsequent influence on microcracking and the grain boundary sliding behavior during the normal plastic deformation at elevated temperatures and (d) demonstrate the relationship of the hot micro-hardness properties with the hot-tensile properties of a class of commercial and advanced alloys presently under investigation at other laboratories. Special consideration is being given to operating conditions typical of nuclear reactor applications, including the knowledge that radiation environment can influence the substructure of these metals, a circumstance which can lead to significant changes in the conventional mechanical property behavior.

II. INTRODUCTION

Transmission electron microscopy has been used as a primary tool to study the deformation substructure of reactor structural materials resulting from creep, fatigue and tensile testing at elevated temperatures. Complimentary work using optical microscopy, scanning electron microscopy and hot-hardness testing has been performed to characterize the deformation and failure behavior. New work was initiated on the Commercial, the Developmental and the Fundamental alloys being evaluated in the ational Alloy Developmental Program with particular attention on the application of hot-hardness measurement as a strength microprobe.

III. EXPERIMENTAL PROGRAM

The work at the University of Cincinnati has been contributed to "Mechanical Properties Test Data for Structural Materials Quarterly Progress Reports" of Oak Ridge National Laboratory, Documented as University of Cincinnati Quarterly or Annual Progress Reports and published in the technical journals. Papers have also been presented at technical society meetings. A listing of the University of Cincinnati past Progress Reports is given on page 13, and those papers published in technical journals on page 14 of this progress report. The quarterly progress efforts on this project since the last progress report COO-2107-11 dated March 15, 1976 for the time period ending December 31, 1975 are reported as Appendices A through F of this progress report.

Previously a number of specific subtasks have been delineated for work to be performed under this program on 304 and 316 stainless steel, Incoloy 800 and 2 1/4 Cr-1Mo steels. Experimental work on most of these have been completed and data analyses have been performed with the results formally submitted or in the process of being submitted for publication.

New work has been initiated during the last two contract years on alloys obtained from the National Alloy Development Program. A total of 8 Commercial Alloys and 14 Developmental and Experimental Alloys have been obtained from HEDL during anuary and February of 1976. Three of the Experimental Alloys (E19, E23 and E36) have been obtained in October, 1974. A listing of Alloys received is given in Table I. Information on recommended heat treatments on these alloys were received in May and August of 1976.

Creep-rupture and hot-hardness studies have been completed on the Experimental Alloys E19, E23 and E36 and the data presented in the Masters Thesis of C.G. Schmidt* in June, 1975. A total of fifteen (15) creep-rupture tests and subsequent TEM studies were performed on the three experimental alloys at test temperatures of 1100 (593) and 1200°F (649°C). Hot-hardness tests were also performed on the same alloys.

The results of the tests on the three experimental alloys are summarized as follows:

1. Hot hardness tests indicate that strength increases with nickel content for the alloys considered in this investigation. Due to the high strain rate involved, hot hardness tests are not always indicative of the performance of a material in the creep mode.
2. Activation energies for what is apparently the self-diffusion of iron and/or nickel were calculated from the hot hardness results using data points from tests above 0.6 T_m.
3. Substructure for the three alloys presently concerned indicated that,

$$\lambda = 4b \left(\frac{\sigma}{E}\right)^{-1}$$

---

*Creep Properties of Some Experimental Nickel-Iron Chromium Alloys, A thesis submitted to the Department of Materials Science and Metallurgical Engineering, College of Engineering, University of Cincinnati, Cincinnati, Ohio 45221, (1975). Note: C.G. Schmidt is now a Ph.D. Candidate at Stanford University

Dislocation density for the Fe-45Ni-15Cr and the Ni-15Cr alloy was found to follow the relation shown below,

$$\tau/G = 1.4 \times 10^{-4} + 0.8\, b \sqrt{\rho}$$

The Fe-20Ni-15Cr alloy did not have a consistent variation in dislocation density with stress. Misorientation angle slowly increased with strain.

4. Cell intercept size for unruptured specimens is significantly larger than that of ruptured ones which implies that cell size continues to decrease in the latter stages of creep.
5. A critical dislocation density for cell formation of 6×10^{9} cm^{-2} appears to exist for these alloys.
6. The fracture surfaces of the Fe-20Ni-15Cr and the Fe-45Ni-15Cr alloy specimens have a mixed mode of transgranular and intergranular fracture for the creep conditions discussed here. High stresses and/or low temperatures tend to produce a more transgranular fracture. The Ni-15Cr alloy fractured in a transgranular fashion for all creep tests conducted in this investigation.

More recent work on the microstructure-strength relationship has been completed on about 40 creep rupture specimens of 330 stainless steel in which one set (16 specimens) were used to determine the stress dependency and subsequent microstructure of these alloys at a temperature of 649°C and another set (14 speci-ens) were used to determine the development of the microstructure as a function of the creep-rupture life at a fixed temperature and stress level. In addition, about 50 A-286 creep-rupture specimens have been fabricated from a reference heat received from HEDL. Extensive creep-rupture testing has not been initiated on the A-286 specimens at the present time.

Hot-hardness experiments have been completed on the three Experimental Alloys E19, E23 and E36, several different heats of AISI 330 SS, several different heats of AISI 304 SS, AISI 316 SS, IN 706, IN 718, PE 16 and M-813. The hot-hardness equipment has been shut-down for about four (4) months for a complete overhaul. Vacuum leaks have been corrected to improve the vacuum capabilities by our one order of magnitude. All O-rings and flange gaskets have been replaced and the indentor mechanisms re-aligned and modified so that indentations can be made more uniform. The equipment is now back in operation and a few samples are rechecked before proceeding with the testing of additional new specimens.

Work on the observation and the preliminary evaluation of the dislocation substructure of the fatigue specimens of Incoloy 800 were completed. Incoloy 800 push-pull fatigue specimens were examined after being tested at various test conditions at 538, 649, 704 and 760°C. Substructure parameters such as cell or subgrain intercept size, dislocation density, were evaluated and correlated with the observed fatigue properties. Cells or subgrains were observed to form Incoloy 800 after LCF at all testing temperatures. The subboundary intercept size and the dislocation density were found to be related to both the saturation stress and the plastic strain range. Subboundaries were also found to lie on the low index crystallographic planes with mixed, tilt and twist nature. Details of this work are reported in Appendix A and B.

A set of A-286 specimens was solid-solution annealed at 900°C for 2 hours and aged at 720°C for various times. It was found that rapid hardening occurs during the initial ageing period, the hardness increasing slowly thereafter (Appendix B).

A constant load creep rupture test was performed on AISI 330 stainless steel at 649°C with an applied stress of 30,000 psi. The minimum creep rate was 1.04×10^{-4} $\sec^{-1}$ and the rupture life and the rupture strain were 29.6 hours and 64.3%, respectively (Appendix B).

A comparison of the hot-hardness values of aged A-286 and solutioned AISI 330 stainless steel shows that A-286 is about three times harder than 330 SS in the temperature region of 200 to 900°C (Appendix B).

Creep-rupture tests were performed on AISI 330 stainless steel at 701°C with an applied stress of 20,000, 30,000, 35,000 and 40,000 psi, respectively. The minimum creep rate varied from 0.60 to 83.7% hr., and the rupture life ranged from 33.65 to 0.25 hours with the increasing applied stress. A limited amount of TEM observation has been performed on two of the rupture specimens: cells and subgrains were observed in the specimens tested at 40,000 psi and 20,000 psi, respectively (Appendix C).

An experimental plan has been set up to study the substructural developments of AISI 330 SS during creep tests. The creep tests will be interrupted at various levels of creep strain, and the substructures will be examined by TEM. The aim of this experiment is to study the mechanisms of subgrain/cell formation (Appendix C).

Based on the hot-hardness data of AISI 330 SS, the apparent activation energies for indentation hardness and the activation energy for creep were calculated. As with other metals, the apparent activation energy for indentation hardness of this material (7,940 cal/mole) is an order of magnitude lower than the activation energy for creep (93,400 cal/mole) (Appendix C).

Hot-hardness tests were performed on four heats of 2 1/4 Cr-1 Mo steel containing various amounts of carbon, and the results were compared with the tensile strength at six temperatures from room temperature to 565°C. The correlation is excellent for the high carbon and the commercial steels and good or fair for the medium and low carbon steels (Appendix C).

A controlled-atmosphere, direct-loading creep testing machine has been constructed for the grain boundary sliding experiments. A preliminary result obtained from AISI 304 stainless steel tested at 750°C with an applied stress of 9,000 psi is in agreement with the data which has been reported in the literature. More detailed experiments are being planned (Appendix C).

Hot-hardness tests were performed on AISI 310 stainless steel and Inconel 718 at temperatures of R.T. ∿1200°C and 900~1200°C, respectively. Compared to AISI 330 stainless steel, both AISI 310 stainless steel and Inconel 718 are lower in hardness values at all temperatures investigated, however, their hardness curves have the similar characteristics as AISI 330 stainless steel. The activation energy for creep calculated rom the hot-hardness data is 85 kcal/mole for AISI 310 stainless steel and 64 kcal/mole for Inconel 718 (Appendix D).

As an effort to investigate the mechanisms of subgrain/cell ormation during creep deformation, a series of creep tests were conducted on AISI 330 stainless steel at 652°C with an applied stress of 35 ksi for various strains (times), including three stress-rupture tests. These tests were reproducible with less than 1 percent deviation in the total strain and are considered to be suitable for the detailed microstructure studies. Preliminary TEM and SEM observations on one of the ruptured specimens revealed an ill-defined cellular structure containing precipitates and a transgranular fracture surface, respectively (Appendix D).

Fatigue crack characteristics were investigated on AISI 304 stainless steel fatigue-tested at 649°C to different fractions of the fatigue life and to failure. The striation density was determined from SEM micrographs of the fractured surface, and the number of cycles for crack propagation and the number of cycles to initiate a crack of one grain diameter length were calculated. Optical microscopy on the specimens tested to various fractions of the fatigue life revealed a crack at various stages of crack initiation and propagation periods. The crack lengths determined from the optical microscope agreed with the values obtained from the SEM technique. Finally, the microhardness values obtained from the interrupted specimens show good agreement with the stress amplitude measurements and the substructure development (Appendix D).

As a continuation of the creep-substructure study on AISI 30 stainless steel, stress-rupture tests have been completed on three more specimens since the last progress report was submitted, and one long term test is presently in progress at 600°C ith an applied stress of 20 ksi. Preliminary analyses of the creep data compiled up to the present time show the following:

$$\Delta \bar{H}_c = 100 \text{ kcal/mole}$$

$$n = 7.4 \text{ at } 701°C$$

$$n = 7.1 \text{ at } 800°C$$

These numbers should be considered as tentative because of the limited number of datum points used for the calculation. However, it is interesting to note that the activation energy for creep, 100 kcal/mole, is in reasonable agreement with the value obtained from the hot-hardness data on the same material, i.e. 93 kcal/mole as reported in the last progress report. Finally, a limited study on the cracking behavior of this material has been initiated (Appendix D).

As a continuation of the study on subgrain/cell development during creep deformation, another series of creep tests--interrupted at various creep stages including one to the rupture--were conducted on AISI 330 SS at 652°C with an applied stress of 25 ksi. The rupture test yielded a minimum creep rate of 0.14% hr^{-1} and a rupture strain of 65%. This contrasts with the 34% rupture strain reported in the last progress report for the specimens tested at 35 ksi and at the same temperature. In order to explain the large variation in the rupture strain at two different stress levels, fractography and an optical microscopy were carried out on the 35 ksi rupture speci-n, and the same is under way for the 25 ksi specimen. Also, preliminary TEM work has been performed on both specimens (Appendix E).

On a series of ruptured specimens, tested at 701°C and at several stress levels ranging from 15 to 40 ksi, room temperature microhardness measurements were made at various locations from the fracture surface along the longitudinal sections. At a given stress level the hardness decreased to a constant value as a function of distance from the fracture surface, and the hardness profiles for different stress levels were quite similar to one another (Appendix E).

At the present time, two long-term stress-rupture tests are in progress on AISI 330 SS. The test conditions are 20 ksi at 600°C and 60 ksi at 500°C, and the accumulated test time to date is 2754 hours and 755 hours, respectively. A minimum creep rate of 1.35×10^{-6} hr^{-1} has been obtained from the test at 20 ksi and at 600°C, and this has been used together with the creep data compiled up to the present time to modify the previously reported value of the apparent activation energy for creep, ΔH_c. Previously 100 Kcal/mole was reported for ΔH_c; however, the modified value for ΔH_c is 118 Kcal/mole in the 600°C - 800°C temperature range (Appendix E).

Hot-hardness tests were conducted on Inconel 718, Inconel 706, PE-16 and M-813. Based on the hot-hardness data, apparent activation energies for indentation hardness and for creep have been determined. The results on the activation energy for indentation hardness for $T > .55T_m$ are: 13 Kcal/mole for Inconel 718; 9 Kcal/mole for Inconel 706; 10 Kcal/mole ɔr PE-16; and 11 Kcal/mole for M-813. The activation energy for creep calculated for Inconel 718 and PE-16 were correlated with hot-tensile data of the same. In Inconel 718 the agreement between the calculated and experimental UTS values was good within 10% in the temperature range up to 650°C; however, the calculated values were much higher than the experimental values at the higher temperatures. On the other hand, the agreement in PE-16 was good being within 20% at all temperature ranges investigated (Appendix E).

Low-cycle fatigue crack initiation and propagation behavior of Incoloy 800 has been investigated by using scanning electron microscopy in both push-pull and bend specimens fatigued at temperatures of 649, 704 and 760°C, and strain ranges of 0.49 $\sim$ 2.01%. Some of the important observations are: 1) the fraction of fatigue life to initiate a 0.1 mm crack is strongly dependent on the plastic strain range in the bend specimens and only slightly dependent in the push-pull specimens, but insensitive to the temperatures in both types of specimens, 2) the crack growth rate in the bend specimens initially increases and then decreases, while that in the push-pull specimens generally increases continuously (Appendix F).

A study of the plastic zone around a fatigue crack in a 304 SS compact tension specimen has been initiated. The specimen was tested at 538°C with a stress ratio of 0.05 and a frequency of 0.067 s^{-1}. This study employs three experimental techniques: microhardness measurements, SEM and TEM. At the present time, the microhardness measurements and SEM work have been completed, and the results are presented in this report, cluding a hardness contour map around the crack tip (Appendix F).

A total of fourteen creep-rupture tests have been conducted on AISI 330 stainless steel at various temperatures and stress levels, and this completes the mechanical testing part of the study on substructure-creep rupture interrelationships. The raw creep data can be adequately described by the power law creep equation with the stress exponent, n, varying from approximately 7 to 10 for various temperatures. The substructural evaluation of the creep-ruptured specimens is under way by using transmission electron microscopy, and the preliminary results show that the subgrains and cells develop in specimens tested at lower and higher stress levels, respectively.

Due to problems of specimen oxidation and heating element cracks, the Hot Hardness Testing Machine has recently been overhauled, and the result, for one thing, is a significant improvement of the vacuum in the system: now reaching 3.0 E-04 Pa (Appendix F).

A study on substructural developments during high temperature tensile deformation of 304 SS has been initiated. The specimens were tested at 650°C and at a strain rate of 3.17 E-04 S^{-1} to various strain levels, including one to the failure. This study will be carried out by using TEM, optical microscopy and microhardness measurements on the tested specimens (Appendix F).

As a continuation of this study on subgrain/cell developments during creep deformation, another series of creep testing has been completed on 330 SS at 652°C and 172.4 MPa. The preliminary results of microhardness and SEM on these creep tested specimens are presented in the report (Appendix F).

IV PAST PROGRESS REPORTS

1. Progress Report, July 1, 1970 to December 31, 1970, COO-2107-1, February 16. 1971, University of Cincinnati, Cincinnati, OH.
2. Progress Report, January, February, March, 1971, COO-2107-2 May 12, 1971, University of Cincinnati, Cincinnati, OH.
3. Progress Report, April, May, June, 1971, COO-2107-3, August 31, 1971, University of Cincinnati, Cincinnati, OH.
4. Progress Report, July, August, September, 1971, COO-2107-4 October 25, 1971, University of Cincinnati, Cincinnati, OH.
5. Progress Report, October, November, December, 1971, COO-2107-5, February 15, 1972, University of Cincinnati, Cincinnati, OH.
6. Progress Report, January, February, March, 1972, COO-2107-6, May 15, 1972, University of Cincinnati, Cincinnati, OH.
7. Progress Report, April thru August, 1972, COO-2107-7, November 15, 1972, University of Cincinnati, Cincinnati, OH.
8. Progress Report, September thru December, 1972, C))-2107-8, March 15, 1973, University of Cincinnati, Cincinnati, OH.
9. Progress Report, January thru March, 1973, COO-2107-9, June 15, 1973, University of Cincinnati, Cincinnati, OH.
10. Progress Report, April thru December, 1973, COO-2107-10, March 15, 1974, University of Cincinnati, Cincinnati, OH.
11. Progress Report, January 1, 1974 to December 31, 1975, COO-2107-11, March 15, 1976, University of Cincinnati, Cincinnati, OH.

V PUBLICATIONS IN TECHNICAL JOURNALS

1. Fatique Crack Behavior of Incoloy 800 Tested in the Bend and Push-Pull Mode, Accepted for Publicatikn in Materials Science and Engineering (1977)
2. Substructure Development During Low Cycle Fatigue of AISI 304 Stainless Steel at 649°C, Acta Metallurgica, 25, 107 (1977)
3. The Dislocation Substructure, Carbides, and the Deformation Map for AISI 304 Stainless Stell, Met. Trans., 7A, 879 (1976)
4. Second Phase Formation and its Influence on the Fatigue Properties of Incoloy 800 at Elevated Temperature, Met. Trans., 7A, 1473 (1976)
5. Correlation of the Microstructure with the Creep and Tensile Properties of AISI 304 Stainless Steel, Proceedings of the ASME Symposium on Structural Materials for Service at Elevated Temperatures in Nuclear Power Generation, MPC-1, 31, (1975)
6. Some Aspects of Sub-Boundary and Mobile Dislocations During High Temperature Creep of AISI 304 Stainless Steel, Met. Trans. 5, 315 (1974)
7. The Role of Twin Boundary/ Grain Boundary Intersections on Microcracking Behavior of AISI 304 Stainless Steel Deformed in Slow Tension and Creep at 650°C, J. Mat. Sci. 10, 1084 (1975)
8. Correlation of the Hot-Hardness with the Tensile Strength of 304 Stainless Steel to Temperatures of 1250°C, Met. Trans. 6A, 1101 (1975)
9. A Correlation Between the Hot-Hardness and the Hot-Tensile Properties of AISI 304 Stainless Steel, Met. Trans. 5, 315 (1974)
10. Substructure of Type 316 Stainless Steel Deformed in Slow Tension at Temperatures Between 21° and 816°C, Acta Met. 21, 1269 (1973)
11. Reply to "Comments on 'On the Influence of Deformation Rate on Intragranular Crack Propagation in Type 304 Stainless Steel'", J. Mat. Sci. 8, 1828 (1973).
12. Deformation Induced Twin-Boundary Crack Formation in Type 304 Stainless Steel, Mat. Sci. and Engrg. 11, 97 (1973)
13. On the Influence of Deformation Rate on Intragranular Crack Propagation in Type 304 Stainless Steel, J. Mat. Sci. 8, 104 (1973)

Con't Publications

14. Correlation of Substructure with the Elevated Temperature Low Cycle Fatigue Properties of AISI 304 and 316 Stainless Steel, Published in the Proceedings of the Symposium on Fatigue at Elevated Temperatures - ASTM STP-520 (1973).

15. Quantitative Characterization of the Substructute of AISI 316 Stainless Steel Resulting From Creep, Met Trans. 4, 749 (1973)

16. Characterization of the Deformation Substructure of AISI 316 Stainless Steel after High Strain Fatigue at Elevated Temperatures, Met. Trans. 3, 1677 (1972)

17. Correlation Between Strain Hardening Parameters and Dislocation Substructure in Austenitic Stainless Steels, Scripta METALLURGICA 6, 155 (1972)

APPENDIX A

PROGRESS REPORT FOR PERIOD ENDING JANUARY 31, 1976

7.1.1 Introduction

The objective of this program is to (a) evaluate the time, temperature and stress-dependent mechanical properties of reactor structural materials, (b) determine the relationship of these properties to the microstructure and (c) show the contribution of the microstructure to the internal stress fields and the subsequent influence on microcracking and the grain boundary sliding behavior during the normal plastic deformation at elevated temperatures. Special consideration is being given to operating conditions typical of nuclear reactor applications, including the knowledge that the radiation environment can influence the substructure of these metals, a circumstance which can lead to significant changes in the conventional mechanical property behavior.

7.1.2 Experimental Program

Transmission electron microscopy has been used to study the deformation substructure resulting from creep, fatigue and tensile deformation at elevated temperatures. New work being initiated will also include similar studies on the Commercial, the Developmental and the Fundamental alloys being evaluated in the National Alloy Developmental Program with particular attention on the application of hot-hardness measurement as a strength microprobe.

A study on difference in fatigue-cracking behavior between bend and push-pull mode of testing is also underway by scanning electron microscopy and the results will be provided in the future reports.

As reported in the previous progress reports(1-4), the substructure formed during strain-controlled push-pull fatigue test of Incoloy 800 has been characterized as part of ongoing research programs at the University of Cincinnati. Observations and the general relationships of subboundary intercept size, dislocation density with fatigue properties are presented. Further analysis and discussions of substructure data will be given in the next report.

7.1.2.1 High Temperature Fatigue Substructure for Incoloy 800

Dislocation distribution of undeformed Incoloy 800 was found to be non-uniform, probably as a result of different dislocation generation during heat treatment. Dislocation density was around 2.3×10^9 cm^{-2}. Extended nodes of partial dislocations were not observed, indicating the stacking fault energy (SFE) of Incoloy 800 is higher than that of AISI 304 or 316 stainless steels where nodes were sometimes observed. Using Gallagher's method(5), the SFE for Incoloy 800 is estimated to be ∿ 90 ergs/cm^2. Since SFE is very sensitive to alloying(5), this estimation is only approximate.

The dislocation structure for Incoloy 800 tested at 538°C is shown in Figs. 1 and 2, and the substructure data are summarized in Table I. Cellular structures were observed in only two out of seven specimens examined which were tested under the large strain range at 538°C. This indicates that the higher dislocation density is needed to form cells at lower temperature. Due to extremely high density, the average mobile dislocation density was not able to be measured in some of the specimens as shown in Table I. The density here was defined previously(4).

Extended cell walls shown in Fig. 1-a were found to be lying parallel to {100} planes from the tilting experiment with the stereographic projection. Well defined cells were formed in specimen #2X72 (See Fig. 1-b). Except for specimens #2R42 and #2X72, all specimens at 538°C exhibited the planar dislocation band structure (See Figs. 1-c, 1-d, and Fig. 2). These bands were often found to be aligned parallel to the low index planes such as {100}, {110}, and {111}. Figs. 1-d and 2 show that band structures mostly consist of dipoles, loops and tangles.

In addition to the second phases such as $M_{23}C_6$ and TiN which were observed in most Incoloy 800 specimens at all testing temperatures, γ' precipitates were also observed in specimens with long testing times at 538°C. The details of the TEM identification procedure of second phases formed in Incoloy 800 during fatigue were given before(3). The influence of precipitates on the fatigue properties is also discussed there. The second phases formed in Incoloy 800 do not appear to affect the cell or subgrain formation behavior.

The characteristics of the dislocation substructure for Incoloy 800 specimens tested at 649°C are shown in Fig. 3 and Fig. 4, and the substructure data are summarized in Table II. The tendency for subboundary formation at 649°C is more pronounced than that at 538°C, as shown in Fig. 3. Five out of eight specimens studied at 649°C display the cell formation. Cells were found to form in the specimens tested under large strain ranges, which is consistent with the results from the specimens tested at 538°C. Well defined cells, close to subgrains were found in specimen #2N14 which had a longer test time than the others (see Fig. 3-c). The specimens without cell formation often reveal the banded dislocation structures as shown in Fig. 3-d, 3-f and 3-g.

Fig. 4 shows the general features of the free dislocations in the specimens tested at 649°C in which dislocation interactions with second phases are much in evidence. $M_{23}C_6$ particles are often found to form preferentially along the grain boundary, while small TiN particles with high number density are uniformly distributed throughout the matrix.

A summary of the fatigue substructure data for the Incoloy 800 push-pull specimens tested at 704°C is presented in Table III and the characteristics of dislocation substructure are given in Fig. 5. Well defined subgrains were formed in specimens tested at 704°C. The propensity for subboundary formation at 704°C is greater than that at 649°C. Five out of seven specimens examined were found to have subgrains. This suggests the subboundary formation is strongly temperature dependent. $M_{23}C_6$ particles become larger and incoherent at 704°C as shown in Fig. 5-d.

The fatigue substructure data for Incoloy 800 specimens tested at 760°C is summarized in Table IV and the substructural characteristics are shown in Figs. 6 and 7. The inclination to form subgrains becomes extreme at this temperature. As a matter of fact, all ten specimens examined by TEM showed subgrain formation. In specimen #2B26, which was cycled under a total strain range of 2% at 760°C, the dislocation density was not obtained because the entire volume was occupied by subgrains. Fig. 6 shows that the subgrain intercept increases with decreasing stress range,which is consistent with the results from those specimens tested at 538°C, 649°C and 704°C. $M_{23}C_6$ particles become larger and incoherent and the number density of small TiN particle is decreased in specimens tested for a longer period of time at 760°C.

Similar to case of dislocation bands observed at low testing temperatures, the subboundaries formed at 760°C were often found to lie on the low index crystallographic planes such as {100}, {110} and {111}. In order to study the nature of dislocations comprising the subboundaries, the Burgers vector for the individual dislocations within the subgrain boundaries were determined by using $\overline{g} \cdot \overline{b} = 0$ criterion. A subgrain boundary with crossing dislocations shown in Fig. 6-g was found to be a tilt boundary lying on the $(1\overline{1}1)$ plane. A row of parallel edge dislocations which are out of contrast in Fig. 6-g, have a Burgers vector of $\overline{b}_1 = a/2\ [10\overline{1}]$ and lie on the $(1\overline{1}1)$ plane, while another set of edge dislocations in contrast have a Burgers vector of $\overline{b}_2 = a/2\ [\overline{1}0\overline{1}]$ which is perpendicular to the $(1\overline{1}1)$ plane. Thus Burgers vectors of two sets of crossing dislocations are not coplanar.

Fig. 8 gives an insight into the possible role of subboundaries on the high temperature fatigue deformation. Pile-ups of dislocations against subgrain boundaries and grain boundaries are clearly seen in this composite micrograph. The position of the pile-ups suggest that the subboundaries, once formed, might act as barriers to the moving dislocations. It should be mentioned, however, that the pile-ups were rarely observed in this study. Blocky $M_{23}C_6$ precipitates are formed along the grain boundary because of a long fatigue at high temperature (specimen #2H32, t_f = 11.86 hours).

The subboundary intercept, λ, as a function of the shear modulus compensated stress, $\Delta\sigma/2G$ for Incoloy 800 fatigue tested in push-pull mode is plotted in Fig. 9. Several interesting observaaions can be made from this figure. The general inverse relationship between the subgrain size and stress, which has been observed by many investigators under different modes of plastic deformation, is found to be true for the results of the present investigation. It is also apparent from Fig. 9 that the subboundary intercept, λ, is strongly dependent on the plastic strain range, $\Delta\varepsilon_p$. The following relationships were obtained for subgrain size as a function of shear modulus compensated saturation stress,

$$\lambda = 1.1 \times 10^{-2} b \left(\frac{\Delta\sigma}{2G} \right)^{-2.43\pm0.15} \qquad [7.1]$$

for $\Delta\varepsilon_p > 0.5\%$

$$\lambda = 5.8 \times 10^{-2} b \left(\frac{\Delta\sigma}{2G} \right)^{-2.02\pm0.37} \qquad [7.2]$$

for $\Delta\varepsilon_p < 0.3\%$

where b is the Burgers vector (2.54×10^{-8} cm) and the $\Delta\varepsilon_p$ is the plastic range. The subboundary intercept, λ, appears to reach the saturation value as the plastic strain range increases at the constant shear modulus compensated saturation stress, $\Delta\sigma/2G$.

A plot of the dislocation density, ρ, versus the shear modulus compensated saturation stress, $\Delta\sigma/2G$, for Incoloy 800 fatigue tested in push-pull mode is presented in Fig. 10. An equation of the type

$$\rho = A\ (\Delta\sigma/2G)^2 \qquad [7.3]$$

where A is a constant, which was found to satisfactorily describe the relationship between the dislocation density and the flow stress. But the dislocation density is also found to be a function of the plastic strain range with the following equations (See Fig. 11):

$$\tau_s = 1.74 + 0.75\ Gb\sqrt{\rho} \qquad [7.4]$$

$$\text{for } \Delta\varepsilon_p > 0.5\%$$

$$\tau_s = 2.67 + 0.33\ Gb\sqrt{\rho} \qquad [7.5]$$

$$\text{for } \Delta\varepsilon_p < 0.3\%$$

where τ_s is the saturation shear stress in kg/mm^2 as defined elsewhere(6). This is consistent with the subboundary intercept findings (See Fig. 10). A further analysis and discussion of the data for Incoloy 800 will appear in the next report.

7.1.3 <u>References</u>

1. ORNL - 4948, "Mechanical Properties Test Data for Structural Materials", Quarterly Progress Report for Period Ending January 31, 1974, pp. 359-364.
2. ORNL - 4963, "Mechanical Properties Test Data for Structural Materials", Quarterly Progress Report for Period Ending April 30, 1974, pp. 228-241.
3. ORNL - 5105, "Mechanical Properties Test Data for Structural Materials", Quarterly Progress Report for

Period Ending April 30, 1975, pp. 324-338.

4. ORNL - 5107, "Mechanical Properties Test Data for Structural Materials", Quarterly Progress Report for Period Ending October 31, 1975, pp. 275-287.

5. P. C. J. Gallagher, Met. Trans., 1, (1970) pp. 2429.

6. H. Nahm, Ph.D. Dissertation, 1975, University of Cincinnati.

TABLE-I

FATIGUE AND SUBSTRUCTURE PROPERTIES OF INCOLOY 800 AT 538°C

Spec. No.	Strain Rate $\dot{\varepsilon}$, sec^{-1}	Plastic Strain Range $\Delta\varepsilon_p$, Pct.	Modulus Compensated[(a)] Saturation Stress $\Delta\sigma/2G$	$\Delta\sigma/2E$	Average Subboundary Intercept λ, μm	Average Mobile Dislocation Density ρ_m, cm^2	Sub-boundary Misorientation θ, Degrees
2R42	4×10^{-3}	2.35	8.53×10^{-3}	3.12×10^{-3}	0.29 ± 0.04	N.M.	N.M.
2X72	4×10^{-3}	1.43	7.58×10^{-3}	2.77×10^{-3}	0.37 ± 0.02	N.M.	N.M.
2D52	4×10^{-3}	0.60	5.35×10^{-3}	1.96×10^{-3}	N.O.	N.M.	----
2T44	4×10^{-3}	0.17	4.42×10^{-3}	1.62×10^{-3}	N.O.	$(1.52 \pm 0.63) \times 10^{10}$	----
2Q41	4×10^{-3}	0.01	3.31×10^{-3}	1.21×10^{-3}	N.O.	$(9.13 \pm 0.84) \times 10^{9}$	----
2H8	4×10^{-4}	0.55	6.05×10^{-3}	2.21×10^{-3}	N.O.	N.M.	----
2I9	4×10^{-4}	0.12	5.16×10^{-3}	1.89×10^{-3}	N.O.	$(1.40 \pm 0.19) \times 10^{10}$	----

[(a)] Elastic Modulus at 538°C ($E=23.58 \times 10^6$, $G=8.60 \times 10^6$ psi) is obtained from the International Nickel Company (Technical Bulletin T-40).

TABLE II

FATIGUE AND SUBSTRUCTURE PROPERTIES OF INCOLOY 800 AT 649°C

	Strain Rate	Plastic Strain Range	Modulus Compensated(a) Saturation Stress		Average Subboundary Intercept	Average Mobile Dislocation Density	Sub-boundary Misorientation
Spec. No.	ε sec^{-1}	$\Delta\varepsilon_p$, Pct.	$\Delta\sigma/2G$	$\Delta\sigma/2E$	λ, μm	ρ_m, cm^2	θ, Degrees
2E53	4×10^{-3}	3.36	8.21×10^{-3}	2.98×10^{-3}	0.40 ± 0.03	N.M.	N.M.
2A73	4×10^{-3}	1.47	6.98×10^{-3}	2.53×10^{-3}	0.48 ± 0.03	$(8.15 \pm 0.90)x10^9$	0.66 ± 0.15
2Q40	4×10^{-3}	0.56	5.90×10^{-3}	2.14×10^{-3}	0.83 ± 0.05	$(8.30 \pm 1.20)x10^9$	0.17 ± 0.02
2G55	4×10^{-3}	0.19	4.21×10^{-3}	1.52×10^{-3}	0.78 ± 0.15	N.M.	N.M.
2F54	4×10^{-3}	0.02	3.12×10^{-3}	1.13×10^{-3}	N.O.	$(4.49 \pm 0.83)x10^9$	----
2N14	4×10^{-4}	0.58	5.56×10^{-3}	2.02×10^{-3}	0.82 ± 0.07	$(4.54 \pm 0.63)x10^9$	0.40 ± 0.07
2M13	4×10^{-4}	0.16	4.61×10^{-3}	1.67×10^{-3}	N.O.	$(1.05 \pm 0.10)x10^{10}$	----
2N62	4×10^{-4}	0.02	3.12×10^{-3}	1.13×10^{-3}	N.O.	$(8.20 \pm 0.60)x10^9$	----

(a) Elastic Modulus at 649°C ($E = 22.37 \times 10^6$, $G = 8.12 \times 10^6$ psi) is obtained from the International Nickel Company (Technical Bulletin T-40).

TABLE II-I

FATIGUE AND SUBSTRUCTURE PROPERTIES OF INCOLOY 800 AT 704°C

Spec. No.	Strain Rate ε, sec^{-1}	Plastic Strain Range $\Delta\varepsilon_p$, Pct.	Modulus Compensated(a) Saturation Stress		Average Subboundary Intercept λ, μm	Average Mobile Dislocation Density ρ_m, cm^2	Sub-boundary Misorientation θ, Degrees
			$\Delta\sigma/2G$	$\Delta\sigma/2E$			
2V70	4×10^{-3}	3.43	7.19×10^{-3}	2.60×10^{-3}	0.48 ± 0.05	$(9.10 \pm 3.93)\times10^{9}$	N.M.
2U21	4×10^{-3}	1.53	6.18×10^{-3}	2.24×10^{-3}	0.66 ± 0.03	$(5.50 \pm 1.90)\times10^{9}$	0.44 ± 0.12
2T20	4×10^{-3}	0.60	5.32×10^{-3}	1.93×10^{-3}	1.09 ± 0.16	$(7.41 \pm 1.73)\times10^{9}$	0.48 ± 0.17
2I57	4×10^{-3}	0.20	4.06×10^{-3}	1.47×10^{-3}	0.88 ± 0.11	$(6.66 \pm 0.77)\times10^{9}$	0.53 ± 0.19
2T68	4×10^{-3}	0.06	3.20×10^{-3}	1.16×10^{-3}	N.O.	$(4.70 \pm 0.58)\times10^{9}$	----
2P16	4×10^{-4}	0.65	4.69×10^{-3}	1.70×10^{-3}	1.44 ± 0.32	$(4.59 \pm 0.50)\times10^{9}$	0.75 ± 0.29
2B74	4×10^{-4}	0.04	2.83×10^{-3}	1.02×10^{-3}	N.O.	$(2.39 \pm 0.21)\times10^{9}$	----

(a) Elastic Modulus at 704°C ($E = 21.74 \times 10^6$, $G = 7.87 \times 10^6$ psi) is obtained from the International Nickel Company (Technical Bulletin T-40).

TABLE IV

FATIGUE AND SUBSTRUCTURE PROPERTIES OF INCOLOY 800 AT 760°C

Spec. No.	Strain Rate $\dot{\varepsilon}$, sec^{-1}	Plastic Strain Range $\Delta\varepsilon_p$, Pct.	Modulus Compensated[(a)] Saturation Stress		Average Subboundary Intercept λ, μm	Average Mobile Dislocation Density ρ_m, cm^{-2}	Subboundary Misorientation θ, Degrees
			$\Delta\sigma/2G$	$\Delta\sigma/2E$			
2C75	4×10^{-3}	3.53	5.69×10^{-3}	2.05×10^{-3}	0.97 ± 0.19	$(5.23 \pm 2.17)\times10^9$	0.67 ± 0.18
2B26	4×10^{-3}	1.61	5.08×10^{-3}	1.83×10^{-3}	1.26 ± 0.18	N.M.	0.54 ± 0.12
2F6	4×10^{-3}	0.66	4.48×10^{-3}	1.61×10^{-3}	1.05 ± 0.05	$(4.98 \pm 0.95)\times10^9$	0.76 ± 0.19
2W23	4×10^{-3}	0.24	3.49×10^{-3}	1.53×10^{-3}	1.89 ± 0.41	$(3.32 \pm 0.80)\times10^9$	0.76 ± 0.32
2D28	4×10^{-3}	0.08	3.07×10^{-3}	1.11×10^{-3}	1.90 ± 0.40	$(3.30 \pm 0.40)\times10^9$	0.42 ± 0.08
2G79	4×10^{-3}	0.07	2.48×10^{-3}	8.93×10^{-4}	2.33 ± 0.19	$(2.46 \pm 0.51)\times10^9$	0.69 ± 0.18
2K35	4×10^{-4}	1.66	4.28×10^{-3}	1.54×10^{-3}	1.61 ± 0.10	$(5.39 \pm 0.31)\times10^9$	0.85 ± 0.20
2H32	4×10^{-4}	0.72	3.76×10^{-3}	1.35×10^{-3}	2.55 ± 0.24	$(1.93 \pm 0.23)\times10^9$	0.59 ± 0.22
2I33	4×10^{-4}	0.28	2.94×10^{-3}	1.06×10^{-3}	1.60 ± 0.16	$(3.25 \pm 0.30)\times10^9$	0.90 ± 0.31
2H80	4×10^{-4}	0.08	2.35×10^{-3}	8.46×10^{-4}	2.98 ± 0.56	$(1.11 \pm 0.25)\times10^9$	0.67 ± 0.14

(a) Elastic Modulus at 760°C ($E = 21.06 \times 10^6$, $G = 7.58 \times 10^6$ psi) is obtained from the International Nickel Company (Technical Bulletin T-40).

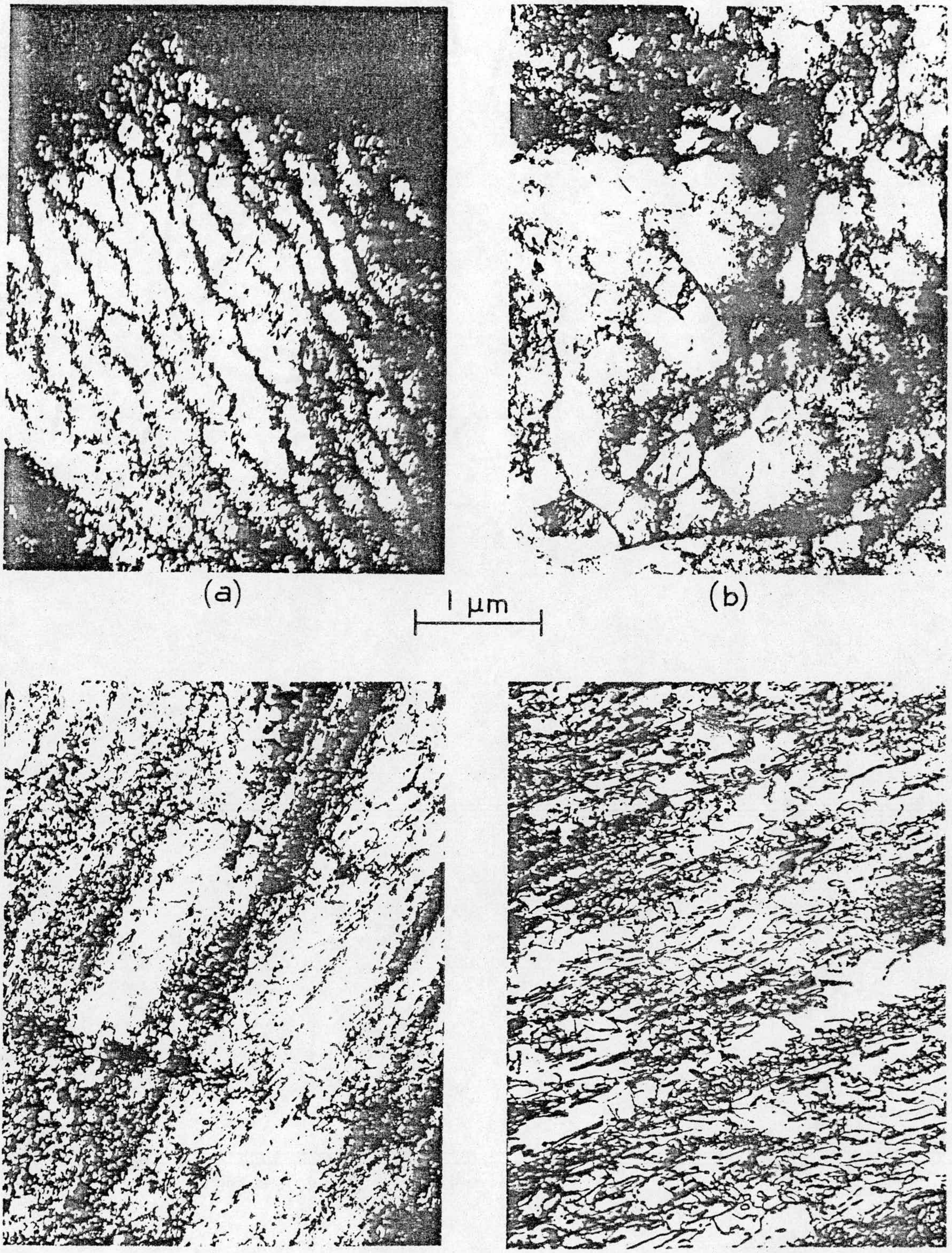

Fig. 1 Fatigue Substructure of Incoloy 800 at 538°C;
(a) Specimen 2R42; (b) Specimen 2X72;
(c) Specimen 2D52; (d) Specimen 2Q41.

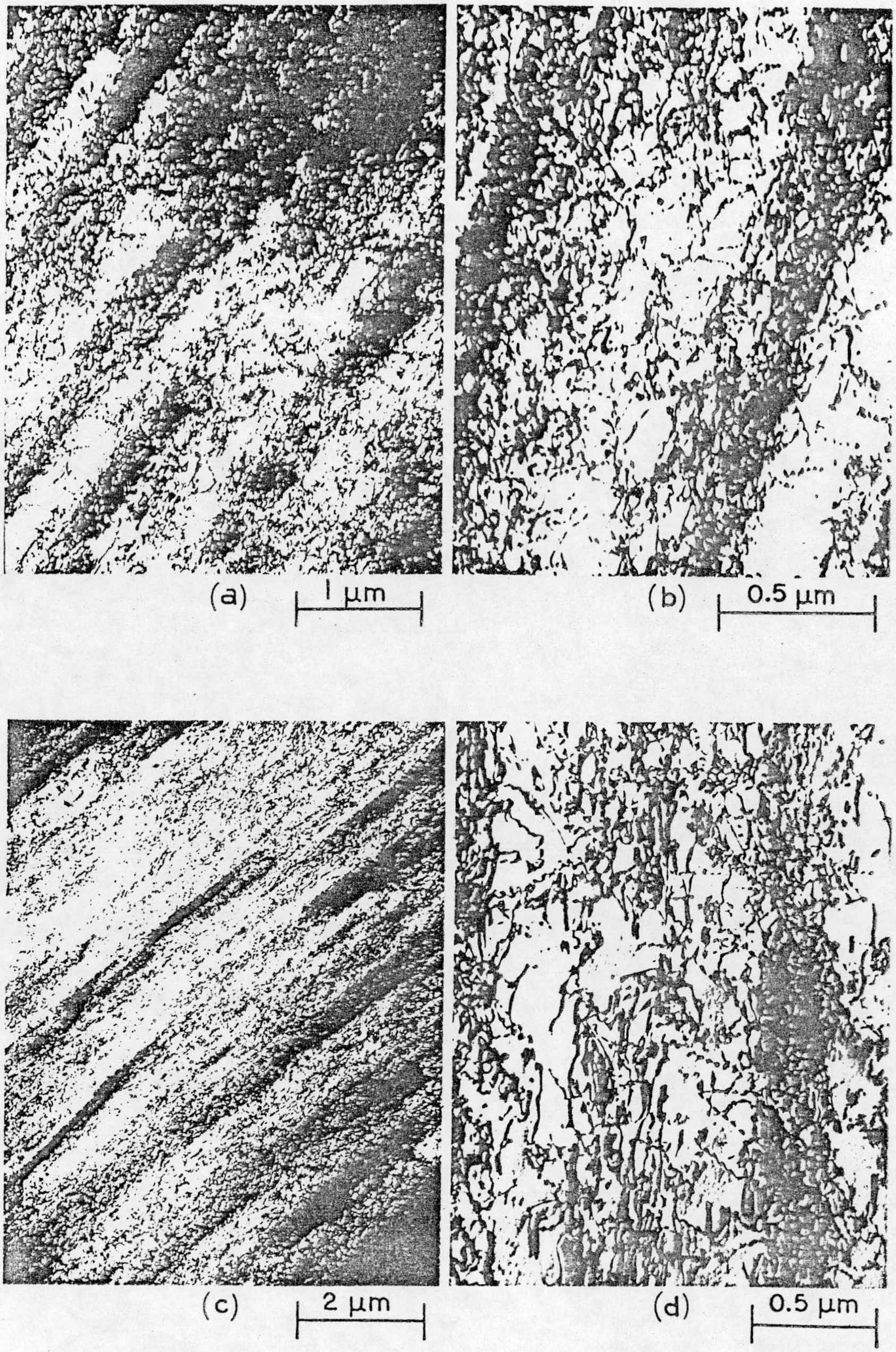

Fig. 2 Fatigue Substructure of Incoloy 800 at 538°C;
(a) Specimen 2H8; (b) Specimen 2H8;
(c) Specimen 2I9; (d) Specimen 2I9.

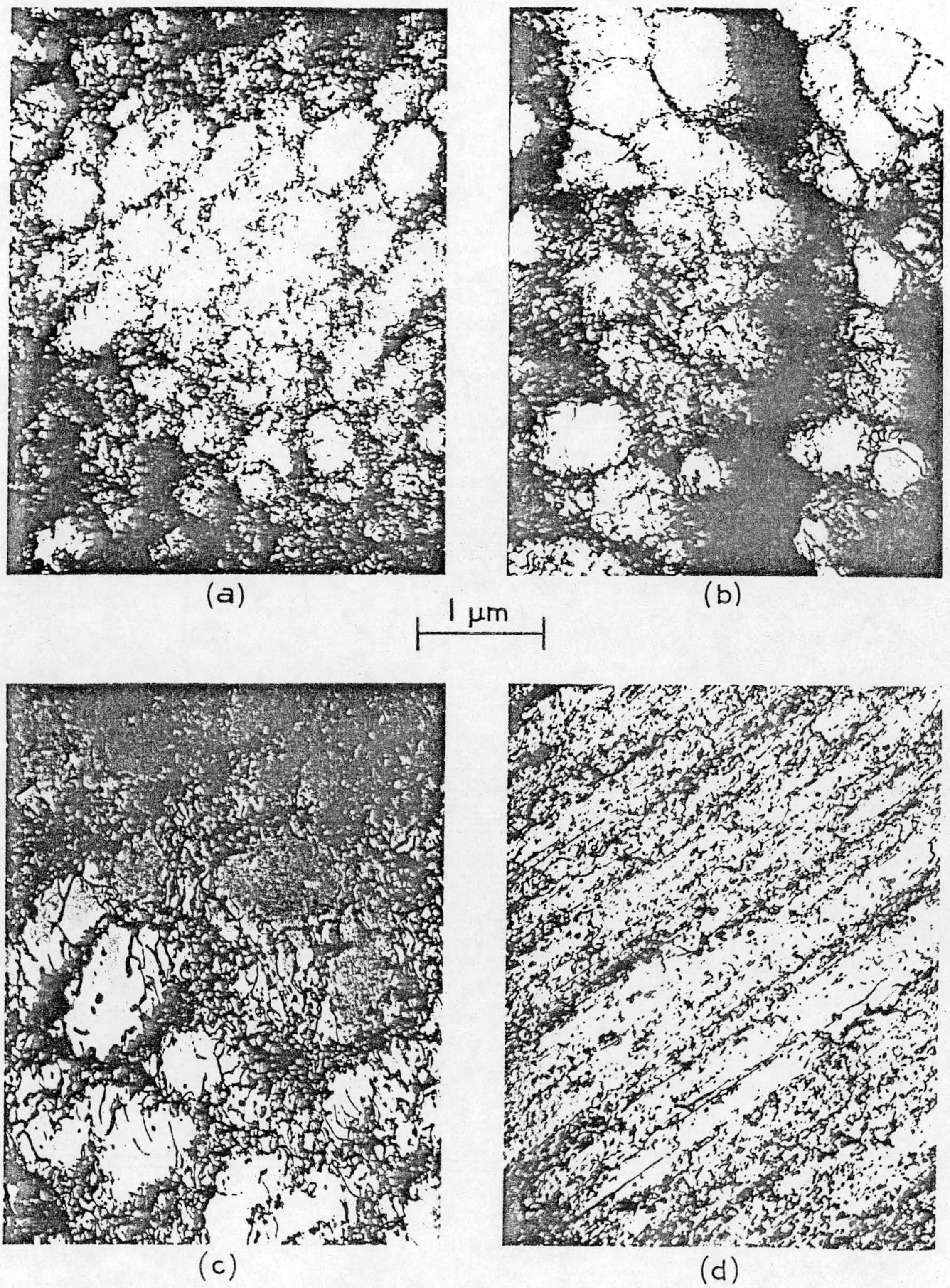

Fig. 3 Fatigue Substructure of Incoloy 800 at 649°C;
(a) Specimen 2E53; (b) Specimen 2A73;
(c) Specimen 2Q40; (d) Specimen 2F54;
(e) Specimen 2N14; (f) Specimen 2M13;
(g) Specimen 2N62.

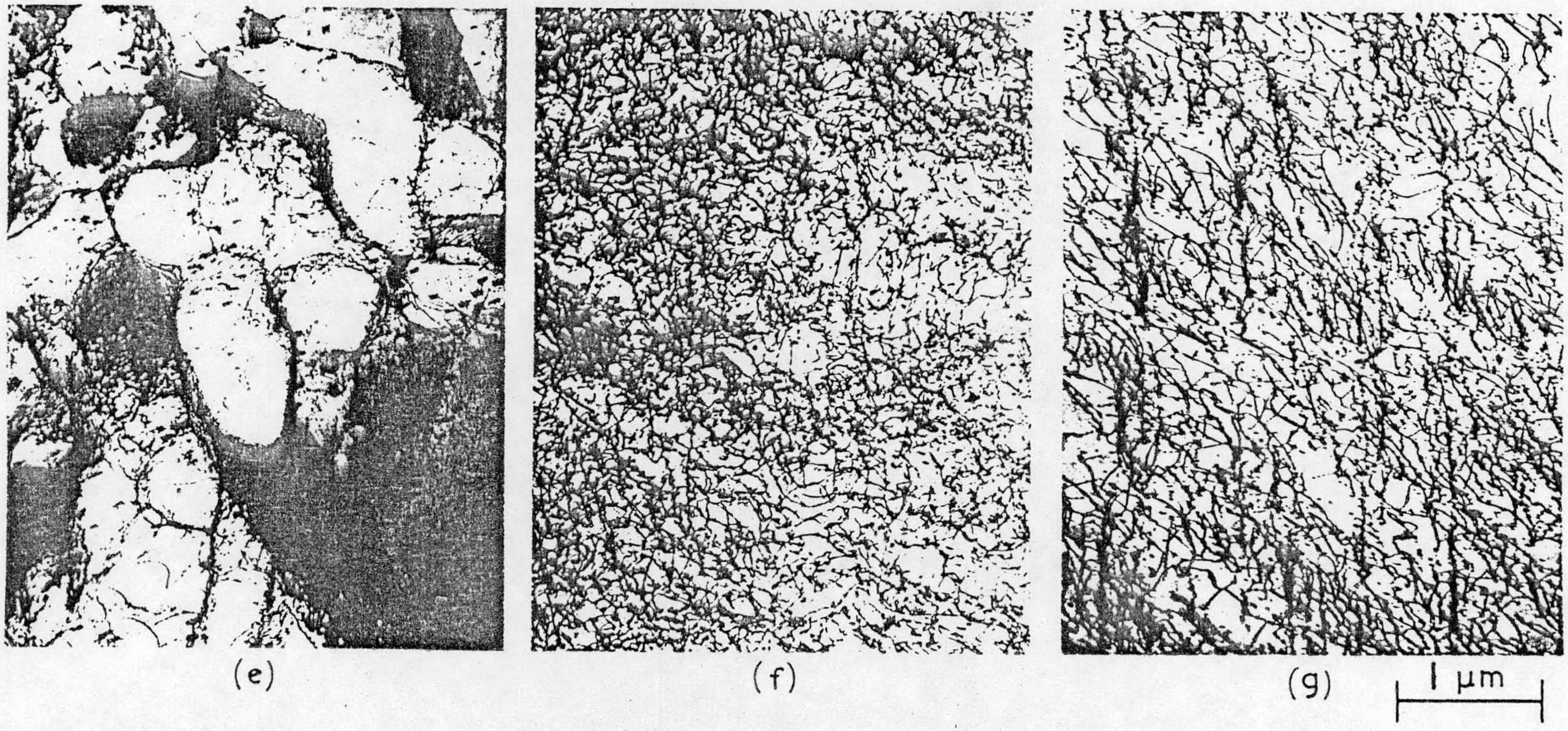

Fig. 3 Cont'd

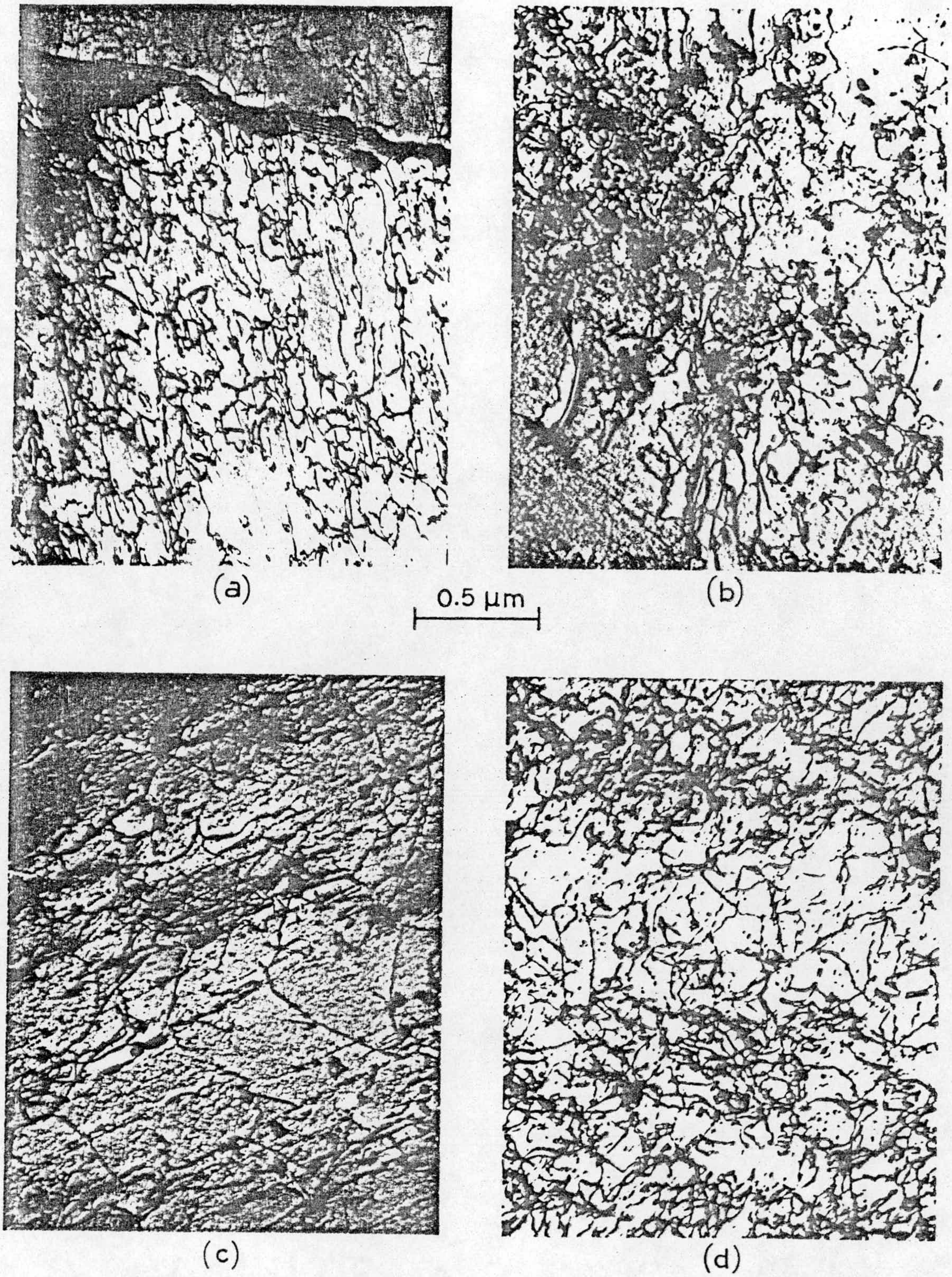

Fig. 4 Fatigue Substructure of Incoloy 800 at 649°C;
(a) Specimen 2Q40; (b) Specimen 2F54;
(c) Specimen 2N14; (d) Specimen 2M13.

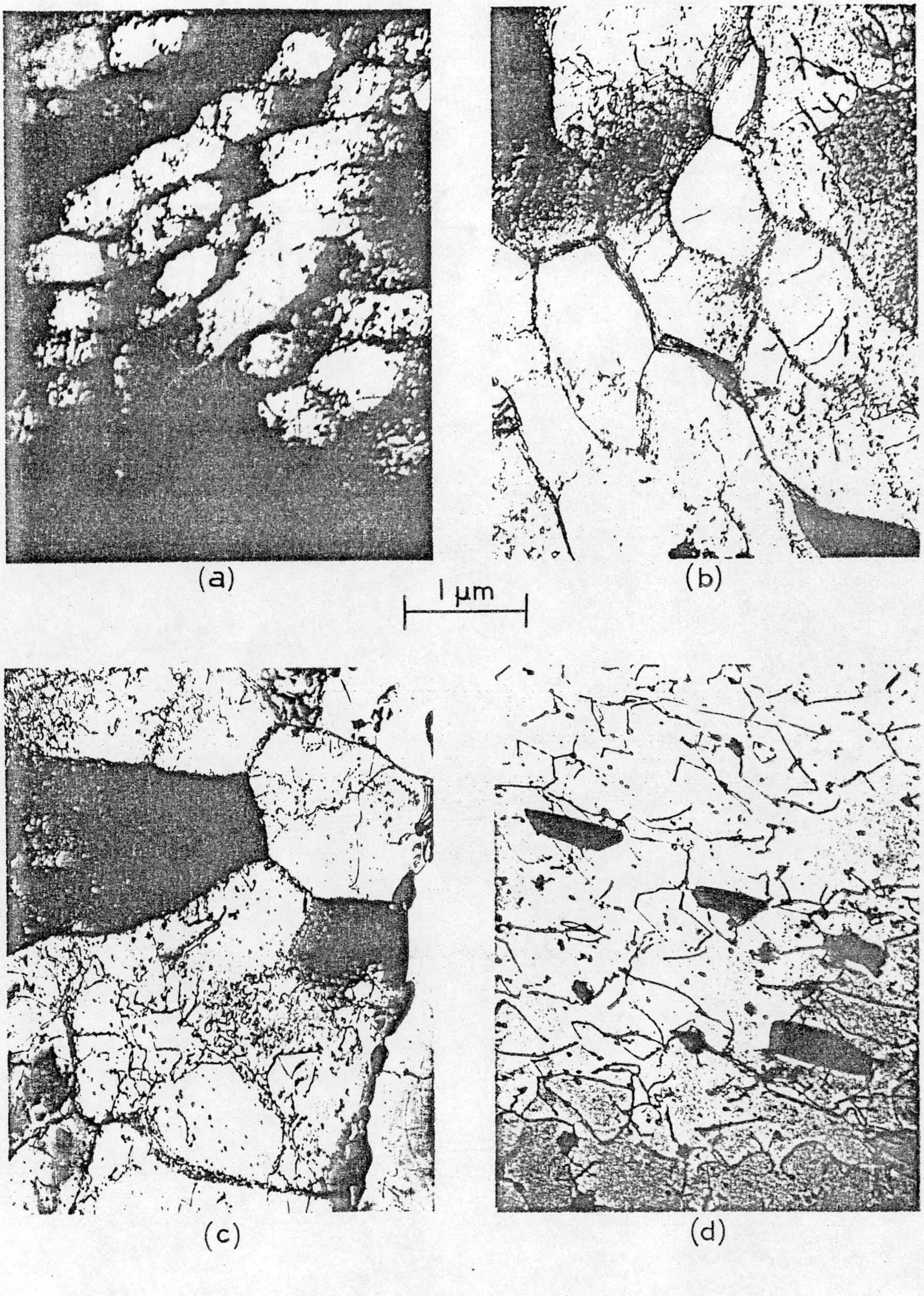

Fig. 5 Fatigue Substructure of Incoloy 800 at 704°C; (a) Specimen 2V70; (b) Specimen 2U21; (c) Specimen 2I57; (d) Specimen 2B74.

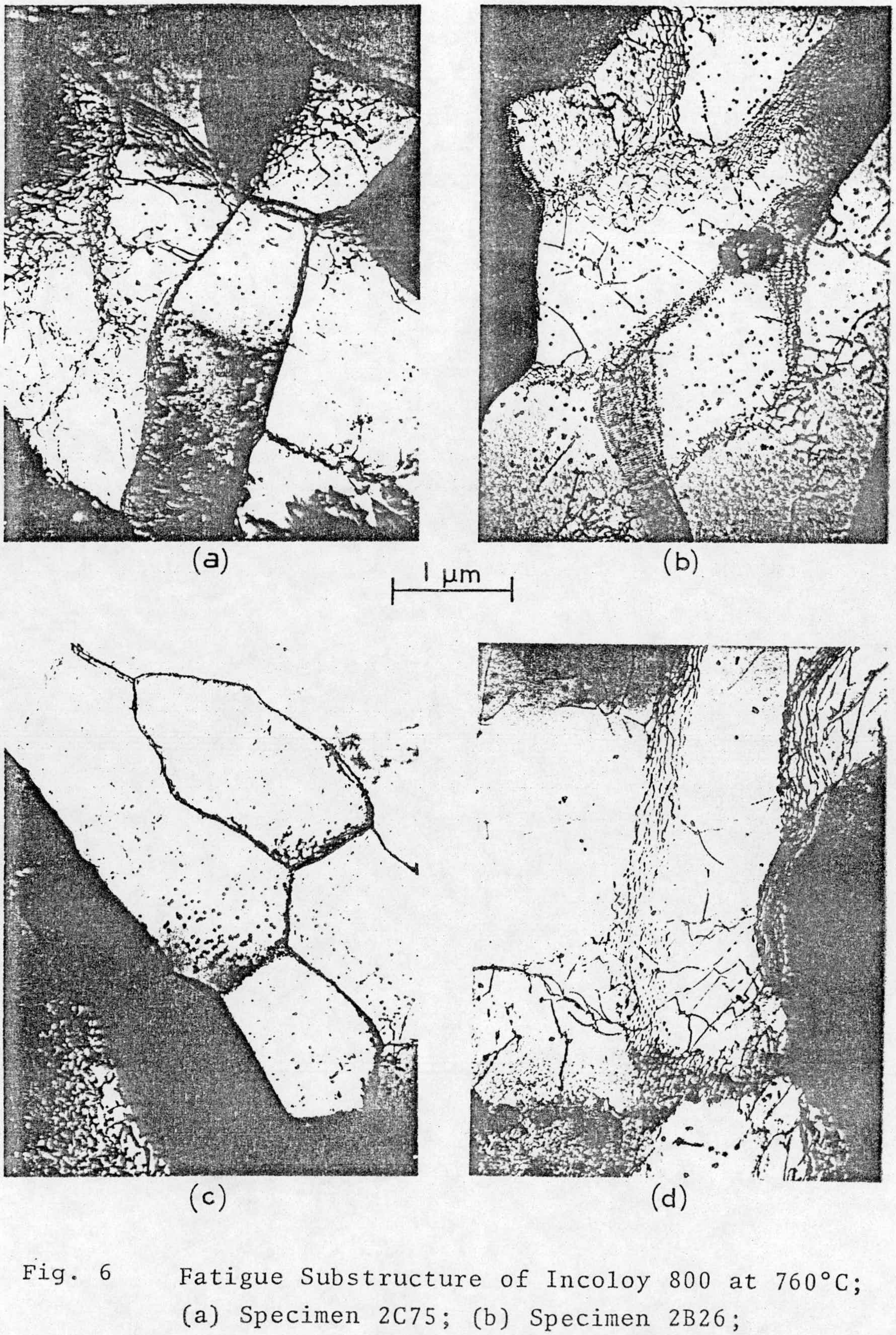

Fig. 6 Fatigue Substructure of Incoloy 800 at 760°C;
(a) Specimen 2C75; (b) Specimen 2B26;
(c) Specimen 2F6; (d) Specimen 2D28;
(e) Specimen 2K35; (f) Specimen 2H32;
(g) Specimen 2H80.

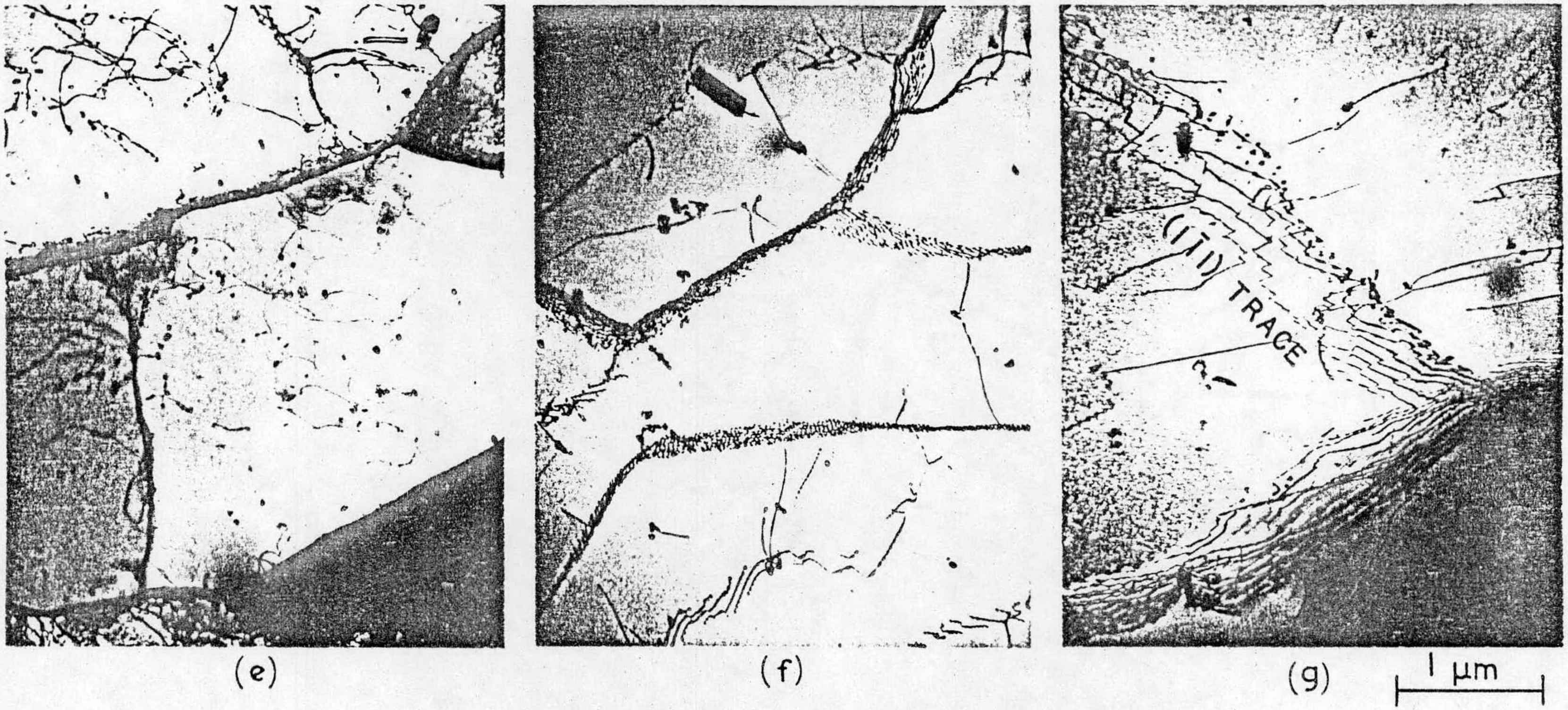

(e) (f) (g)

Fig. 6 Cont'd

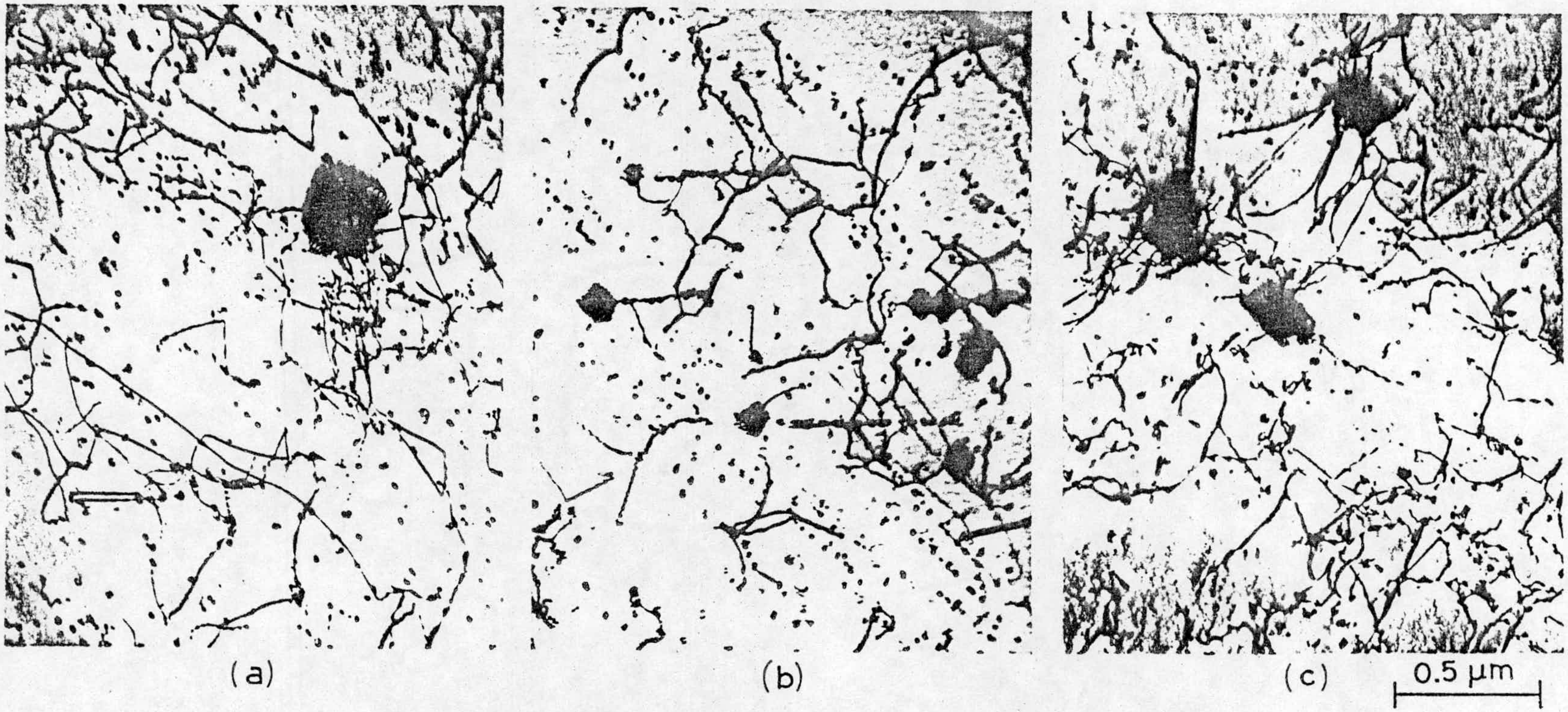

Fig. 7 Fatigue Substructure of Incoloy 800 at 760°C; (a) Specimen 2F6; (b) Specimen 2D28; (c) Specimen 2K35.

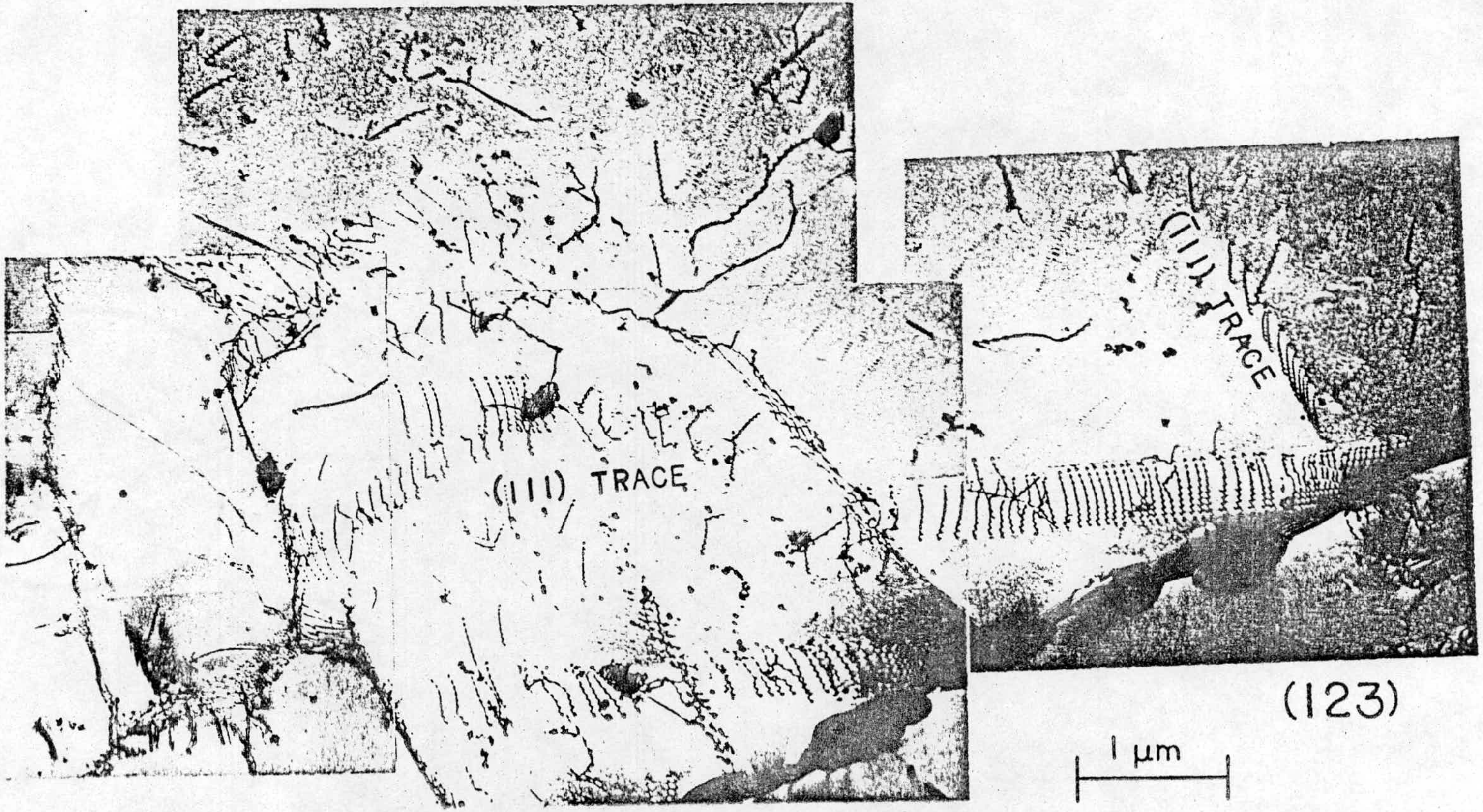

Fig. 8 Fatigue Substructure of Incoloy 800 in Specimen 2H32 at 760°C.

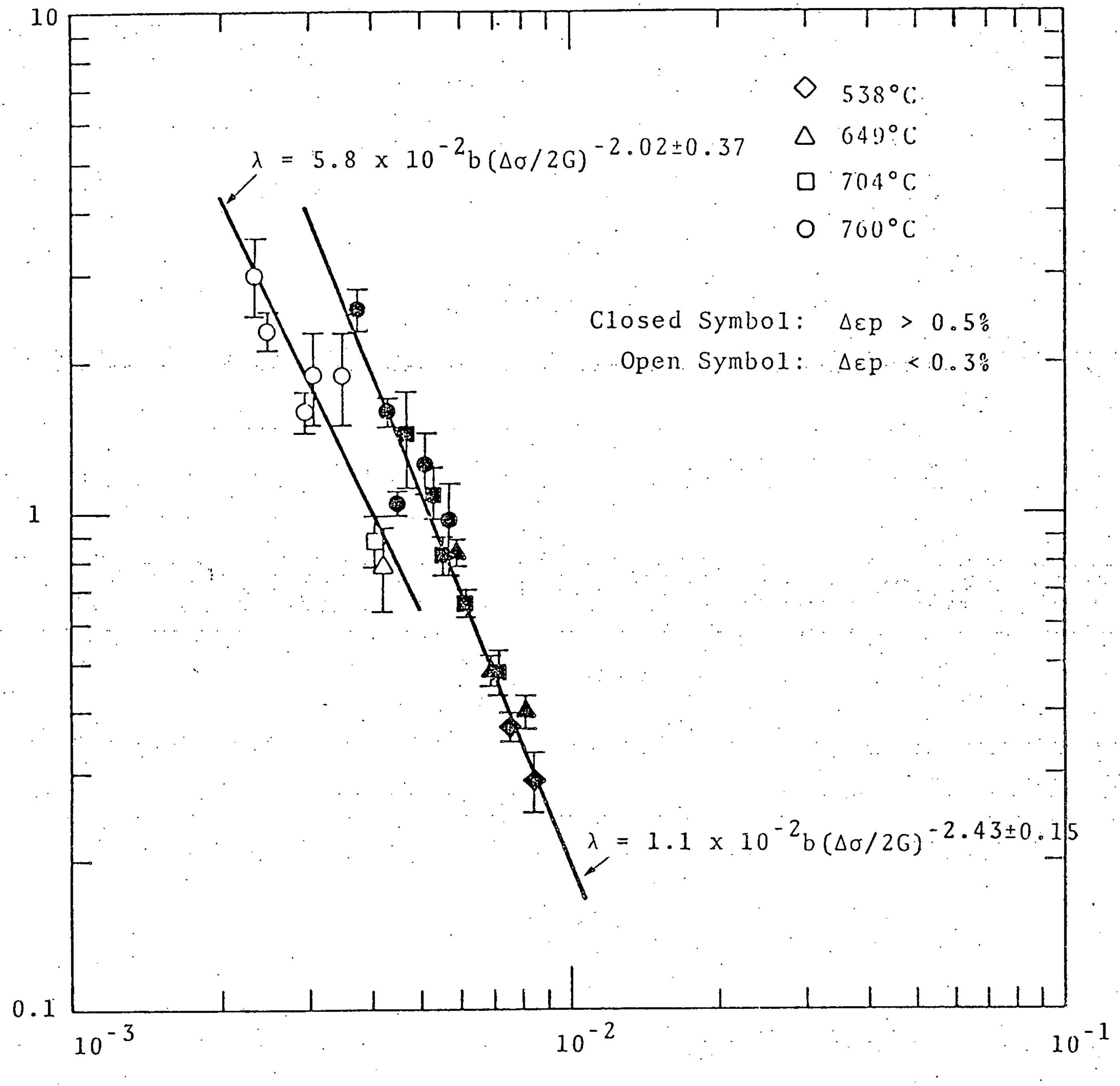

Fig. 9 The Subboundary Intercept Size, λ, as a Function of the Shear Modulus Compensated Saturation Stress $\Delta\sigma/2G$ for Incoloy 800.

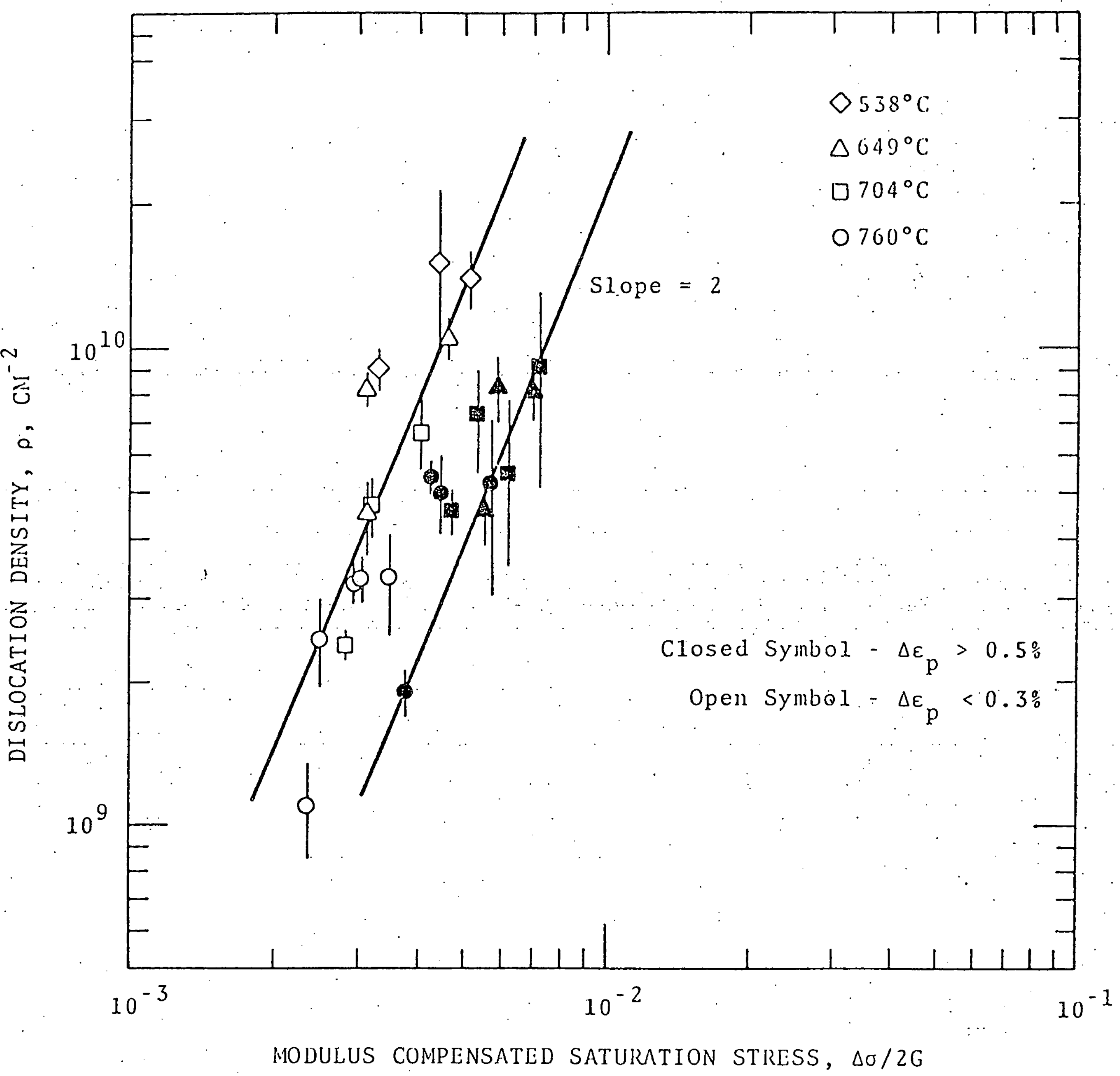

Fig. 10 The Dislocation Density, ρ, as a Function of the Shear Modulus Compensated Saturation Stress, Δσ/2G, for Incoloy 800.

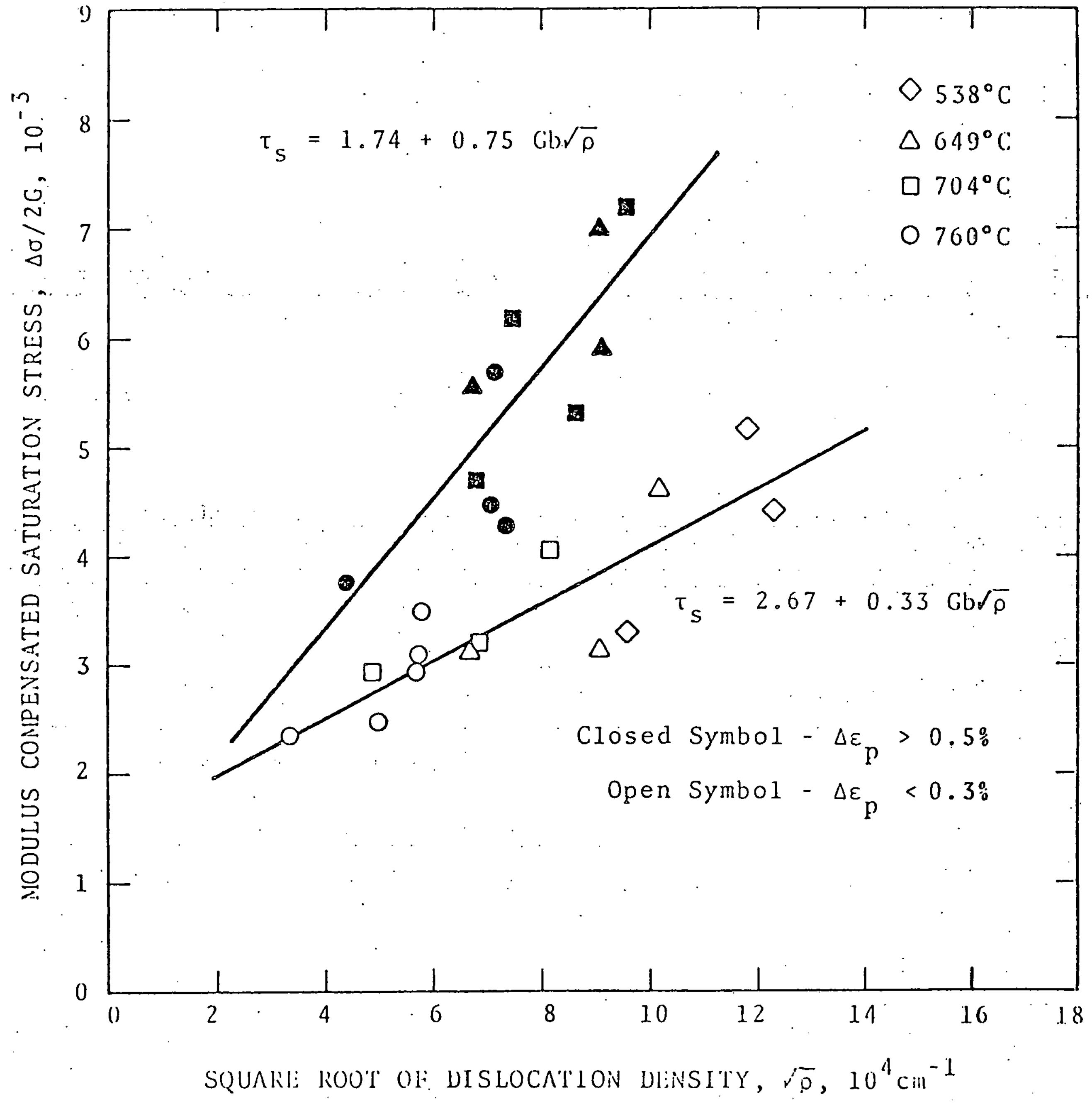

Fig. 11 The Shear Modulus Compensated Saturation Stress, $\Delta\sigma/2G$, as a Function of the Square Root of the Dislocation Density $\sqrt{\rho}$, for Incoloy 800.

INDEX

APPENDIX B

PROGRESS REPORT FOR PERIOD ENDING APRIL 30, 1976

7.1.1 INTRODUCTION

The objective of this program is to (a) evaluate the time, temperature and stress-dependent mechanical properties of reactor structural materials, (b) determine the relationship of these properties to the microstructure, (c) show the contribution of the microstructure to the internal stress fields and the subsequent influence on microcracking and the grain boundary sliding behavior during the normal plastic deformation at elevated temperatures and (d) demonstrate the relationship of the hot micro-hardness properties with the hot-tensile properties of a class of commercial and advanced alloys presently under investigation at other laboratories. Special consideration is being given to operating conditions typical of nuclear reactor applications, including the knowledge that radiation environment can influence the substructure of these metals, a circumstance which can lead to significant changes in the conventional mechanical property behavior.

7.1.2 EXPERIMENTAL PROGRAM

Transmission electron microscopy has been used as the primary tool to study the deformation substructure of reactor structural materials resulting from creep, fatigue and tensile testing at elevated temperatures. Complementary work using optical microscopy, scanning electron microscopy and hot-hardness testing has been performed to characterize the deformation and failure behavior. New work is underway to perform similar studies on the Commercial, the Developmental and the Fundamental alloys being evaluated in the National Alloy Developmental Program with particular attention on the application of hot-hardness measurement as a strength microprobe.

7.1.2.1 Further Analysis of Fatigue Substructure Data for Incoloy 800 (H. Nahm)

The relation between the cell intercept size and the flow stress may be appropriately described by an equation of the following form:

$$\lambda = k_o \left(\frac{\tau}{G} \right)^{-n} \qquad [7.1]$$

where k_o is a constant, τ is the shear stress and $\underline{n}$ takes a value between one and three. The value of one for $\underline{n}$ was theoretically predicted by Holt(1), Kuhlmann-Wilsdorf(2) and Langford and Cohen(3). Recently Young and Sherby(4) developed a model yielding $n = 2$. This general relationship has been experimentally confirmed both for the unidirectional deformation(3-14) and for the cyclic deformation(15-21) in a wide range of materials at various testing temperatures.

Recently it was observed in high temperature creep of AISI 304 and 316 stainless steels(9,13) that the dislocation cell or subgrain intercept, λ, has been related to the modulus compensated shear stress by the equations:

$$\lambda \simeq 12b\ (\tau/G)^{-1} \qquad [7.2]$$

for the case of subgrains, and

$$\lambda \simeq 5 \times 10^{-2} b\ (\tau/G)^{-2} \qquad [7.3]$$

for the case of cells, with the transition occurring at a value of τ/G equal to approximately 4.2×10^{-3}. The constant b is the Burgers vector.

The present results for the fatigued Incoloy 800 (Fig. 9 in reference 22) indicate that n is somewhat higher than 2 which is consistent with the results of Challenger and Moteff(10) for fatigued AISI 316 stainless steel at elevated temperature. The difference in the observed value of n is not known at the present time; it appears to be a complex function of the material, alloying and the applied stress as suggested by Young and Sherby(4). It is also possible that the difference might be from the fatigue deformation.

The subboundary intercept and the dislocation density were found to be a function of the plastic strain range employed as shown in Fig. 9 and Fig. 10, in the reference 22 respectively. The subboundary intercept initially increases and reaches a saturated value with increasing plastic range at constant value of $\Delta\sigma/2G$ (see Fig. 9 of the reference 22). Dislocation density shows the similar dependency on the plastic strain range (see Fig. 10 of the reference 22).

Despite the differences mentioned above, the general inverse relation between the cell size and the flow stress strongly indicates that a similar deformation mechanism is operating in both monotonic and cyclic deformation. Furthermore, a wide range of parallelisms of deformation mechanisms exist in either single phase or multi-phase materials(15,23-25). Feltner and Laird(15) interpreted their data for the high amplitude saturation stress observed in Cu and Cu-Al alloys by using Kuhlmann-Wilsdorf's(26) work hardening theory for stage II. Similarly, Calabrese and Laird(25) used Ashby's workhardening theory for plastically non-homogeneous materials(27) to explain the fatigue properties of a two phase alloy (Al - 4% Cu) with particles not penetrated by dislocations. It seems, therefore, quite reasonable to take a similar approach in correlating the present substructure data of Incoloy 800 with the observed fatigue properties.

Since Ashby's theory is going to be slightly modified in interpreting the present fatigue data, it is appropriate to briefly describe Ashby's workhardening theory for plastically non-homogeneous materials, especially for the case of materials with non-deformable plate-like particles. Most materials are "plastically non-homogeneous" because of the existence of the gradients of deformation due to microstructure. For example, the hard particles deform less than the matrix. This difference in deformation should be accommodated by "geometrically necessary" dislocations to allow compatible deformation of the different component in the matrix. Thus, most materials can be defined as "plastically non-homogeneous" possibly with the exception of single crystals. The other type of dislocations are called "statistically stored" dislocations which result from the mutual trapping of one another, often found in the uniform deformation of single crystal. When the accumulation of "geometrically necessary" dislocation becomes more than that of "statistically stored" dislocation, the former starts to be a controlling factor in the work-hardening behavior of materials.

The density of the "geometrically necessary" dislocations, ρ_G, is given by

$$\rho_G = \frac{1}{\lambda_G} \frac{4\gamma}{b} \qquad [7.4]$$

where γ is the shear strain, b is the Burgers vector, λ_G is "geometric slip distance" which is characteristic of microstructure. For the case of alloys with non-deforming plate-like particles, λ_G becomes the spacing between plates.

A theoretical relationship between the flow stress, τ, and the total dislocation density, ρ_T,

$$\tau = \tau_o + \alpha G b \sqrt{\rho_T} \qquad [7.5]$$

has been found to be true in a wide range of deformed FCC and BCC metals, where τ_o is the frictional stress, G is the shear modulus, b is the Burgers vector, α is a constant to be ~ 0.3 and ρ_T is the sum of the density of "geometrically necessary" dislocations, ρ_G, and that of "statistically stored" dislocations, ρ_s.

In case ρ_G is dominant, ρ_T becomes equal to ρ_G. Substituting equation [7.4] into [7.5], an equation of the type,

$$\tau = \tau_o + 2CG\sqrt{\left(\frac{b\gamma}{\lambda_G}\right)} \qquad [7.6]$$

is obtained where C is a constant. Equation [7.6] is Ashby's work-hardening theory for the plastically non-homogeneous materials. This relation shows the parabolic stress-strain relationship, often observed in the polycrystalline materials.

Similar to equation [7.4], a relation of the form,

$$\rho = \alpha\left(\frac{\gamma_p}{b\lambda'}\right)^m \qquad [7.7]$$

is assumed to follow in the cyclic deformation behavior of Incoloy 800, where ρ is the dislocation density, γ_p is the plastic shear strain amplitude, b is the Burgers vector, γ' is the cell or subgrain diameter from $\lambda' = 1.68\,\lambda$(1) and α,m are constants. The above assumption appears to be reasonable since the subboundaries, once formed, may play a role as barriers to mobile dislocations similar to the role of phases during deformation; and the dislocation density is expected to increase with increasing plastic strain range. It is not known at the present time, however, what the exact role of subboundaries is on plastic deformation.

Since the observations made by the TEM are essentially made inside a single crystal, the following relations were used to convert the stress and strain in Incoloy 800 into that of single crystal,

$$\Delta\sigma/2 = \sigma = M_p\ \tau_s \tag{7.8}$$

$$\gamma_p = M_p\ \varepsilon_p = M_p\ \frac{\Delta\varepsilon_p}{2} \tag{7.9}$$

where M_p is the numerical factor, $\Delta\sigma/2$ or σ is the saturation stress at half fatigue life, $\Delta\varepsilon_p/2$ or ε_p is the plastic strain amplitude, τ_s is the saturation shear stress for single crystal and γ_p is the saturation shear plastic strain for single crystal. The value of 3.1 for M_p calculated by Taylor(28) for FCC materials was used in the present study. This value may be approximate because M_p appears to be also a function of temperature(28).

In order to check the validity of the assumptions previously made, the dislocation density as a function of the parameters $(\gamma_p/b\lambda')$ for Incoloy 800 is plotted in Fig. 1. Experimental verification of equation [7.7] appears to be satisfactory from Fig. 1, considering the error involved in measuring the dislocation density.

If we substitute equation [7.7] into equation [7.5], the following type of equation is obtained

$$\tau_s/G = A\left(\frac{b\gamma_p}{\lambda'}\right)^n \tag{7.10}$$

This equation has a form similar to Ashby's workhardening theory, equation [7.6], except for the power relationship instead of the square root of the term $(b\gamma_p/\lambda')$.

A plot of the modulus compensated saturation shear stress versus the parameter $(b\gamma_p/\lambda')$ is given in Fig. 2. It is apparent that the data are in excellent agreement with the modified theory. The best fit line through least square analysis(29) was found to be

$$\tau_s = 2.4 \times 10^{-2}\, G \left(\frac{b\gamma_p}{\lambda'} \right)^{0.20 \pm 0.014} \qquad [7.11]$$

with the multiple correlation coefficient value of ∿ 0.95. Fatigue data on AISI 304 and 316 stainless steels by Challenger and Moteff(18,19) and on AISI 304 stainless steel by Nahm and Moteff(30) are included in Fig. 3 with the best fit line for the data on Incoloy 800. It is again evident that the data on the other austenitic stainless steels are well correlated with the modified theory. It is believed that the same type of fatigue mechanism is operating in austenitic stainless steels for a wide range of testing temperatures and test conditions.

At this point of discussion, it seems proper to discuss the influence of second phases in subboundary formation in Incoloy 800. Three types of precipitates (λ', $M_{23}C_6$ and TiN) are identified in fatigued Incoloy 800. Details of identification methods and the effect of precipitates on mechanical properties were discussed previously(31). Second phase formation during fatigue in Incoloy 800 appears not to affect the subboundary formation. The TEM observations and the evidence of a critical dislocation density for cell formation support this view. The lack of second phase effects on subboundary formation is also consistent with the cells that were observed in the dispersion hardened copper single crystal during fatigue(32-35).

The present result can be interpreted by the concept of "threshold" interparticle geometry as given by Ashby(27). Second phases control the hardening behavior when particle geometry is similar to that of dislocation cell structure and the interparticle spacing is less than or equal to the self-trapping distance of dislocations. When the spacing between the second phases is larger than the dislocation self-trapping distance (equivalent to the cell size) and the geometry of second phases is quite different from the cell structure, the cyclic behavior becomes that of the single phase materials. The present results on Incoloy 800 belong to the latter case. For example, the substructure observed during creep of Hastelloy X and Udimet 700 did not show any subboundary formation(36). The reason for this is that the geometry and size of second phases formed in these alloys is quite comparable with the geometry and size of the dislocation cell structure. It is, however, true that the second phase formation contributes to the increase in flow stress. The higher value of saturation shear stress in Incoloy 800 than in AISI 304 or 316 stainless steels, at constant value of the parameter $(b\gamma_p/\lambda')$ (see Fig. 3), could be attributed to the presence of a second phase such as small TiN particles formed in Incoloy 800.

7.1.2.2 Creep-Microstructure Evaluation of AISI 330 Stainless Steel (H. Jang)

The creep-microstructure evaluation has been initiated on AISI 330 stainless steel which was provided by Hanford Engineering Development Laboratory in the form of 1/4 in. diameter rods. Round creep test specimens were machined from these rods with a gage length 1.00 in. long by 0.125 in. diameter. The complete specimen dimensions are shown in Fig. 4. The specimens, wrapped in Ta foil, were given an annealing treatment at 1100°C for 1/2 hour in a vacuum of $\sim 1 \times 10^{-6}$ torr. No oxidation or discoloration of the specimens occurred during the annealing treatment.

A constant load creep rupture test was performed on a conventional lever type creep testing machine (Arcweld Model C creep-rupture tester) with one of the specimens at 649°C under an applied stress of 30,000 psi. The specimen was heated slowly from the room temperature to the test temperature and soaked overnight at that temeprature before the load was applied. The temperature was monitored by two chromel-alumel thermocouples fastened to the ends of the reduced section. Temperature variation along the gage length of the specimen was held to within ±1°C and temperature control was maintained within ±2°C during the entire test period. The specimen extension was monitored by two dial gages and one LVDT. One dial gage was placed on the load arm, and the other dial gage and the LVDT were attached to an extensometer which was clamped to the shoulders of the specimen. The dial gages had an accuracy of 2×10^{-4} in. and the LVDT had an accuracy of 6×10^{-5} in. The output of the LVDT was plotted on an X-Y recorder continuously during the test period. When ruptured, the specimen was cooled rapidly in order to preserve microstructures developed in the specimen during the test. An electric fan was used to assist the rapid cooling.

The strain vs. time curve for the specimen tested at 649°C with an applied stress of 30,000 psi is shown in Fig. 5. It shows small primary and secondary creep stages, and a very large tertiary creep stage. The creep rupture data are listed below:

Strain on loading: 1.63%

Strain at the end of primary stage: 2.6%
Time at the end of primary stage: 0.8 hr.

Strain at the end of secondary stage: 5.75%
Time at the end of secondary stage: 6.2 hrs.

Rupture strain: 64.3%
Rupture Life: 29.6 hrs.

Minimum creep rate: 1.04×10^{-4} sec^{-1}

Reduction in Area: 50.2%

A comparison of these data with those obtained from an AISI 304 stainless steel tested under the same test conditions shows that the rupture life of 330 SS is an order of magnitude longer than 304 SS, while the minimum creep rate is smaller by a factor of 6-7.

TEM evaluation of this creep-rupture specimen and another creep test at 500°C with an applied stress of 30,000 psi are presently being conducted. Also, other creep tests at a wide range of temperature and stress levles and the subsequent substructural studies are being planned.

7.1.2.3 Creep-Microstructure Evaluation of A286 (A. M. Ermi and H. Nahm)

Material was provided by the National Alloy Development Program Task Group, Hanford Engineering Development Laboratory in the form of ∿ 1mm thick sheets. Most of the time has been spent on the preparation of test specimens and heat treating of this precipitation strengthened stainless steel. The details of the specimens and preliminary creep data with microstructural correlation will be reported in future progress reports.

Before evaluating the creep-microstructure relationship the effect of ageing was studied. A set of specimens was solid-solution annealed at 900°C in air for 2 hours, oil quenched, aged at 720°C for various times, and air cooled. Fig. 6 shows the DPH hardness as a function of ageing time. It is apparent that rapid hardening occurs during the initial ageing period, the hardness increasing slowly thereafter.

Electron and optical microscopy are being performed to study the effects of the heat treatments on the microstructure.

7.1.2.4 Hot-Hardness Measurements on High Temperature Alloy Systems (R. Dorning)

One objective of the hot-hardness test is to determine the relative strength levels at different temperatures so that the initial test conditions for creep and hot tensile experiments can be established. Accordingly, hot-hardness measurements have been made on specimens fabricated from solution treated AISI 330 stainless steel and on aged A-286. The tests were performed in an Argon atmosphere at temperatures up to 1200°C. These results are presented in Fig. 7. The aged A-286 shows hardness levels which are about a factor of three greater than the AISI 330 stainless steel in the temperature range of about 200 to 900°C. The AISI 330 hardness values are very similar to that of annealed AISI 316 stainless steel and much lower than the 20% cold-worked 316 stainless steel as shown in Fig. 7.

7.1.3 REFERENCES

1. D. L. Holt, J. Appl. Phys., 41 (1970) 3197.
2. D. Kuhlmann-Wilsdorf, in "Work Hardening", Gordon & Breach (1968) 97.
3. G. Langford and M. Cohen, Trans. ASM, 62 (1969) 623.
4. C. M. Young and O. D. Sherby, J I S I, September (1973) 640.
5. D. J. Michel, J. Moteff and A. J. Lovell, Acta Met., 21 (1973) 1269.
6. K. D. Challenger and J. Moteff, Scripta Met., 6 (1972) 155.
7. K. D. Challenger and J. Moteff, ASTM STP 520 (1973) 68.
8. K. D. Challenger and J. Moteff, Met. Trans., 4 (1973) 749.
9. V. K. Sikka, H. Nahm and J. Moteff, Accepted for publication in Mat. Sci. Eng. (1975).
10. F. Garofalo, C. Richmond, W. F. Domis and F. von Gemmingen, Joint Int. Conf. on Creep, Inst. of Mech. Engrs., (1963) I-31.
11. L. J. Cuddy, Met. Trans., 1 (1970) 395.
12. M. R. Staker and D. L. Holt, Acta Met., 20 (1972) 569.
13. R. K. Bhargava, Ph.D. Thesis, University of Cincinnati, Cincinnati, Ohio (1975).
14. C. G. Schmidt, M.S. Thesis, University of Cincinnati, Cincinnati, Ohio (1975).
15. C. E. Feltner and C. Laird, Acta Met., 15 (1967) 1633.
16. P. Lukas and M. Klesnil, Phys. Stat. Sol., 21 (1967) 717.
17. A. Saxena and S. D. Antolovich, Met. Trans., 6A (1975) 1809.
18. K. D. Challenger and J. Moteff, Met. Trans., 3 (1972) 1675.

19. H. Abdel-Raouf, A. Plumtree and T. H. Topper, Met. Trans., 5 (1974) 267.

20. H. Abdel-Raouf and A. Plumtree, Met. Trans., 2 (1971) 1863.

21. H. Abdel-Raouf, T. H. Topper and A. Plumtree, ASTM STP 520 (1973) 300.

22. ORNL-5112, "Mechanical Properties Test Data for Structural Materials," Quarterly Progress Report for Period Endong January 31, 1976.

23. H. D. Nine and D. Kuhlmann-Wilsdorf, Can. J. Phys., 45 (1967) 865.

24. C. Calabrese and C. Laird, Mat. Sci. Eng., 13 (1974) 141.

25. C. Calabrese and C. Laird, Mat. Sci. Eng., 13 (1974) 159.

26. D. Kuhlmann-Wilsdorf, Trans. AIME, 224 (1962) 1047.

27. M. F. Ashby, Phil. Mag., 21 (1970) 399.

28. W. J. M. Tegart, in "Elements of Mechanical Metallurgy", McMillan Co., (1966) New York, 154.

29. Call/360 Version 2 Basic Library Programs, 2nd ed. (1970) G 320-1015-1, I.B.M., New York.

30. H. Nahm and J. Moteff, Unpublished Results, University of Cincinnati, Cincinnati, Ohio.

31. ORNL-5105, "Mechanical Properties Test Data for Structural Materials", Quarterly Progress Report for Period Ending April 30, 1975.

32. O. T. Woo, B. Ramaswami, O. A. Kupics and J. T. McGrath, Acta Met., 22 (1974) 385.

33. W. M. Stobbs and D. F. Watt, in "Proc. 2nd Int. Conf. on the Strength of Metals and Alloys", Vol. II (1970) 560.

34. W. M. Stobbs, D. F. Watt and L. M. Brown, Phil. Mag., 23 (1971) 1169.

35. O. T. Woo, O. A. Kupcis, B. Ramaswami and J. T. McGrath, "Proc. 2nd Int. Conf. on the Strength of Metals and

Alloys", Vol. II (1970) 659.

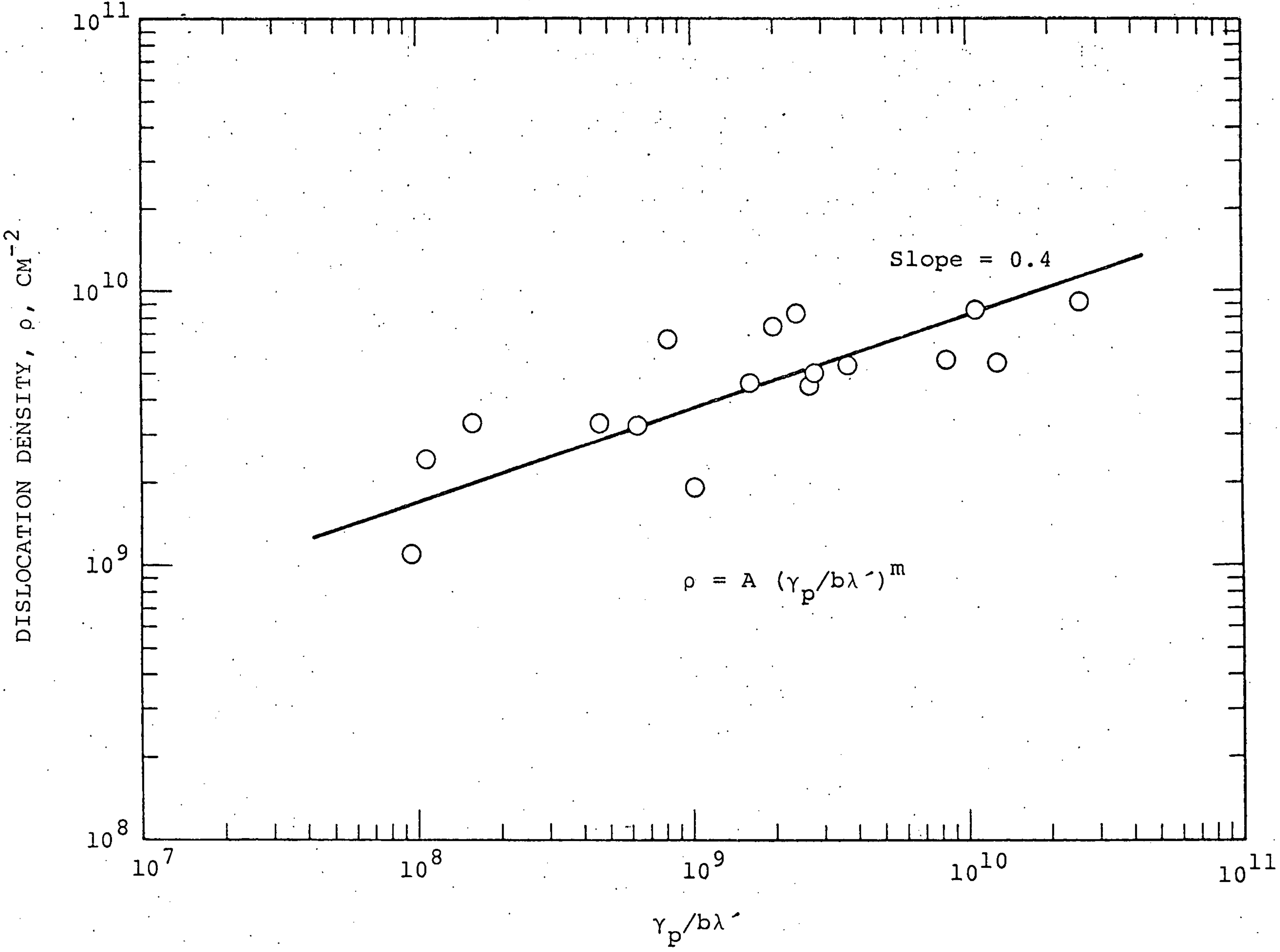

Fig. 1. Correlation of the Dislocation Density, ρ, with the Parameter $(\gamma_p/b\lambda')$

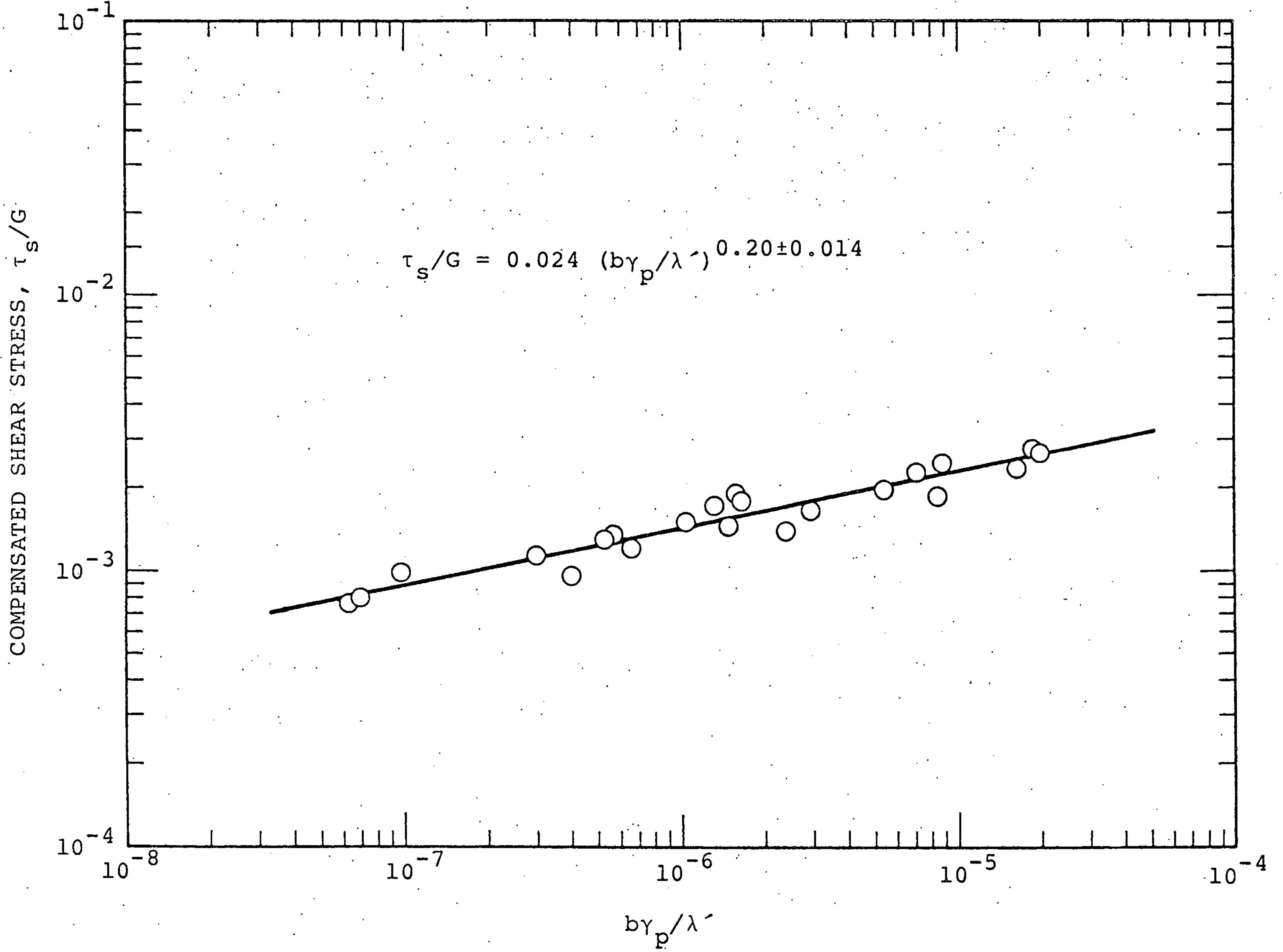

Fig. 2. Correlation of the Shear Modulus Compensated Saturation Shear Stress, τ_s with the Parameter (b

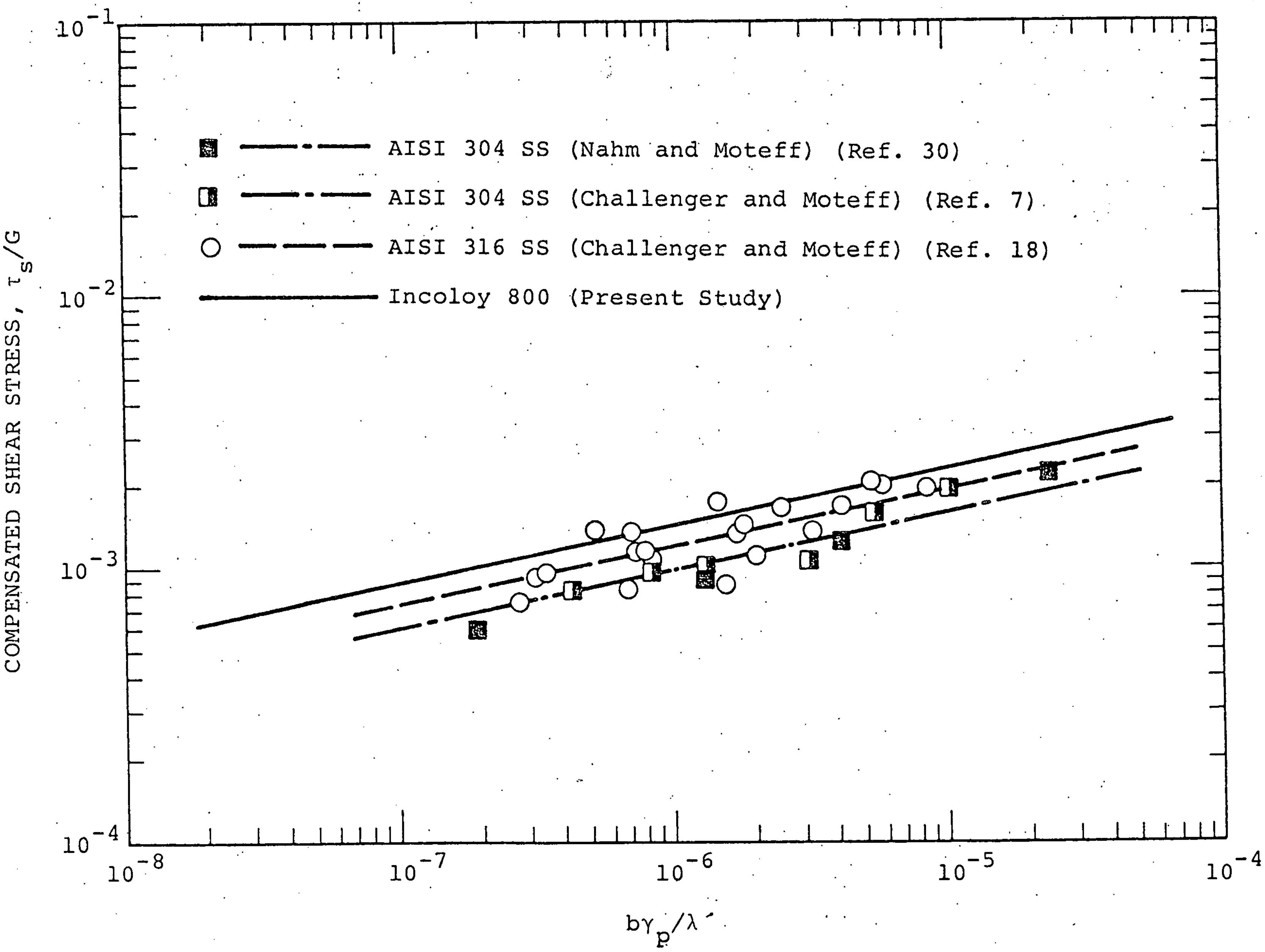

10^-1
10^-2
10^-3
10^-4
COMPENSATED SHEAR STRESS, τ_s/G
10^-8
10^-7
10^-6
10^-5
10^-4
bγ_p/λ'
▨ AISI 304 SS (Nahm and Moteff) (Ref. 30)
◧ AISI 304 SS (Challenger and Moteff) (Ref. 7)
○ AISI 316 SS (Challenger and Moteff) (Ref. 18)
Incoloy 800 (Present Study)

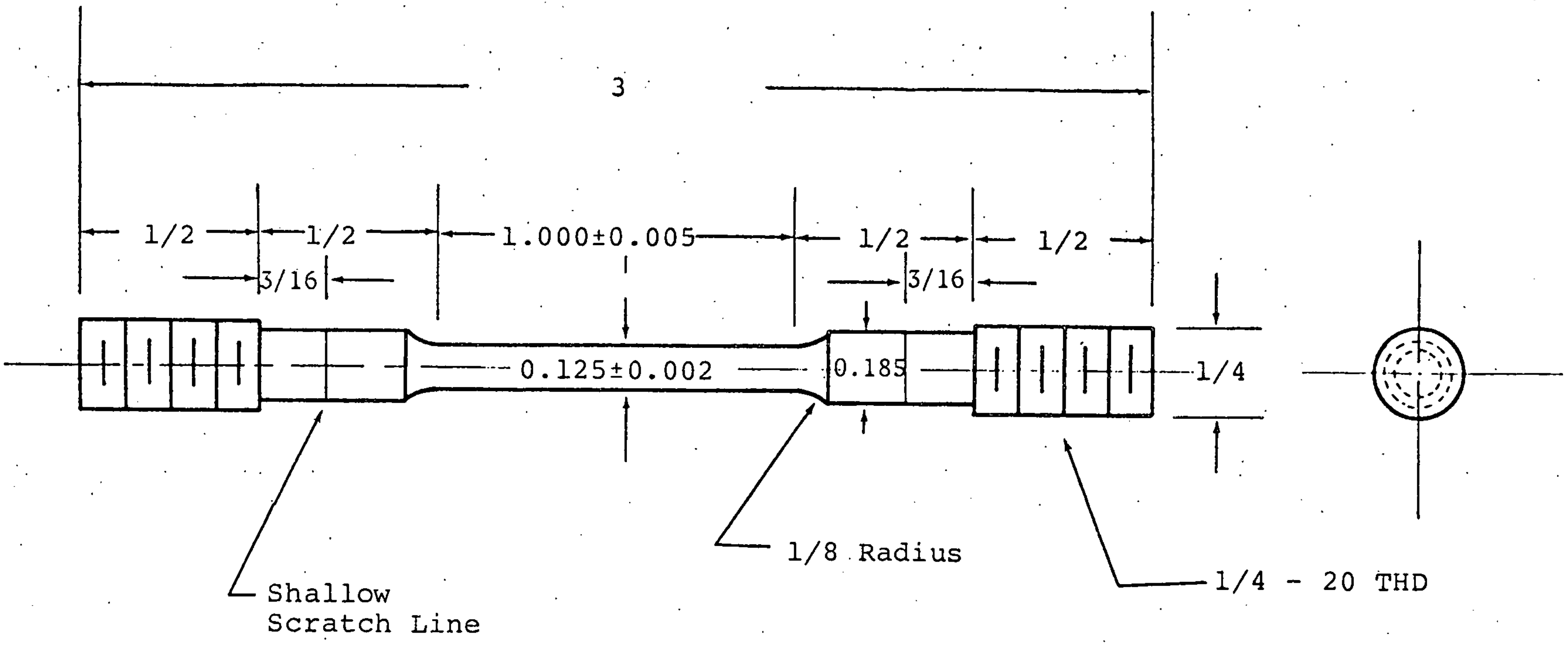

Fig. 4. Drawings of AISI 330 Stainless Steel Creep Test Specimen. (The dimensions are given in inches).

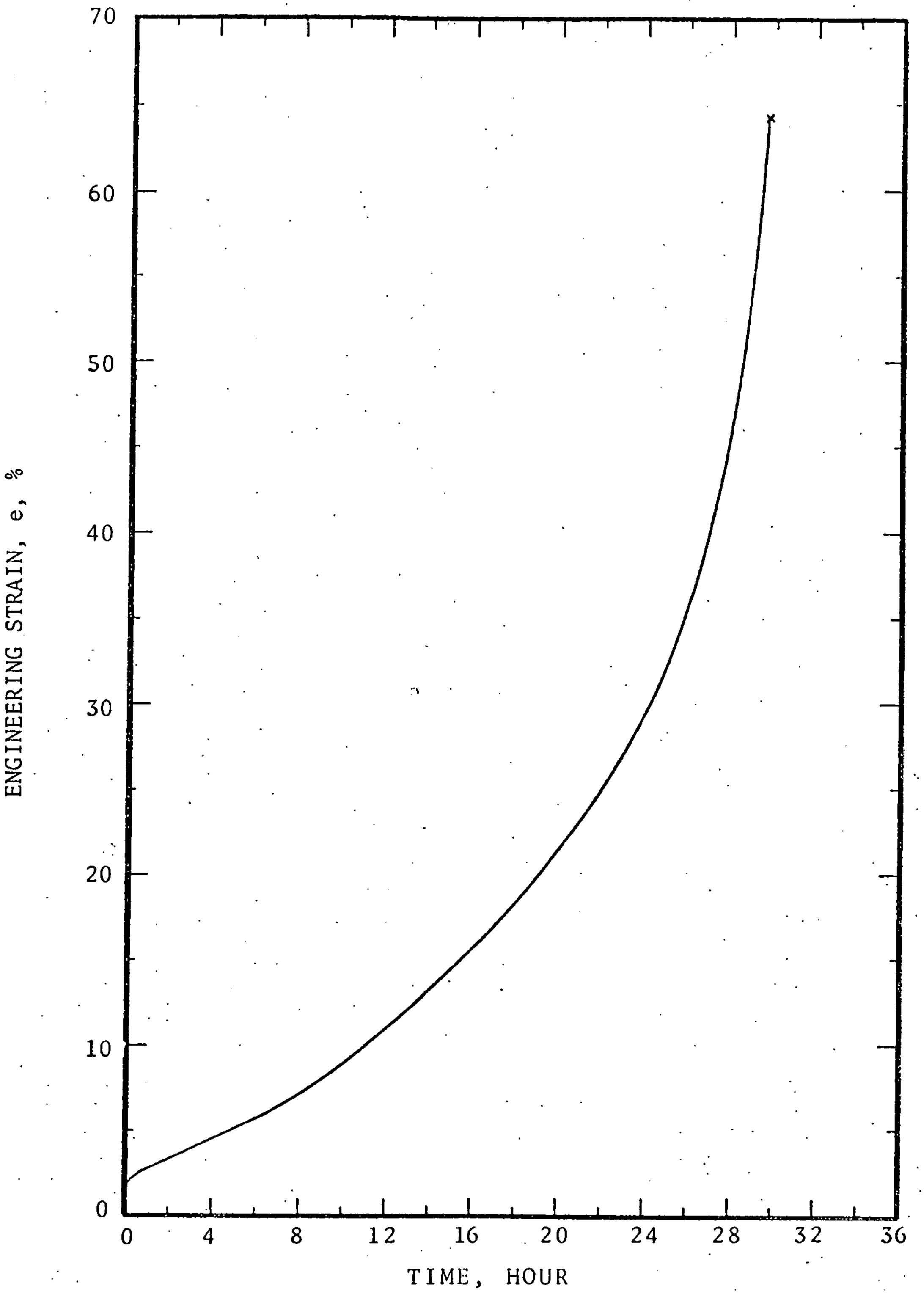

Fig. 5. Creep-Rupture Curve of AISI 330 Stainless Steel Tested at 649°C with an Applied Stress of 30,000 psi.

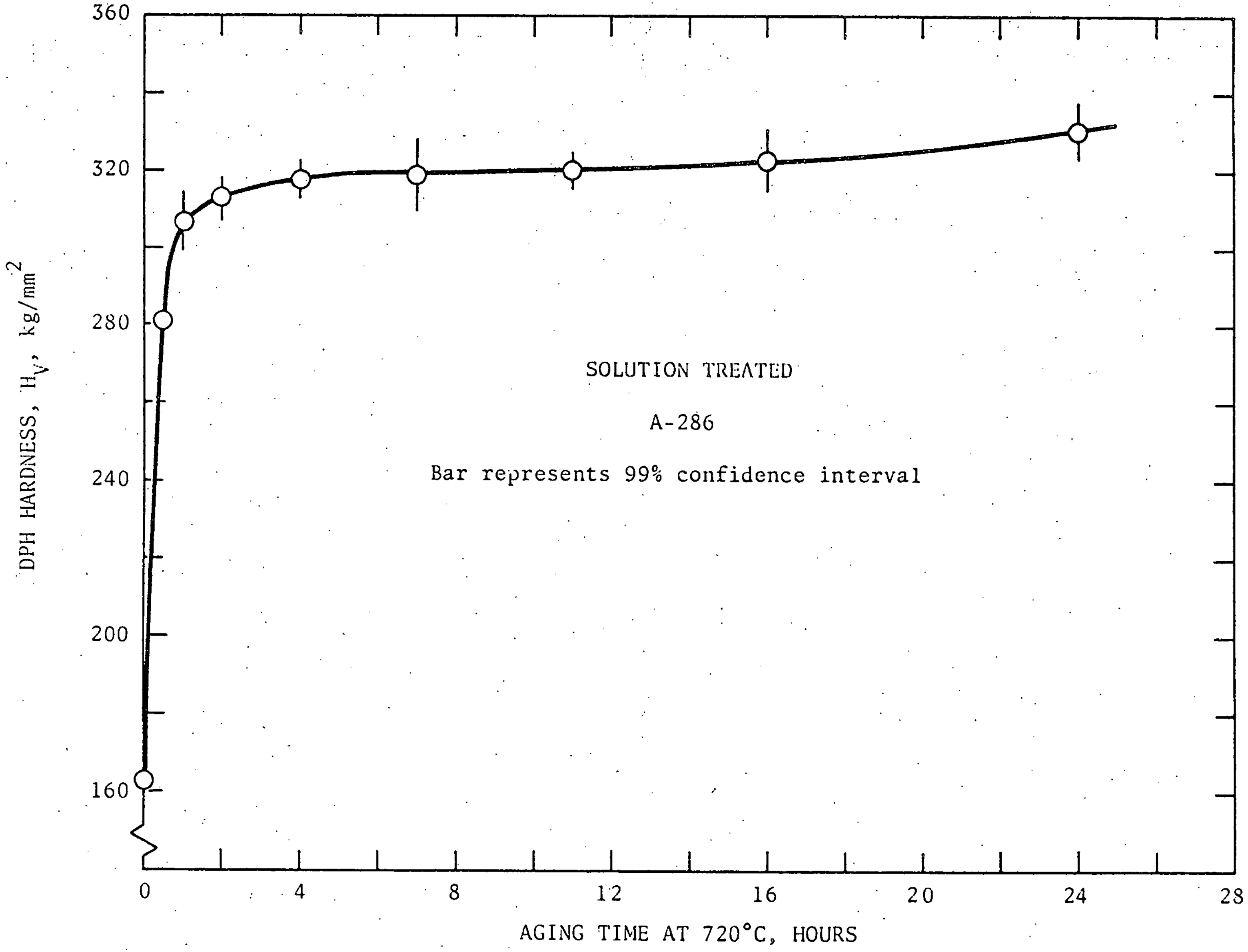

Fig. 6. DPH Hardness versus Aging Time at 720°C for Solution-Treated A-286

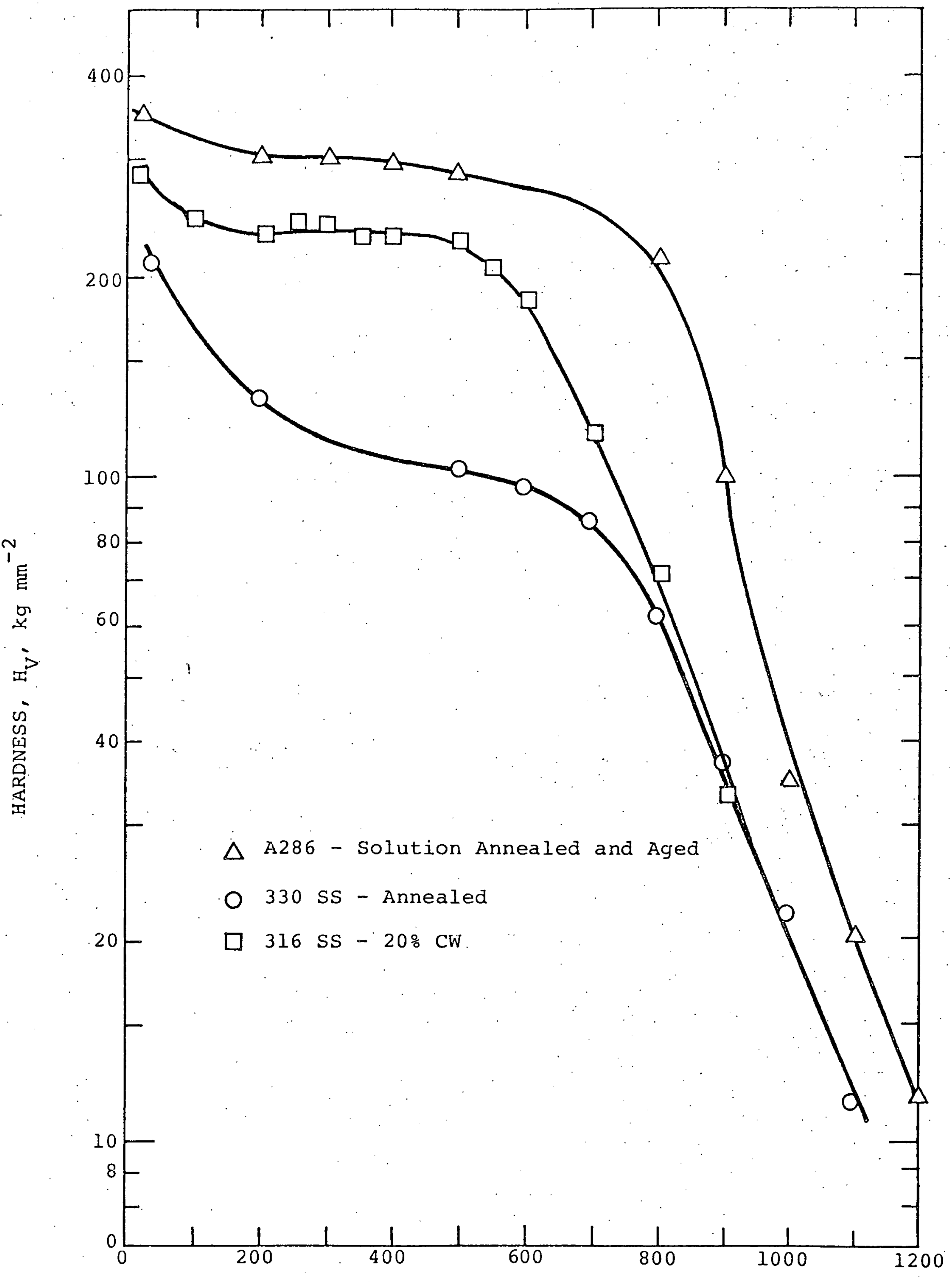

Fig. 7. Plot of Hardness versus Temperature for Several High Temperature Alloys.

APPENDIX C

PROGRESS REPORT FOR PERIOD ENDING JULY 31, 1976

7.1.1. INTRODUCTION

The objective of this program is to (a) evaluate the time, temperature, and stress-dependent mechanical properties of reactor structural materials, (b) determine the relationship of these properties to the microstructure, (c) show the contribution of the microstructure to the internal stress fields and the subsequent influence on microcracking and the grain boundary sliding behavior during the normal plastic deformation at elevated temperatures, and (d) demonstrate the relationship of the hot micro-hardness properties with the hot-tensile properties of a class of commercial and advanced alloys presently under investigation at other laboratories. Special consideration is being given to operating conditions typical of nuclear reactor applications, including the knowledge that radiation environment can influence the substructure of these metals, a circumstance which can lead to significant changes in the conventional mechanical property behavior.

7.1.2. EXPERIMENTAL PROGRAM

Transmission electron microscopy has been used as the primary tool to study the deformation substructure of reactor structural materials resulting from creep, fatigue, and tensile testing at elevated temperatures. Complementary work using optical microscopy, scanning electron microscopy, and hot-hardness testing has been performed to characterize the deformation and failure behavior. New work is underway to perform similar studies on the Commercial, the Developmental, and the Fundamental alloys being evaluated in the National Alloy Developmental Program with particular attention on the application of hot-hardness measurement as a strength microprobe.

7.1.2.1. Creep-Microstructure Evaluation of AISI 330 Stainless Steel

7.1.2.1. (A) Stress-Temperature Effects on Substructures

(B. Billings)

Table I shows the results of the creep-rupture testing completed to date. All testing was performed at 701°C with the exception of one sample which has been discussed elsewhere(1). The specimen geometry, type of creep testing machine, and testing methods pertinent to this work have been reported before(1). Figure 1 shows the creep curves obtained through this testing. It can be observed qualitatively that AISI 330 demonstrates the stress dependence of the overall creep rate as documented in the literature(2). However, as the present time period is being utilized mainly for raw data collection, a detailed interpretation of the experimental results will be withheld pending further data accumulation.

A limited amount of TEM observation has been performed on two (2) of the ruptured specimens: AN330-CB01 and AN330-

TABLE 7.I

AISI 330 RAW CREEP-RUPTURE TEST DATA, TEST TEMPERATURE 701°C (1294°F)

Sample Number	Applied Stress, ksi	e_p %	e_t %	$\dot{e}_s$ %/hr	t_2 hr	t_R hr	e_R %	RA %
AN330-CB01	40	5.0	12.0	83.7	0.15	0.25	60.0	44.1
-CB03	35	2.7	6.0	33.3	0.17	0.68	65.0	54.1
-CB02	30	1.5	2.7	8.82	0.85	2.90	64.0	56.4
-CB04	20	0.19	0.95	0.60	5.0	33.65	62.3	58.5

e_p = plastic loading strain
e_t = transient creep strain
$\dot{e}_s$ = minimum secondary creep rate
t_2 = time to reach end of secondary creep (0.2% offset)
t_R = time to rupture
e_R = rupture strain
% RA = % reduction in cross sectional area
NOTE: Values obtained through graphical methods

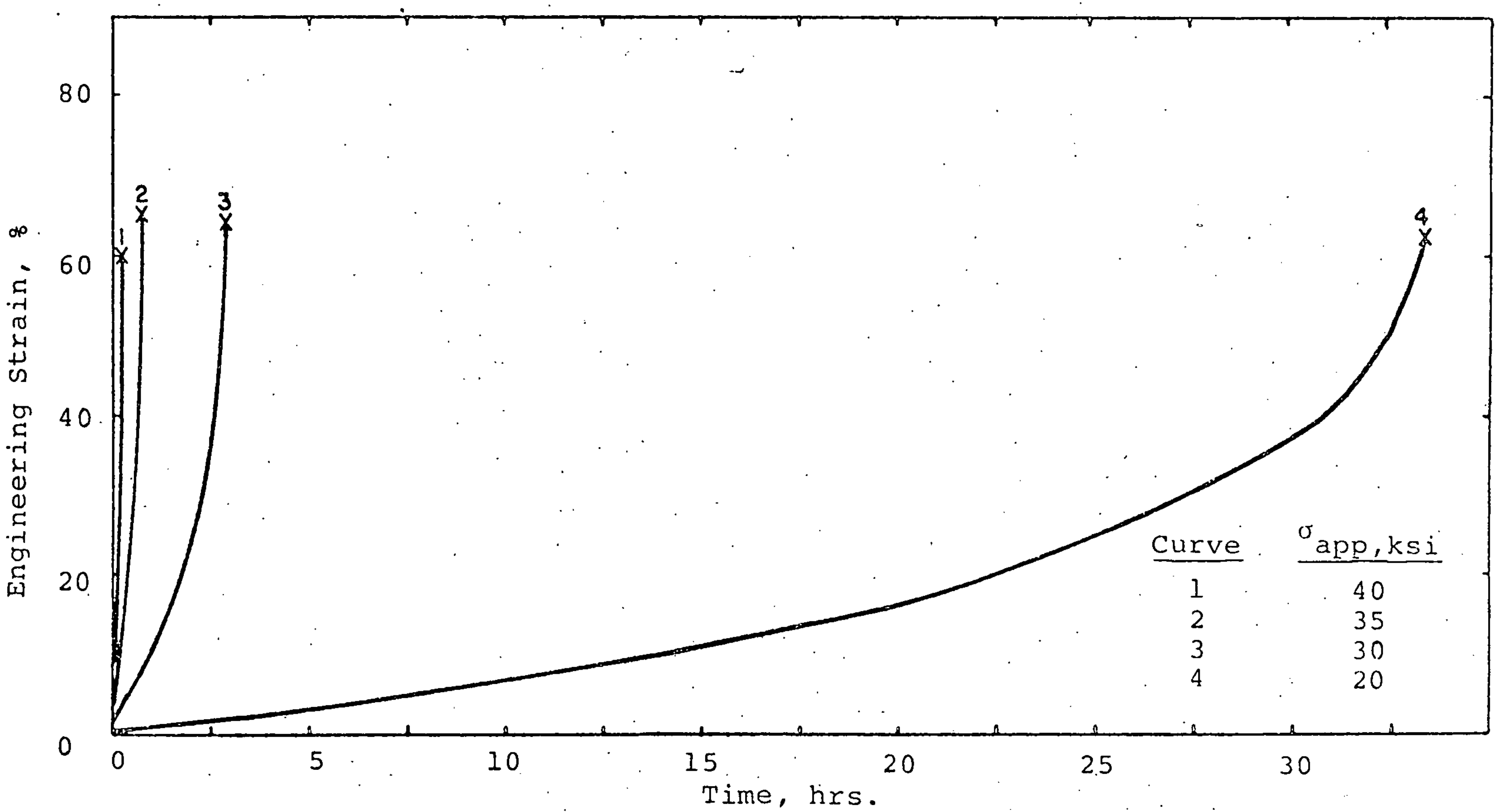

Fig. 7.1. Constant Load Creep-Rupture Curves for AISI 330 Stainless Steel Tested at Various Applied Stresses (σ_{app}) at 701°C.

CB04. These samples were tested at 40 ksi (275.8 MPa) and 20 ksi (137.9 MPa), respectively. The microstructure of the former was cellular in nature, while that of the latter was subgranular, as was expected. At the present time, however, no quantitative microscopy work will be discussed.

7.1.2.1. (B) A Study on Subgrain/Cell Development During Creep Deformation (J. Foulds)

The specimens for creep testing were machined from 1/4 in. dia. bar stock obtained from the Hanford Engineering Development Laboratory (reference heat = BB8951) and annealed at 1100°C ± 10°C and less than 1×10^{-6} torr in two batches of twelve specimens each.

Microstructural features will be observed and the grain size determined. Creep testing and TEM work will be carried out according to the plan described below.

The strain behavior of the material will be studied at a fixed temperature above 0.5 Tm and at two stress levels. The temperature and stress levels will be selected such that subgrains are obtained at one stress level and cells at the other, and such that the strain rates involved are not too high or too low to result in very short-term or long-term tests. For this, a few preliminary tests will be run using as a first approximation an Ashby deformation map for 304 SS and operating at temperatures and stress levels in the region of separation between dislocation glide and climb. Constant load creep tests will be run using an Arcweld model C creep-rupture tester, the electric furnace being of the zone controllable type and capable of a constant temperature zone of maximum variation ± 1°C over a length twice the specimen gage length.

The dislocation substructures will be studied at various points in the deformation process using a different specimen each time and stopping the test at the desired level of completion. The cross-marked points in Fig. 2 indicate the points at which substructure studies will be made,which with increasing strain,represent:

(i) Before test (annealed).
(ii) At start of primary creep stage.
(iii) At approximately 50% primary creep strain.
(iv) At completion of primary creep stage.
(v) At 50% secondary creep strain.
(vi) At completion of secondary creep.
(vii) At approximately 50% of tertiary creep strain.
(viii) At rupture.

At these strains the substructure will be evaluated with regard to

(i) Dislocation density.
(ii) Cell or subgrain size.
(iii) Misorientation between cells or subgrains.
(iv) The identification of any second phase formed and its effect on strain behavior.

These will enable a quantitative correlation between the

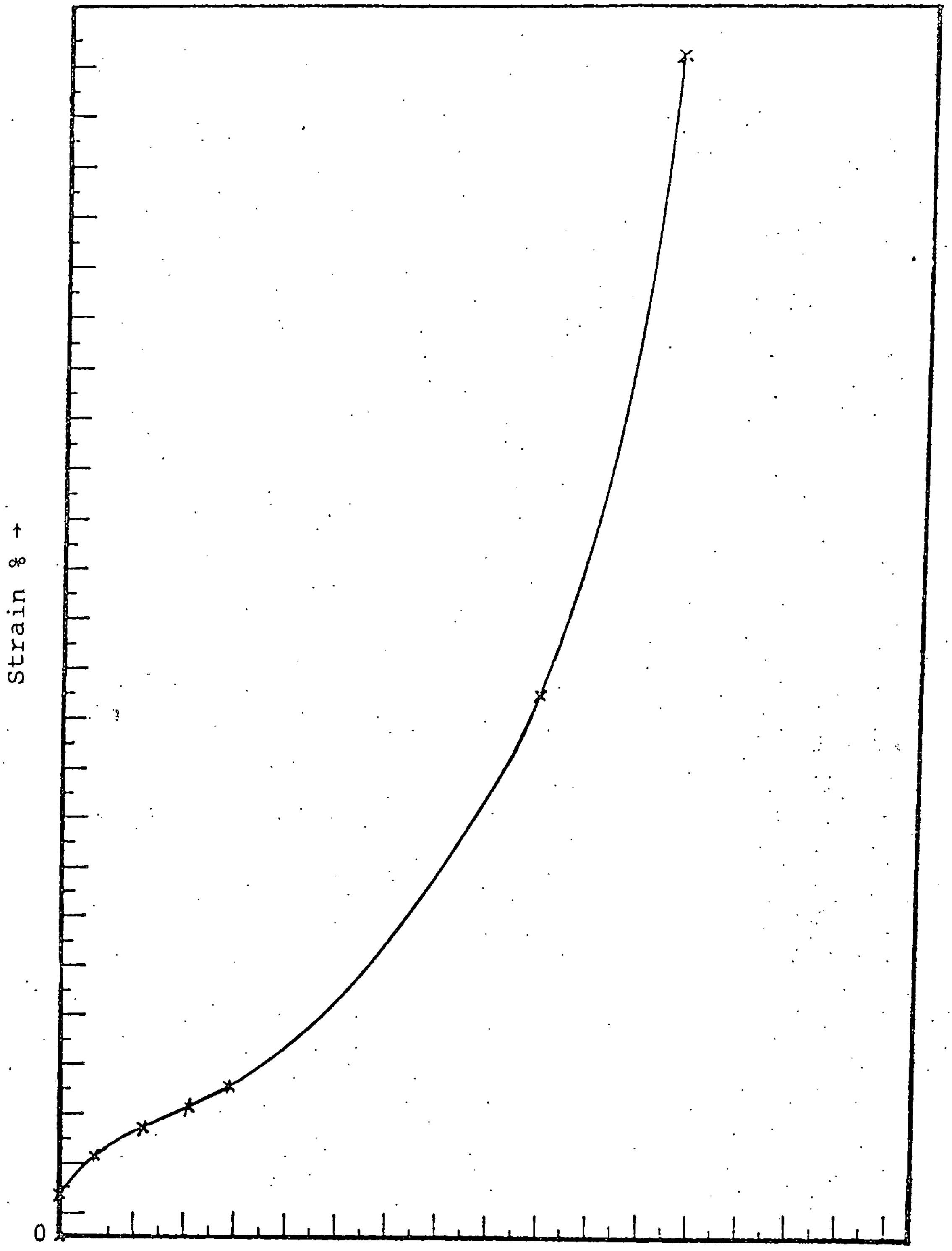

Fig. 7.2. Typical Creep Curve for AISI 330 Stainless Steel. X Denotes Strain Levels at Which Substructure Studies will be made.

various facets of substructure development and the observed strain behavior in the creep mode.

7.1.2.2. Activation Energy for Creep Calculated from Hot-Hardness Data (H. I. Jang)

Most of the empirical equations relating hardness with temperature are of the form:

$$H = Ae^{-BT} \qquad [7.1]$$

$$H = Ae^{B/T} \qquad [7.2]$$

$$H = A + B/T \qquad [7.3]$$

Although it is considered(3) that the Ito-Shishokin relationship (Equation 7.1) is the most satisfactory expression to fit the experimental data, it is difficult to interpret in terms of other metal characteristics(4). For a large number of metals, in fact, the data fit all three expressions quite well, and Equation 7.2 is suggestive of thermally activated deformation processes(4).

The influence of temperature on the hardness of AISI 330 SS is shown in Fig. 3. The logarithmic scale of hardness vs. 1/T is used in accordance with Equation 7.2. The shape of the hardness/temperature curve can be described as two straight lines intersecting at about 0.55 Tm. The inflection of the curve at around 0.5 Tm has been observed in many other metals, and it has been attributed to a change in the deformation mechanism from normal slip processes below the inflection to diffusion-controlled processes above the inflection. From

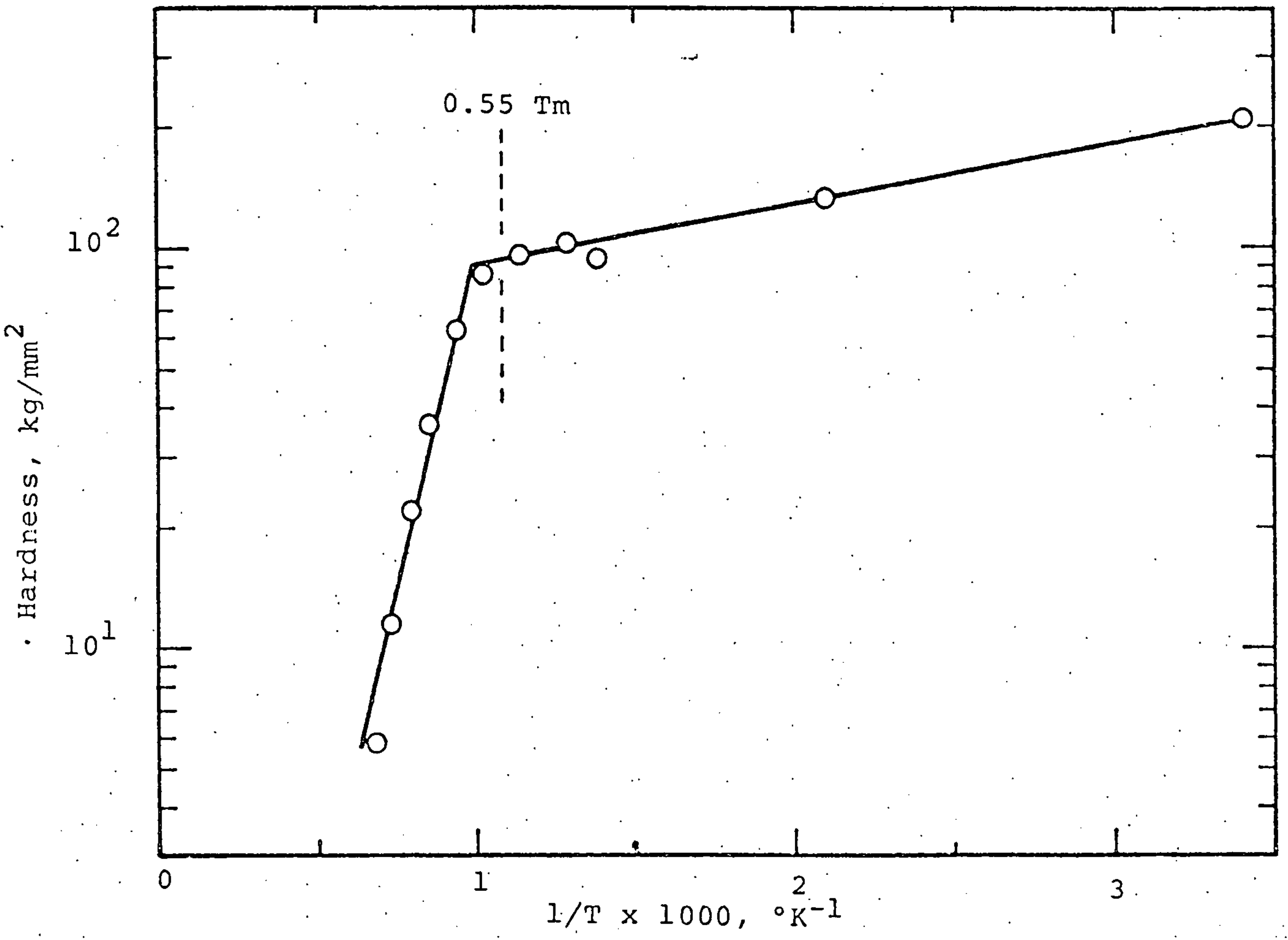

Fig. 7.3. Log Hardness of AISI 330 Stainless Steel Plotted Against 1/T.

the slope of the curve in Fig. 3, the "apparent activation energies for indentation hardness" were determined by using the Larsen-Badse relation(4):

$$H = Ae^{2Q'/RT} \qquad [7.4]$$

The results are:

$$Q' = 7.940 \text{ cal/mole for } T > 0.55 \text{ Tm}$$

$$Q' = 340 \text{ cal/mole for } T < 0.55 \text{ Tm.}$$

The apparent activation energy for indentation hardness is low, and this has been explained by Sherby and Armstrong(5). They have shown that the activation energy for creep can be determined from hot-hardness data above 0.75 Tm by using the expression

$$H/E = G \exp \frac{L}{nRT} \qquad [7.5]$$

The hot-hardness data of AISI 330 stainless steel above 0.5 Tm plotted as logarithm H/E vs. 1/T is shown in Fig. 4. As can be seen two straight lines can be drawn with a break occurring at about 0.75 Tm. In this plot the Young's modulus of AISI 304 SS(6) was used with an extrapolation to 1200°C. Utilizing Equation 7.5 with $n = 5$, the activation energy for creep of 93,400 cal/mole was obtained for $T > 0.75$ Tm.

7.1.2.3. Correlation of Hot-Hardness and Hot Tensile Strength of 2 1/4 Cr - 1 Mo Steel (R. Dorning)

Hot-hardness tests were performed in a high purity argon (99.999%) atmosphere on 2 1/4 Cr - 1 Mo steel at four different carbon levels between 0.009% and 0.135% by weight. The

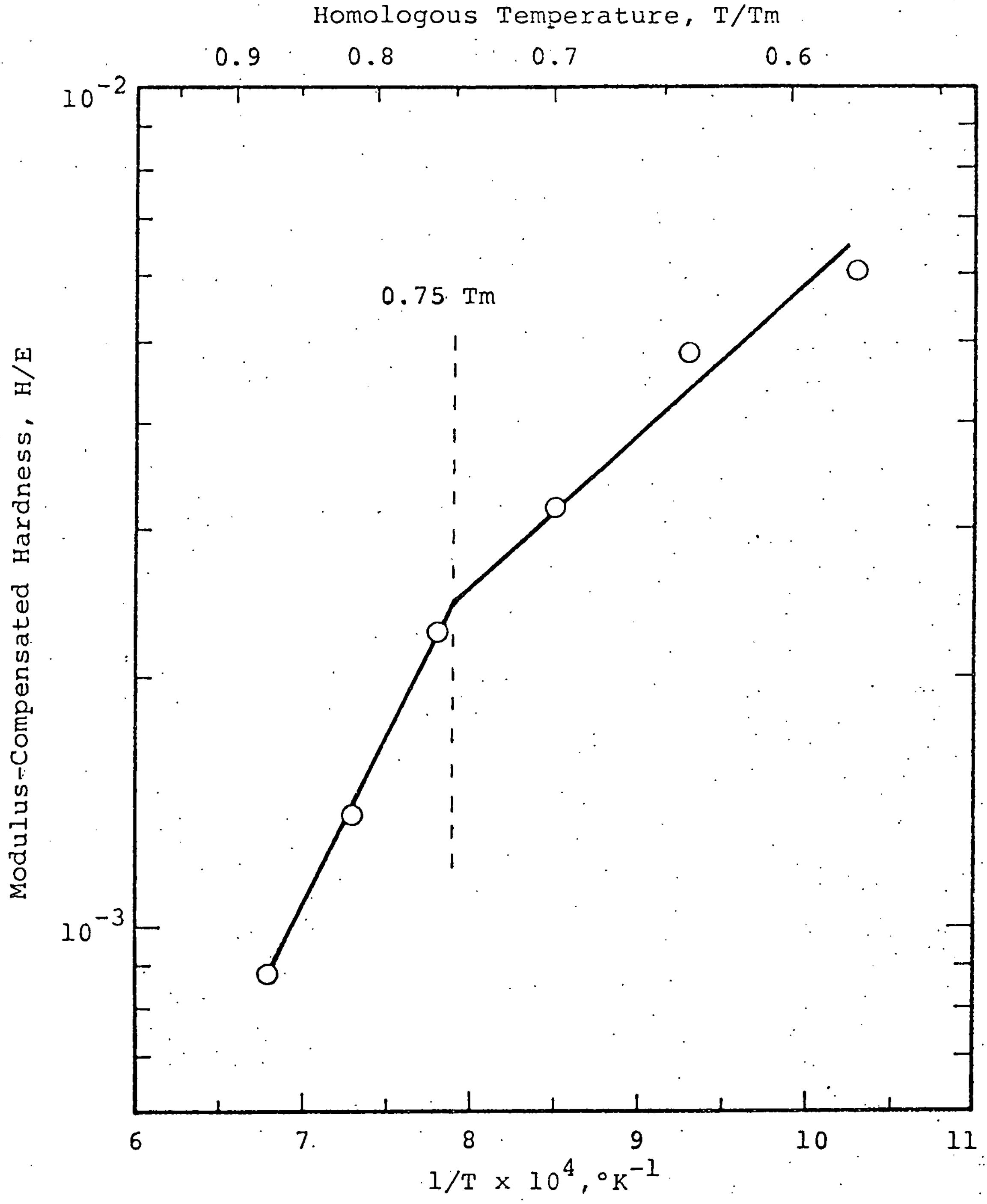

Fig. 7.4. Modulus-Compensated Hardness vs. 1/T of AISI 330 Stainless Steel.

hardness results are related to the tensile strength at six temperatures ranging from room temperature to 565°C by the relationship(7)

$$\sigma = \frac{H}{3}\left(\frac{n}{0.217}\right)^{n} \qquad [7.6]$$

As can be seen in Fig. 5, the correlation between UTS and hot-hardness is excellent for the high carbon (0.120% C) and the commercial (0.135% C) steels for all the temperatures tested. The medium (0.030% C) and low (0.009% C) carbon steels show good correlation at test temperatures above ∿ 350°C and fair correlation at the lower temperatures. Figure 6 shows the comparison between the UTS obtained from the tensile data and that calculated from the hot-hardness data for all four different carbon-level steels. A straight line is drawn with a 45° angle through the data points, and it can be seen that there is an excellent correlation between the experimental and the calculated tensile strength.

7.1.2.4. Grain Boundary Sliding in AISI 304 Stainless Steel

(J. Costa)

Preliminary grain boundary sliding (GBS) data has resulted from the testing of a direct-loading, ultra-pure argon atmosphere creep furnace. Creep specimens 2.5 x 0.5 x 25 mm long were machined from a 304 SS sheet. The sheet product form, after undergoing a series of cold rolling and annealing treatments, resulted in an average grain size of 93 microns. Specimens were mechanically polished, etched lightly, and a rectangular grid pattern was scribed by hand

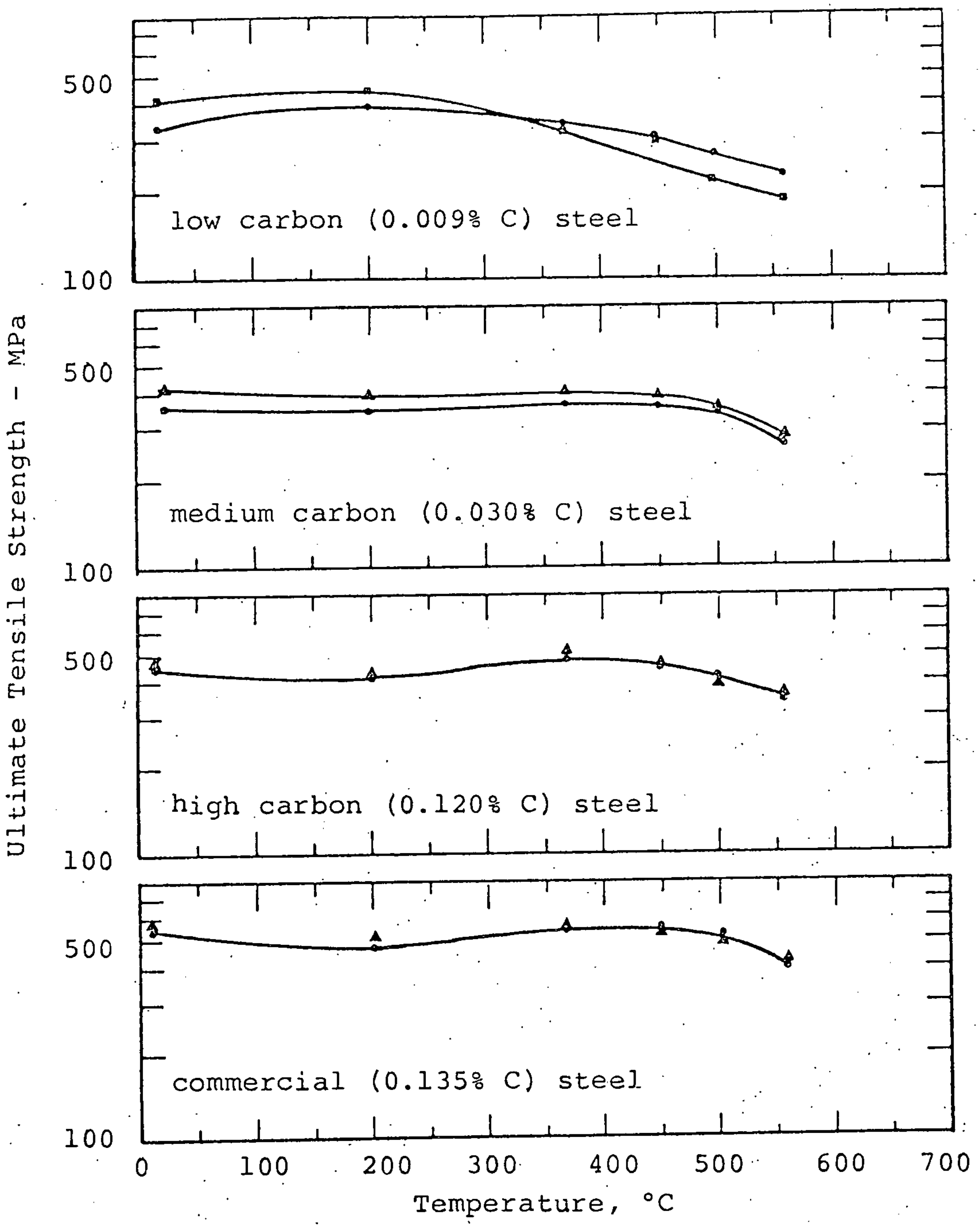

Fig. 7.5. Ultimate Tensile Strength of 2 1/4 Cr - 1 Mo Steels with Varying Carbon Contents Plotted Against Temperature. (⊙ - Experimental Data From R. L. Klueh; ▲,▣ - Calculated Values Based on Hot-Hardness Data)

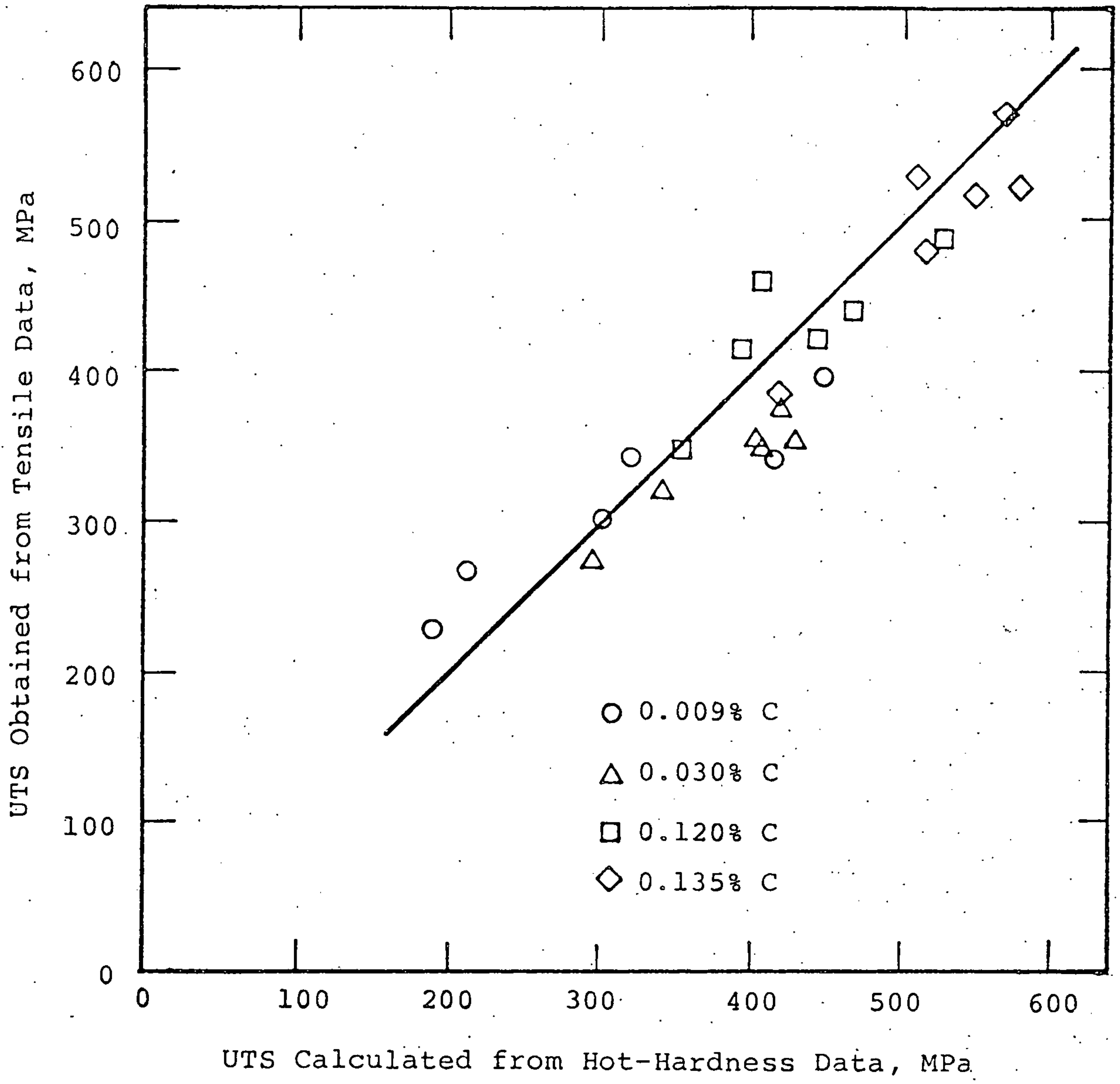

Fig. 7.6. Comparison of the Calculated and Experimental Tensile Strength of 2 1/4 Cr - 1 Mo Steels with Varying Carbon Contents in the Temperature Range of RT ∿ 565°C.

over the midsection using a SiC scriber.

The specimen was then heated to 750°C in an argon atmosphere and a 9,000 psi stress applied. At random intervals the testing was interrupted and the specimen removed. Using the traveling and optical microscopes, strain and grain boundary sliding parameters were measured. The offsets of both the transverse and longitudinal marker lines were measured and applied in Equation 7.7, previously used by Rachinger(8) and, in Equation 7.8, a simplified version from Stevens(9).

$$\varepsilon_{gb} = N_L \bar{l}_T \qquad [7.7]$$

$$\varepsilon_{gb} = 2\, N_L \bar{d}_L \qquad [7.8]$$

where N_L is the number of boundaries per unit length in the longitudinal direction, $\bar{l}_T$ is a mean value of the longitudinal component of displacement of a transverse line, $\bar{d}_L$ is a mean value of the transverse component of displacement of the longitudinal marker line.

It should be noted that these equations are applicable under specific assumptions. Present investigations are verifying the validity of these simplifying assumptions.

At least 400 total measurements were taken at the intersections of the grain boundary and the longitudinal and transverse marker lines to compute values for ε_{gb}. The single plot of $\bar{\varepsilon}_{gb}$ in Fig. 7 was the computed mean value of the results as obtained from Equations 7.7 and 7.8. Photomicrographs of the more distinguishable sliding grains were

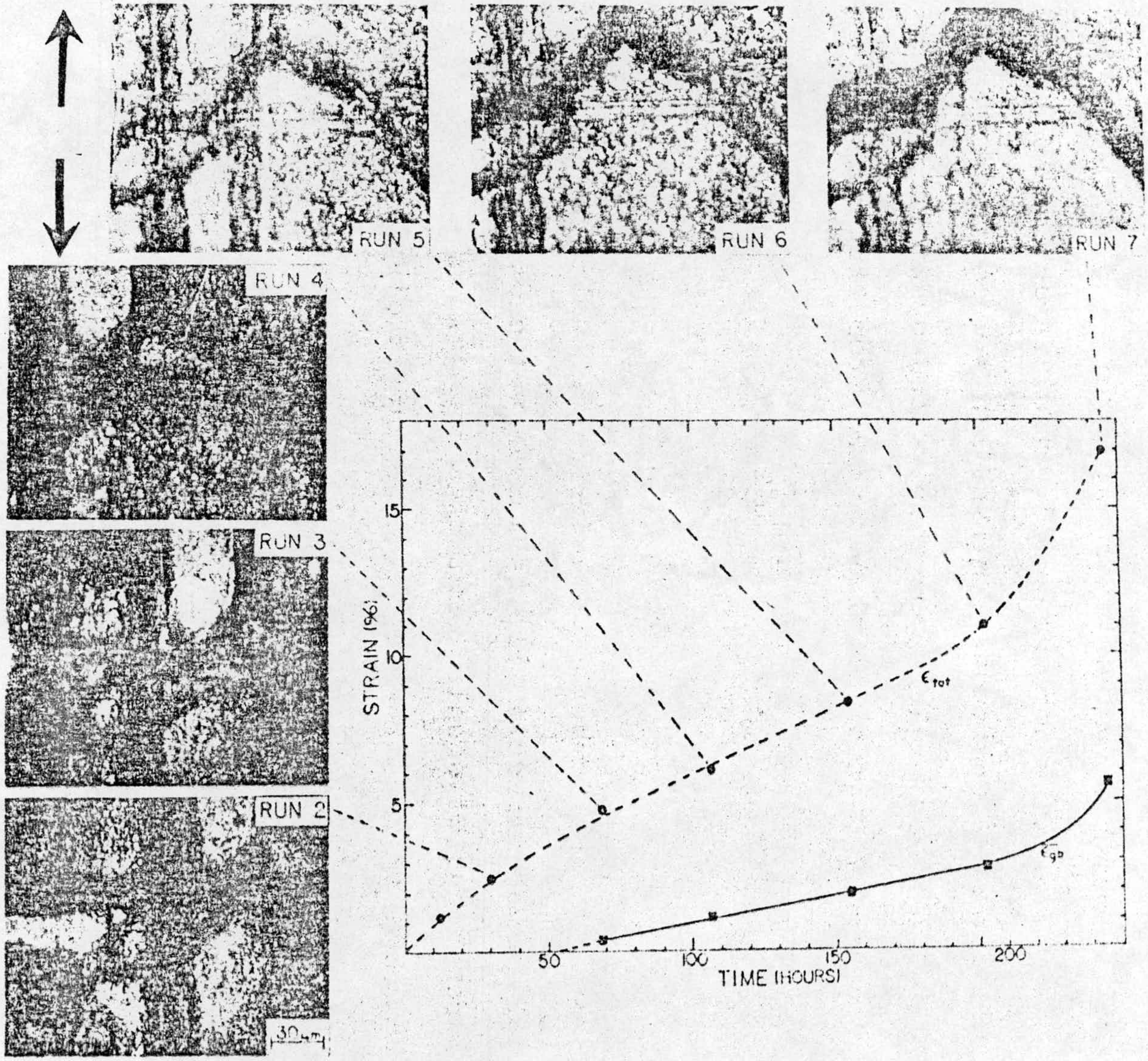

Fig. 7.7. Total Strain and Grain Boundary Sliding Behavior in AISI Stainless Steel Creep Tested at 9 ksi and 750°C.

included in Fig. 7.

Another fact to be emphasized is that only one specimen was employed in this test of interrupted runs which could appreciably affect the rupture life and total strain to rupture.

7.1.3. REFERENCES

1. Oak Ridge National Laboratory, Mechanical Properties Test Data for Structural Materials Quarterly Progress Report for Period Ending April 30, 1976, ORNL-5150, pp. 375-379.
2. F. Garofalo, Fundamentals of Creep and Creep-Rupture in Metals, The Macmillan Co., NY, 1965, pp. 46-66
3. J. H. Westbrook, Trans. Amer. Soc. Metals, 45 (1953) 221.
4. J. Larsen-Badse, Trans. JIM, 9 (1968) 312.
5. O. D. Sherby and P. E. Armstrong, Met. Trans., 2 (1971) 3479.
6. F. Garofalo, P. R. Malenock, and G. V. Smith, ASTM STP No. 129 (1952) 10.
7. J. R. Cahoon, Met. Trans., 3 (1972) 3040.
8. W. A. Rachinger, J. Inst. Metals, 81 (1952-53) 33.
9. R. N. Stevens, Met. Rev., II (1966) 133-136.

APPENDIX D

PROGRESS REPORT FOR PERIOD ENDING OCTOBER 31, 1976

7.1.1. INTRODUCTION

The objective of this program is to (a) evaluate the time, temperature, and stress-dependent mechanical properties of reactor structural materials, (b) determine the relationship of these properties to the microstructure, (c) show the contribution of the microstructure to the internal stress fields and the subsequent influence on microcracking and the grain boundary sliding behavior during the normal plastic deformation at elevated temperatures, and (d) demonstrate the relationship of the hot micro-hardness properties with the hot-tensile properties of a class of commercial and advanced alloys presently under investigation at other laboratories. Special consideration is being given to operating conditions typical of nuclear reactor applications, including the knowledge that radiation environment can influence the substructure of these metals, a circumstance which can lead to significant changes in the conventional mechanical property behavior.

7.1.2. EXPERIMENTAL PROGRAM

Transmission electron microscopy has been used as the primary tool to study the deformation substructure of reactor structural materials resulting from creep, fatigue, and tensile testing at elevated temperatures. Complementary work using optical microscopy, scanning electron microscopy, and hot-hardness testing has been performed to characterize the deformation and failure behavior. New work is underway to perform similar studies on the Commercial, the Developmental, and the Fundamental alloys being evaluated in the National Alloy Developmental Program with particular attention on the application of hot-hardness measurement as a strength microprobe.

7.1.2.1. Activation Energy for Creep of AISI 310 Stainless Steel and Inconel 718 Calculated from Hot-Hardness Data (R. Dorning)

Hot-hardness tests were performed in a high purity argon (99.999%) atmosphere on AISI 310 stainless steel and preliminary tests on Inconel 718. As shown in Fig. 7.1, the hardness curve of AISI 310 stainless steel is similar to that of AISI 330 stainless steel at temperatures above 300°C. The difference at lower temperatures is believed to be due to heat treatment variance. Sample preparation also effects the hardness at low temperatures since a cold work surface layer is introduced by cutting and polishing. Electro polishing was employed to minimize surface stress.

Tests above 0.75 Tm have been completed on Inconel 718 which displays the same general characteristics on the AISI 310 and 330 stainless steels at similar temperatures.

In a continuation of the work done on AISI 330 stainless steel the apparent activation energy for indentation hardness and the activation energy for creep have been calculated on

AISI 310 stainless steel and Inconel 718. The apparent activation energy for indentation hardness was determined using the Larsen-Badse relation(1)

$$H = A \exp^{2Q'/RT} \qquad [7.1]$$

where the slopes in Fig. 7.2 are equal to $2Q'/R$.

The results for AISI 310 stainless steel are

$Q' = 6{,}200$ cal/mole for $T > 0.55$ Tm

$Q' = 140$ cal/mole for $T < 0.55$ Tm

and for Inconel 718

$Q' = 6{,}100$ cal/mole for $T > 0.55$ Tm.

The low apparent activation energy for indentation hardness has been explained by Sherby and Armstrong(2). By using the expression

$$H/E = G \exp (Q/nRT) \qquad [7.2]$$

the activation energy for creep can be determined. The modulus compensated hardness data for AISI 310 stainless steel and Inconel 718 above 0.55 Tm versus 1/T are given in Fig. 7.3. The AISI 310 stainless steel displayed the same break at 0.75 Tm as the AISI 330 stainless steel (previous report). For a value of $n = 5$ in Equation 7.2, the activation energy for creep of 85,100 cal/mole for AISI 310 stainless steel and 63,500 cal/mole for Inconel 718 were obtained for $T > 0.75$ Tm.

7.1.2.2. A Study on Subgrain/Cell Development During Creep Deformation (J. Foulds)

Three tests were run to rupture on AISI 330 stainless steel at 652°C (0.57 Tm) and 35 ksi, the curves obtained being sufficiently identical to warrant the running of interrupted tests. Interrupted tests were run as shown in Fig. 7.4 and Table 7.I. Table 7.II contains the rupture data for the test (Specimen #AN330-CF01).

Interrupted tests at 652°C and 25 ksi have been postponed due to the variation obtained in the rupture data for the three tests run. The possible reasons for the variation are under investigation.

Straining during the interrupted tests was carefully monitored noting a less than 1 percent strain deviation from the curve in Fig. 7.4, indicating the validity of the microstructural data to be obtained from the tested specimens.

The fractured surface of the ruptured specimen AN330-CF01 indicated a highly (>95%) transgranular cracking mechanism when observed on the scanning electron microscope. Preliminary TEM observation on the same specimen revealed a "not so well defined" cellular structure with the presence of a second phase (not yet identified) having the same crystal structure as the matrix. All micrographs will be reported at the time of quantitative evaluation of the microstructural data.

With regard to the "as-annealed" material the grains were observed to be equiaxed with the average grain size = 87 microns measured both on longitudinal and diametrial sections while the average microhardness was found to be 128 DPH for the same.

7.1.2.3. Fatigue Crack Characteristics as a Function of the Fatigue Life of AISI 304 Stainless Steel Tested at 649°C (J. Costa)

This study was accomplished in conjunction with the high temperature fatigue substructure development work reported earlier(3). Since these tested specimens were used in this study, the reference heat number, heat treatment, and chemical analysis are the same.

Seven hour-glass specimens have been tested to different fractions of the fatigue life and to failure (complete separation) under the identical testing conditions of temperature (649°C), total strain range (2%), and cyclic strain rate ($4 \times 10^{-3} \text{sec}^{-1}$). The number of cycles at the termination of the respective fatigue tests and their test details are given in Table 7.II. All tests were initiated at the peak of the tension cycle, with the exception of the 1/4 cycle case.

Montages of the fractured surface, as photographed by a scanning electron microscope (Fig. 7.5), were assembled in order to count striation fringes. Recognizing that there is normally a one-to-one relationship between a striation and a fatigue cycle during crack propagation, the number of striations per unit length (dN/da) counted at various positions

positions along the montage was determined. This value, dN/da, called the striation density, was plotted against crack length, a, which produced a curve (Fig. 7.6 a) from which, by integration, Np(s), the number of cycles for crack propagation was calculated. Similarly, $\ell n(a)$ versus N plots were constructed as shown in Fig. 7 b, to determine N_o, the number of cycles to initiate a crack of length, a_o (∿ 1 grain diameter ≃ .1 mm). These techniques employed in separating N_o and Np were developed by other investigators(4-6).

The remaining six specimens interrupted before failure were sectioned and prepared for metallographic examination and for micro-hardness evaluation. Unetched metallographic specimens showed the development of a crack during crack initiation and propagation periods (Fig. 7.7). Maximum observable crack lengths at various cyclic times agreed with the predicted values calculated using the $\ell n(a)$ versus N plots. Furthermore, Tukon micro-hardness measurements correlated well with stress amplitude readings at interruption (Fig. 7.7) and with the substructure development investigated by Nahm.

7.1.2.4. Stress-Temperature Effects on Substructures

(B. Billings)

Table 7.III presents the raw creep data accumulated to date for AISI 330 stainless steel. The stress levels used in the constant load tests range from 10 ksi (69.9 MPa) to 40 ksi (279.4 MPa). Three test temperatures have been used at

present: 652°C (.58 Tm), 701°C (.6 Tm), and 800°C (.66 Tm). In addition to the data in Table 7.III, one test is presently in progress: sample number AN330-CB08, σ_a = 20 ksi, T = 600°C, e_p = 1.1%. This test has been underway for over 500 hours with an observed total strain of 1.6%. The sample geometry and testing procedures used to generate these data are reported elsewhere(7).

Figure 7.8 shows the constant load creep curves for the previously unreported specimens in Table 7.III, i.e. for specimens numbered AN330-CB05, 06, and 07. For the test conditions of these specimens see Table 7.III.

Figure 7.9 and Fig. 7.10 show the dependencies of the steady state creep rate and the time to rupture, respectively, on the applied stress.

In Fig. 7.9 the relationship between the steady state creep rate and the applied stress may be given by a power law as:

$$\dot{\varepsilon}_s = A\sigma_a^{\ n}$$

where $\dot{\varepsilon}_s$ is the steady state creep rate (hr^{-1}), σ_a is the applied stress (psi), n is a dimensionless constant, and A is a constant ($psi^{-n}hr^{-1}$).

In the present case,

$$\text{at } T = 800°\text{C} \qquad \dot{\varepsilon}_s = 8.7 \times 10^{-32}(\sigma_a)^{7.13}$$

$$\text{at } T = 701°\text{C} \qquad \dot{\varepsilon}_s = 1.23 \times 10^{-34}(\sigma_a)^{7.35}$$

It should be noted that these equations are the result of a least squares fit to a relatively small number of data points. Therefore, the accuracy of the values of A and n and the equations above is limited. As more creep rupture data is generated, these equations will be significantly refined.

In Fig. 7.10 the relationship between the time to rupture can be interpreted in terms of a power law of the form:

$$t_R = A\sigma_a^{-n}$$

where t_R is the time to rupture (hours), σ_a is the applied stress (psi), n is a dimensionless constant, and A is a constant ($(\text{psi})^n$hr). Again, it should be noted that the equations for the curves are the result of an analysis of a small number of data points, hence they are inherently uncertain. Moreover, the power law equation itself is not sufficient to explain the stress dependence of the rupture life(8). Various parameters have been used to obtain the rupture life from the stress. Examples of such parameters are the Larson-Miller, the Manson-Succop, and the Orr-Sherby-Dorn parameters(9). However, the power law fit yields a first approximation of the functional dependency of the time to rupture on stress for the 330 alloy for a small data population.

Figure 7.10 actually shows the inverse relationship of that proposed above. The figure is plotted after Garofalo(8) and it can be noted that no change in slope occurs in any one curve. This indicates that the fracture mode remained constant for all samples tested at the same temperature(10).

The fracture surfaces of the ruptured samples from Table 7.III have been observed in the Scanning Electron Microscope (SEM). The major fracture mode observed was the transgranular mode.

Figure 7.11 is a plot of the secondary creep rate versus the reciprocal temperature. After Garofalo$^{(8)}$, the slope of this curve is equal to $-\frac{\Delta H_c}{R}$ where ΔH_c is the apparent activation energy for creep (cal/mole) and R is the gas constant. This is only true if it is assumed that temperature has no effect on the substructure developed during steady state creep. Because of this assumption, Fig. 7.11 is shown at a constant applied stress. The slope calculations from this figure yield an activation energy ΔH_c = 100 kcal/mole. This value for ΔH_c is in good agreement with that obtained from hot hardness measurements on the same alloy (93.4 kcal/mole)$^{(11)}$. However, it must be noted that only three data points have been used to define the curve in Fig. 7.11. The curve was fit to these points by a least squares method, hence the ΔH_c = 100 kcal/mole value obtained from the curve may be slightly uncertain.

A limited study into the cracking behavior of AISI 330 has been initiated. It is known that the cracking characteristics of an alloy depend on the stress, temperature, and strain-rate conditions to which the alloy is subjected$^{(12)}$. The rupture of an alloy is directly related to growth and interlinking of cracks which appear during deformation$^{(13,14)}$. Hence, an investigation into the cracking behavior of AISI

330 stainless steel is appropriate.

No quantitative microstructural evaluation is available at this time.

7.1.3. REFERENCES

1. J. Larsen-Badse, Trans. JIM 9 (1968) 312.

2. O. P. Sherby and P. E. Armstrong, Met. Trans. 2 (1971) 3479.

3. H. Nahm, Ph.D. Thesis, University of Cincinnati, Cincinnati, Ohio (1975).

4. P. S. Maiya, Scripta Met. 9 (1975) 1141.

5. P. S. Maiya, Scripta Met. 9 (1975) 1277.

6. J. Moteff, H. Nahm, and A. Ermi, paper in preparation.

7. Oak Ridge National Laboratory, Mechanical Properties Test Data for Structural Materials Quarterly Progress Report for Period Ending April 30, 1976, ORNL-5150, pp. 374-379.

8. F. Garofalo, Fundamentals of Creep and Creep-Rupture in Metals, The Macmillan Company, New York, 1966, pg. 211.

9. M. K. Booker, C. R. Brinkman, and V. K. Sikka, Correlation and Extrapolation of Creep Ductility Data for Four Elevated-Temperature Structural Materials, Symposium on Structural Materials for Service at Elevated Temperatures in Nuclear Power Generation, ASME, 1975, pp. 108-145.

10. R. E. Reed-Hill, Physical Metallurgy Principles, D. Van Nostrand Company, New York, 1964, pg. 879.

11. Oak Ridge National Laboratory, Mechanical Properties Test Data for Structural Materials Quarterly Progress Report for Period Ending July 31, 1976, ORNL-5200, pg. 372.

12. H. Nahm, M.S. Thesis, University of Cincinnati, Cincinnati, Ohio (1973).

13. H. Nahm, D. J. Michel, and J. Moteff, J. of Material Science 8, (1973) 104-108.

14. U. Lindborg, Acta Met. 17 (1969) 157-165.

INDEX

TABLE 7.I

AISI 330 INTERRUPTED TEST DATA AT 652°C AND 35 KSI

Sample Number	e%	t hr.	R.A.%	Expected e% from Fig. 7.4
AN330-CF02	21.10	9.0	19.44	18.90
-CF03	10.30	3.5	8.40	10.95
-CF04	9.85	2.25	10.90	10.20
-CF05	8.80	1.0	7.80	9.40
-CF06	7.60	0.3	6.80	8.65
-CF07	7.30	0.0	7.04	7.80

e = Strain at interruption.

t = Time of test.

RA = Reduction in cross-sectional area.

TABLE 7.II

LOW CYCLE FATIGUE DATA FOR
AISI 304 SS (9 T 2796) TESTED IN AIR AT 649°C

Number of Cycles at Interruption(b) N, (Cycles)	Number of Surface Cracks(c)	Number of Surface Cracks per (mm^2)	Largest Crack (μm)
0	0	0	0
1/4	0	0	0
3/4	0	0	0
2 3/4	0	0	0
6 3/4	8	0.25	3
80	66	2.11	20
361	138	4.41	147
722(a)	165	4.46	350

(a) This specimen was tested until failure.

(b) All tests were initiated in the compression mode and interrupted at the peak of tension cycling with the exception of the 1/4 cycle care which was terminated at the end of compressive cycling.

(c) All specimens were examined in the polished condition at 1000X mag.

TABLE 7.III

AISI 330 RAW CREEP-RUPTURE TEST DATA

Sample Number	Applied Stress, ksi	Temp. °C[°F]	e_p %	e_t %	$\dot{e}_s$ %/hr	t_z hr	t_R hr	e_r %	RA %
AN330-CB01	40	701[1294]	5.0	12.0	83.7	0.15	0.75	60.0	44.1
-CB02	35		1.5	2.7	8.82	0.85	2.9	65.0	56.4
-CB03	30		2.7	6.0	33.3	0.17	0.68	64.0	54.1
-CB04	20		0.19	0.95	0.605	5.0	33.6	62.3	58.5
-CB05	15		1.13	3.5	0.057	41.5	251.1	62.5	52.2
-CB06	20	800[1472]	0.45	3.5	39.8	0.2	0.75	70.5	60.2
-CB07	10		0.09	1.55	0.284	24.8	64.9	30.3	31.0
-CF01	35	652[1206]	7.8	9.4	0.618	4.8	13.2	34.0	36.15

---

e_p = Plastic loading strain.

e_t = Cumulative strain at end of primary creep.

$\dot{e}_s$ = Minimum secondary creep rate.

t_2 = Time to reach end of secondary creep.

t_R = Time to rupture

e = Rupture strain

e_R = Rupture strain.

%RA = % reduction in cross-sectional area

NOTE: Values obtained through graphical methods.

report. Finally, a limited study on the cracking behavior of this material has been initiated.

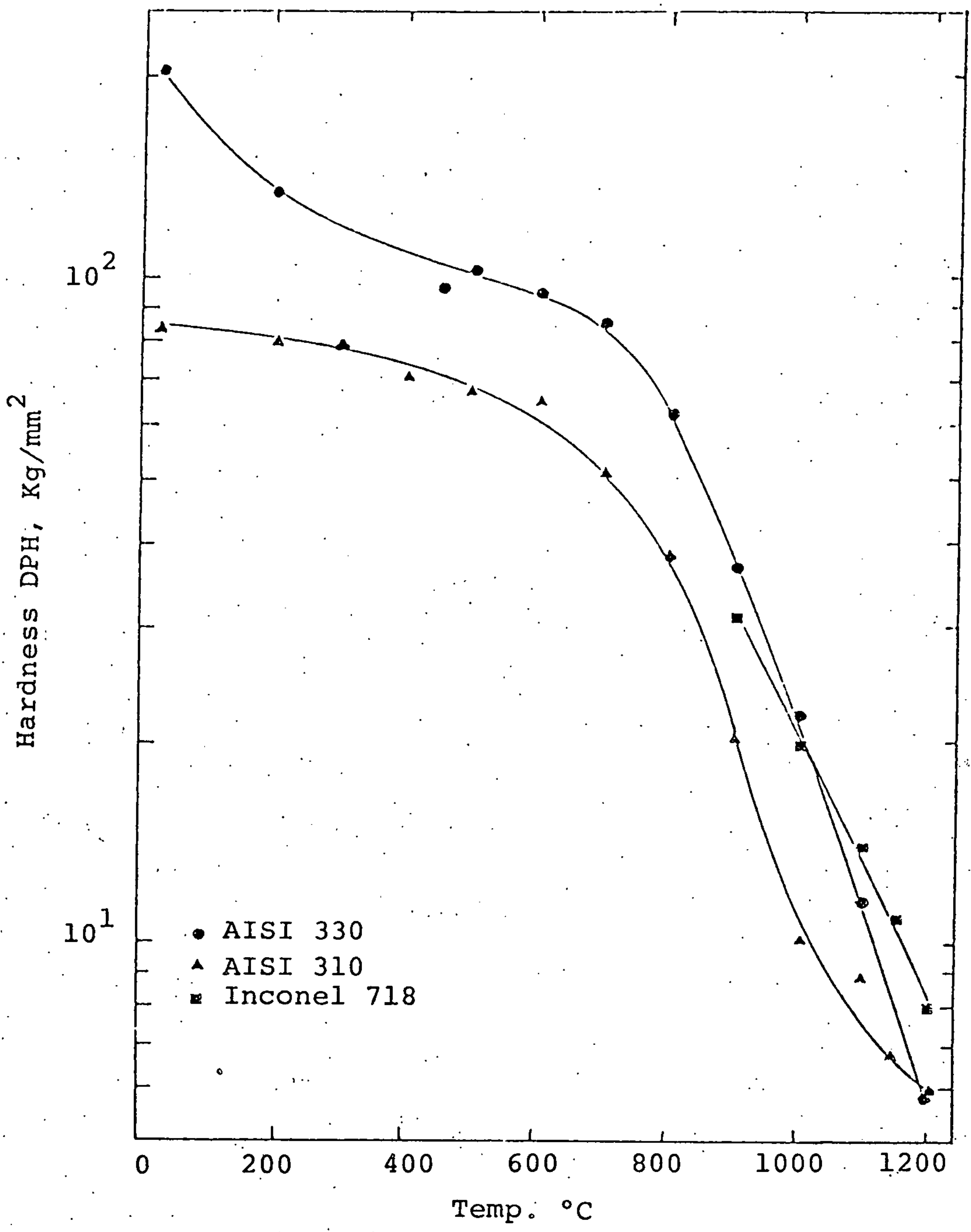

Fig. 7.1. Hardness versus Temperature for AISI 310 and Inconel 718 Compared to AISI 330.

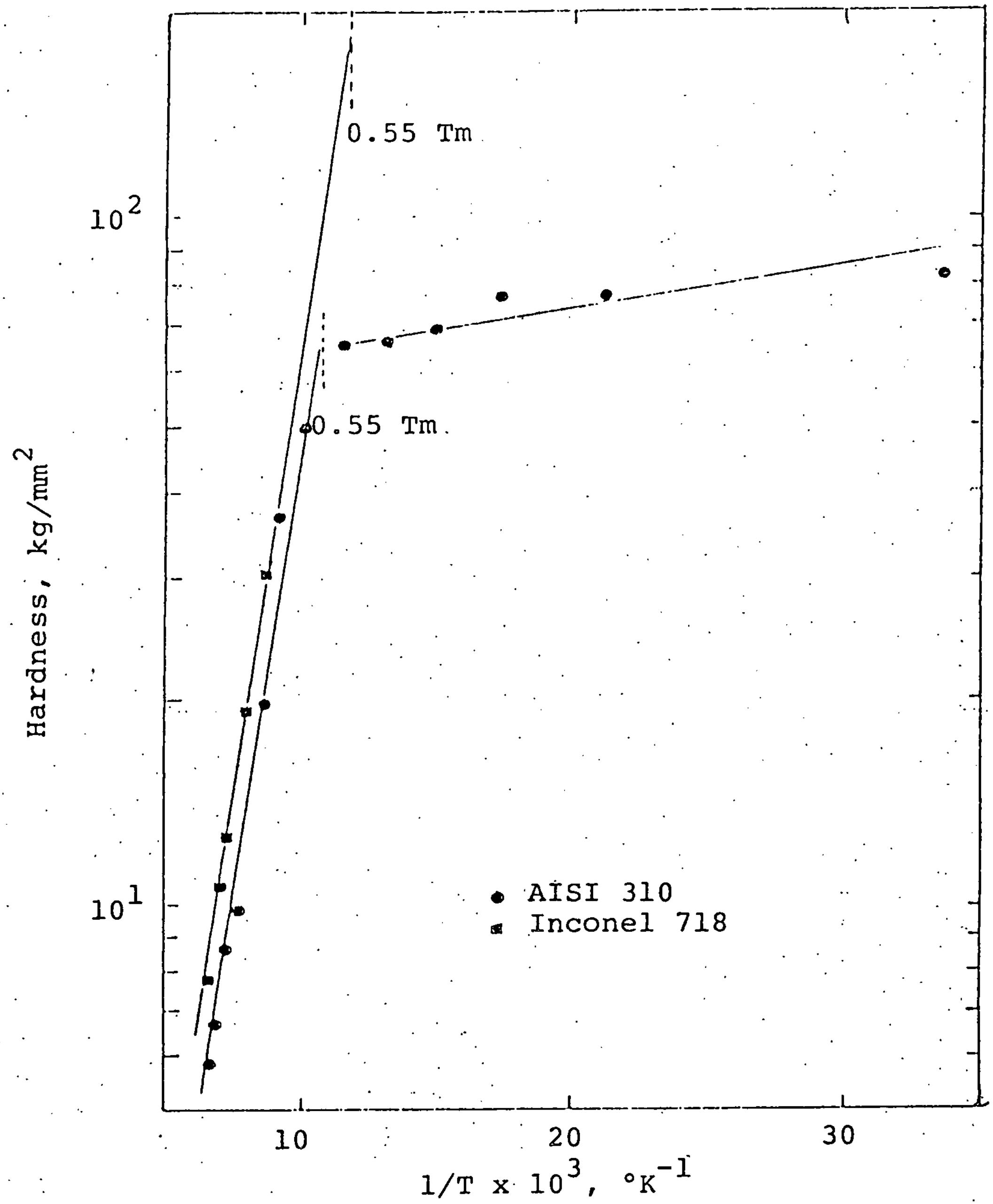

Fig. 7.2. Log Hardness versus 1/T for AISI 310 and Inconel 718.

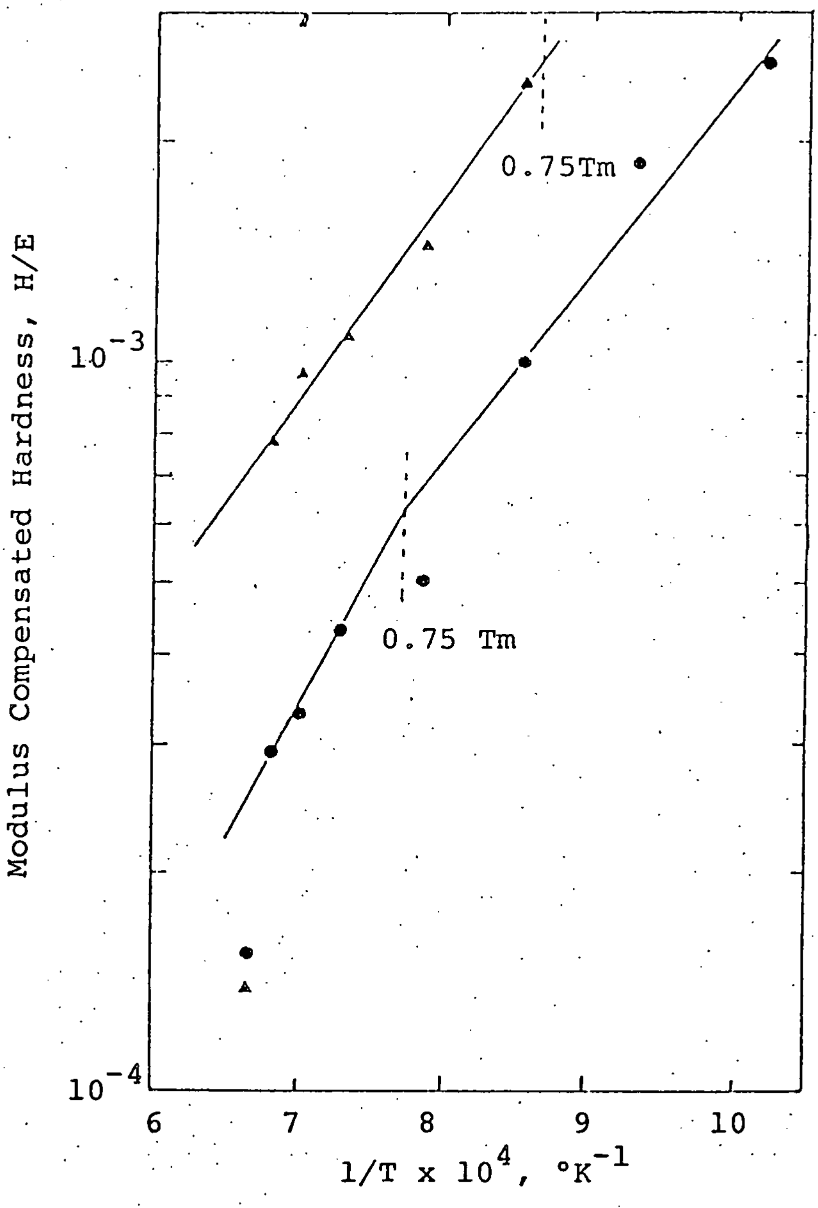

Fig. 7.3. Modulus Compensated Hardness versus 1/T for AISI 310 and Inconel 718.

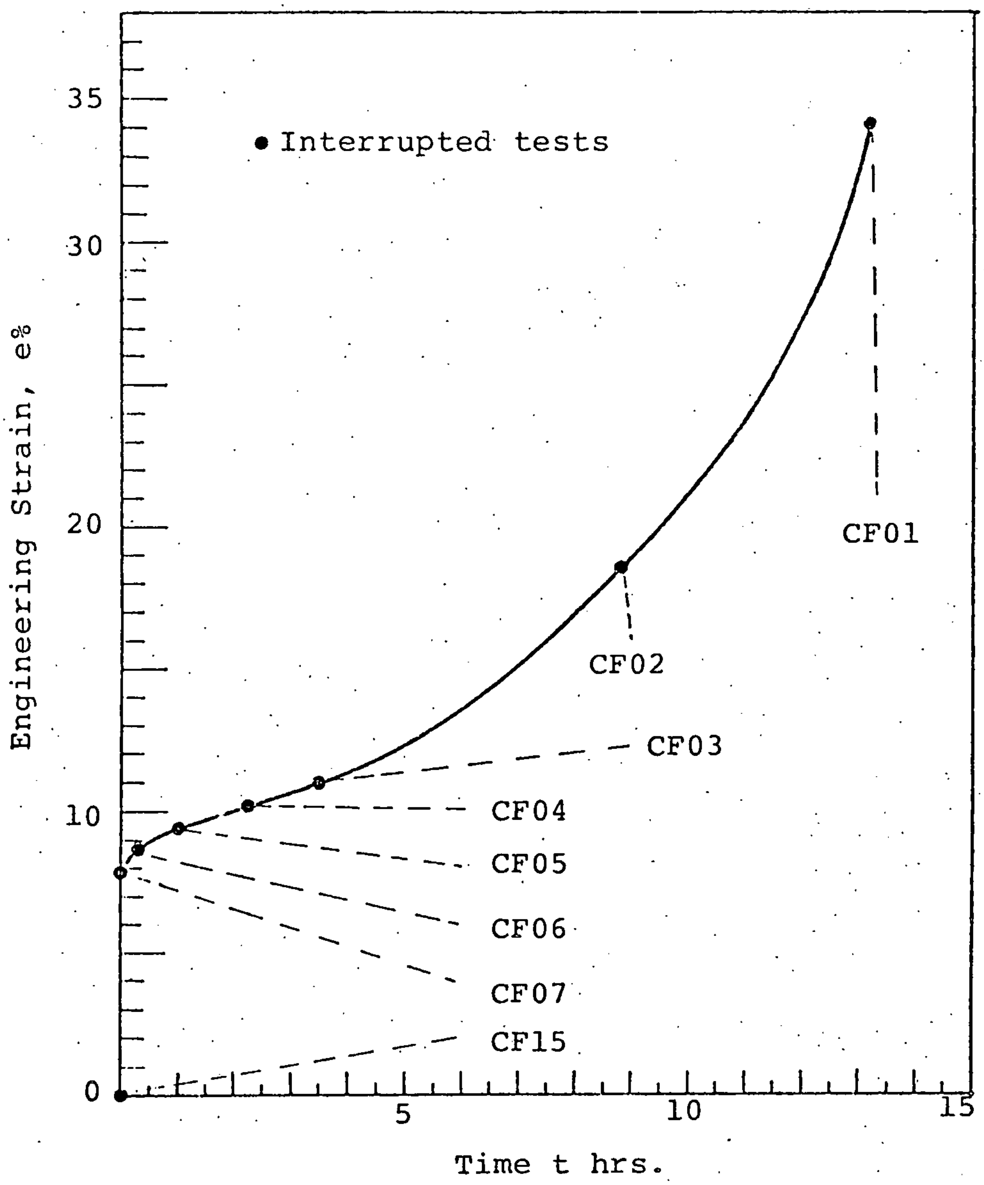

Fig. 7.4. Strain Behavior of AISI 330 Stainless Steel at 652°C and 35 ksi Applied Stress.

PUSH-PULL FATIGUE

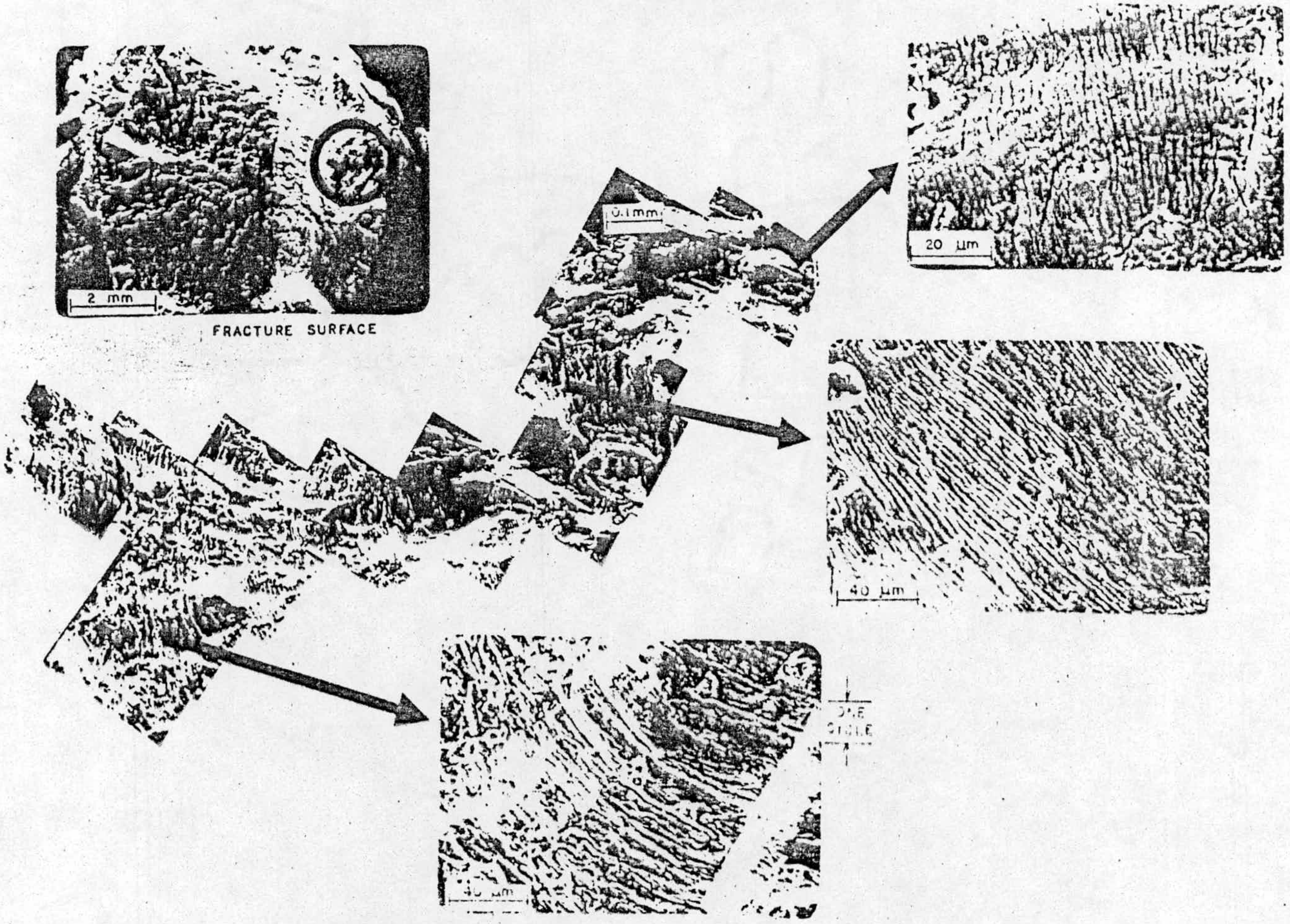

Fig. 7.5. AISI 304 SS Hour-Glass Specimen Montage of the Fractured Surface as Photographed by a Scanning Electron Microscope.

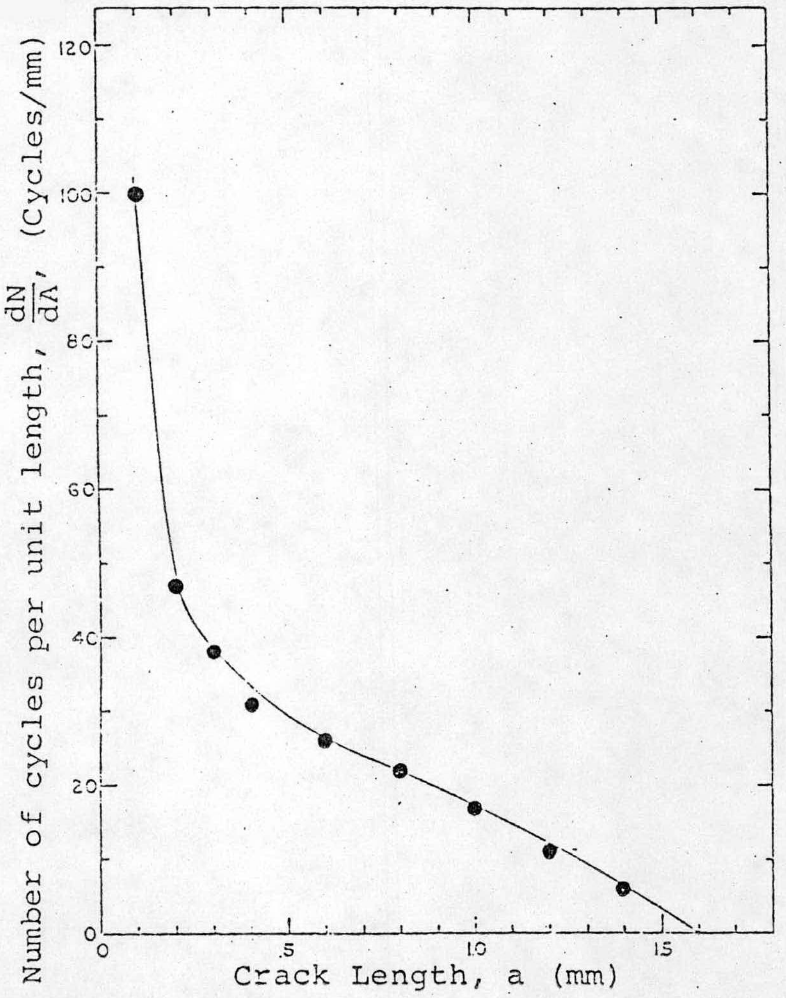

Fig. 7.6 a. Striation Density (dN/da) or the Number of Cycles per Unit Length Plotted Against Crack Length, a.

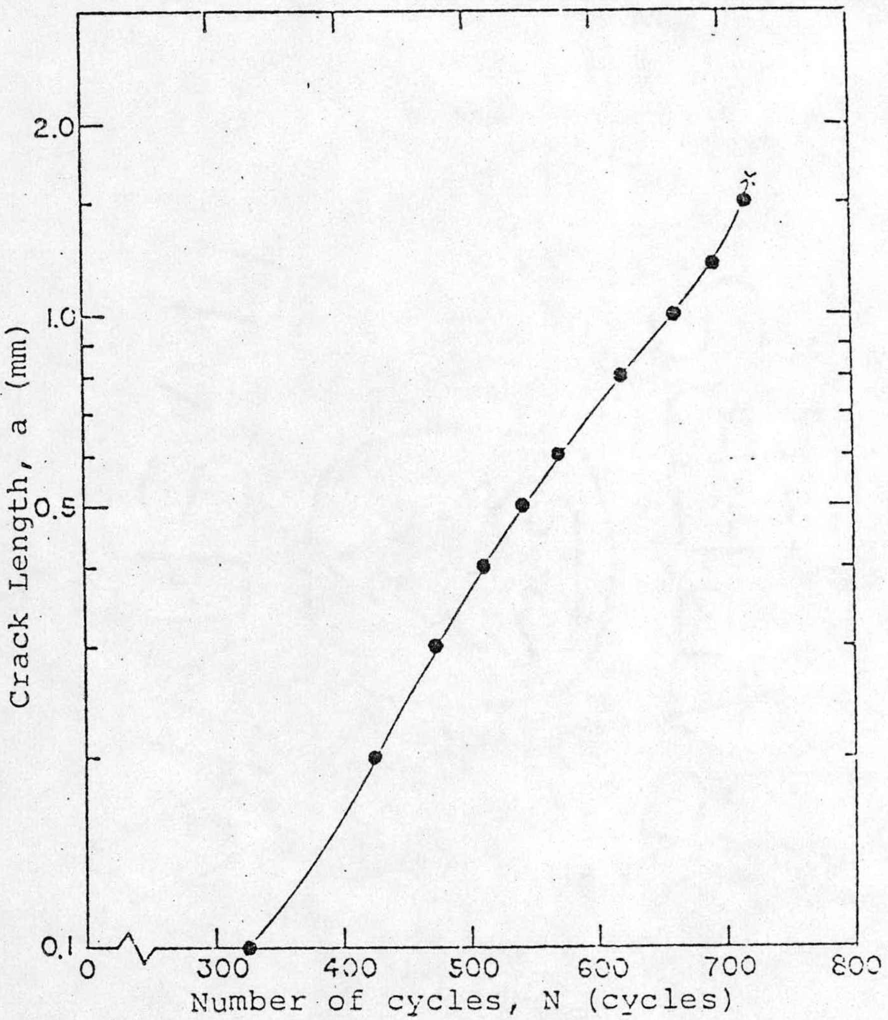

Fig. 7.6 b. ℓn a Versus N Plots of AISI 304 SS at 649°C in Air.

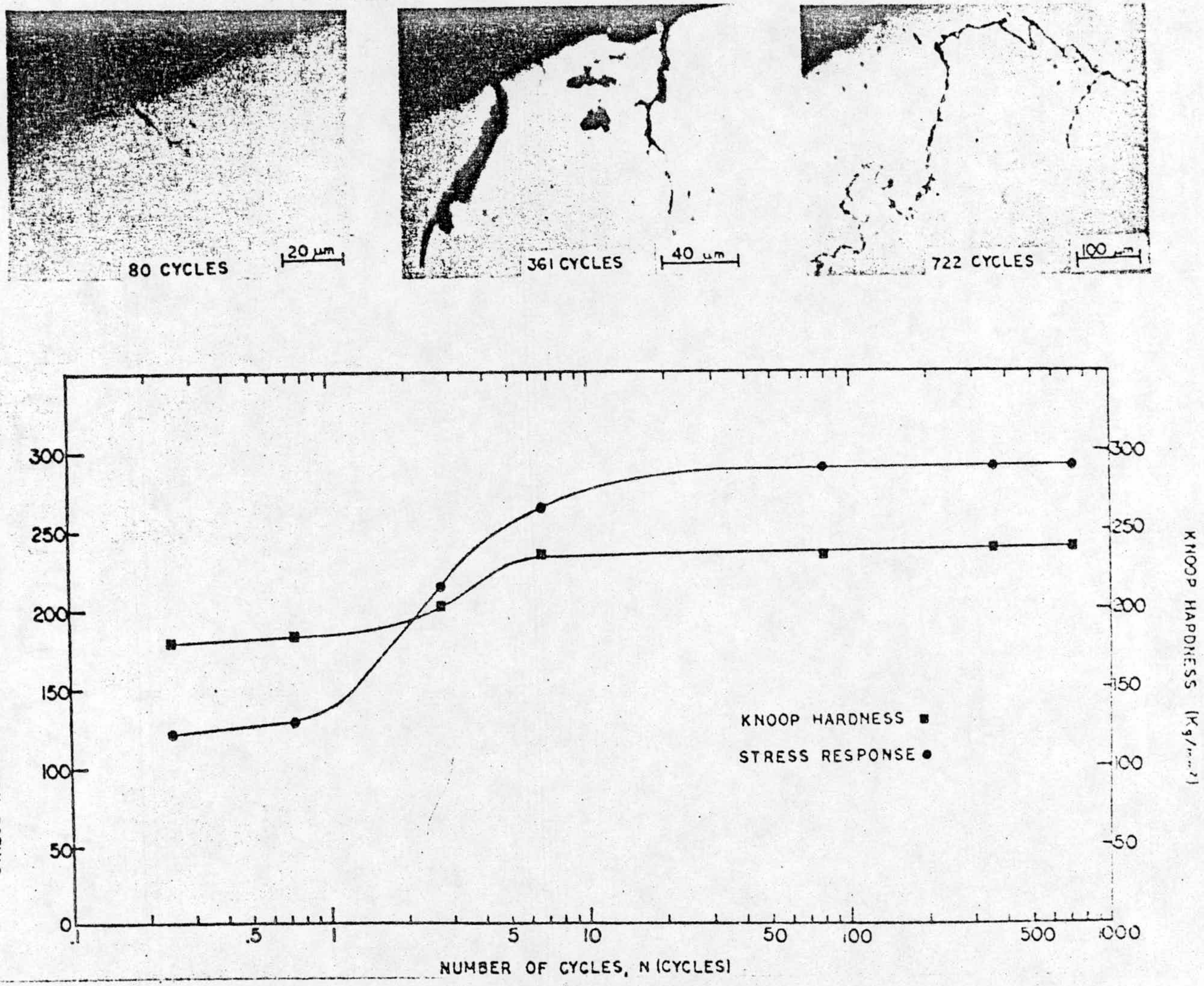

Fig. 7.7. Unetched Metallographic Specimens, Interrupted Before Failure, Showing the Development of a Crack During Crack Initiation and Propagation Periods. Plots Correlating Microhardness and Stress Response as a Function of N (Cycles).

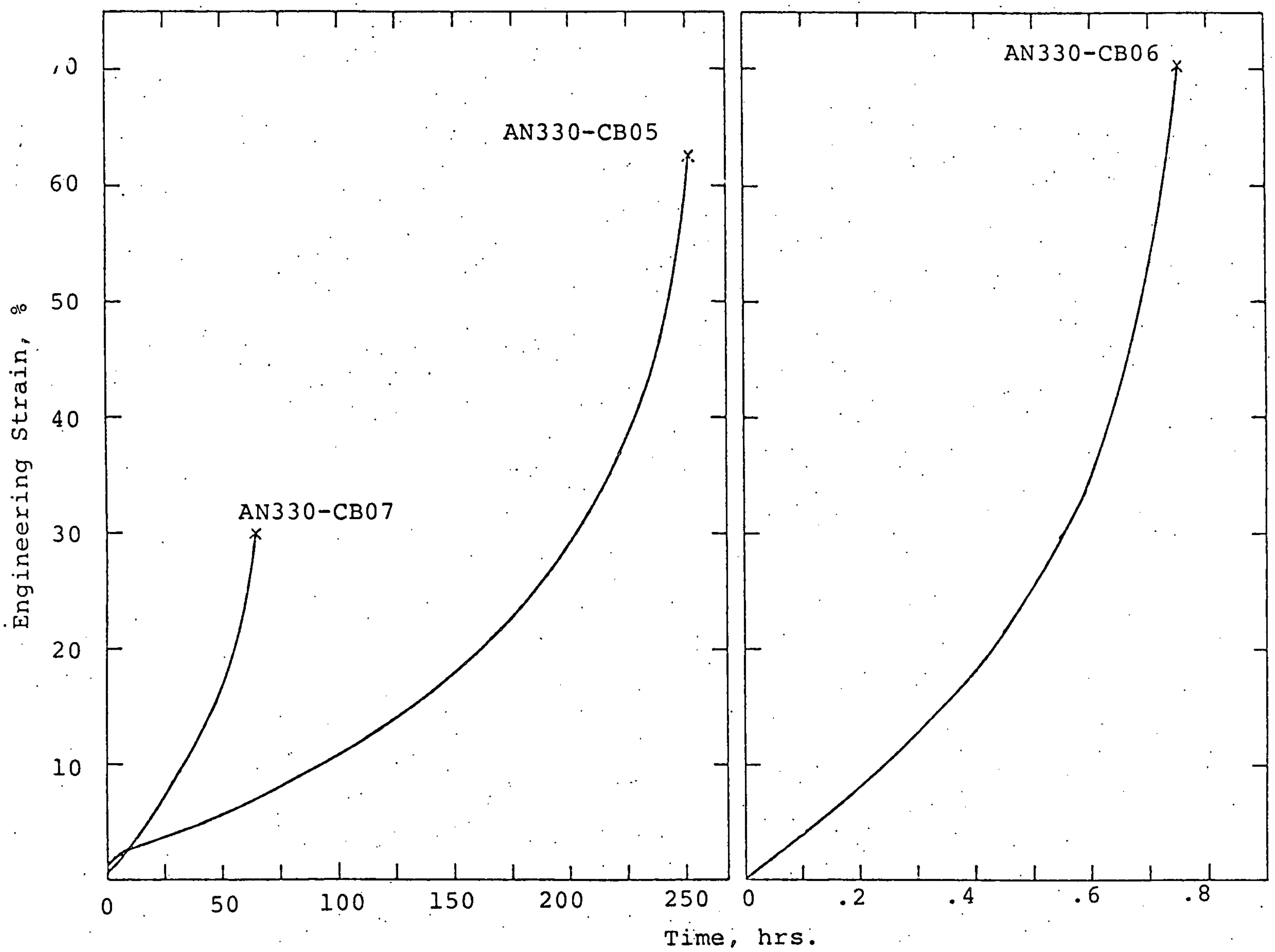

Fig. 7.8. Constant Load Creep-Rupture Curves for AISI 330 Stainless Steel Tested Various Conditions.

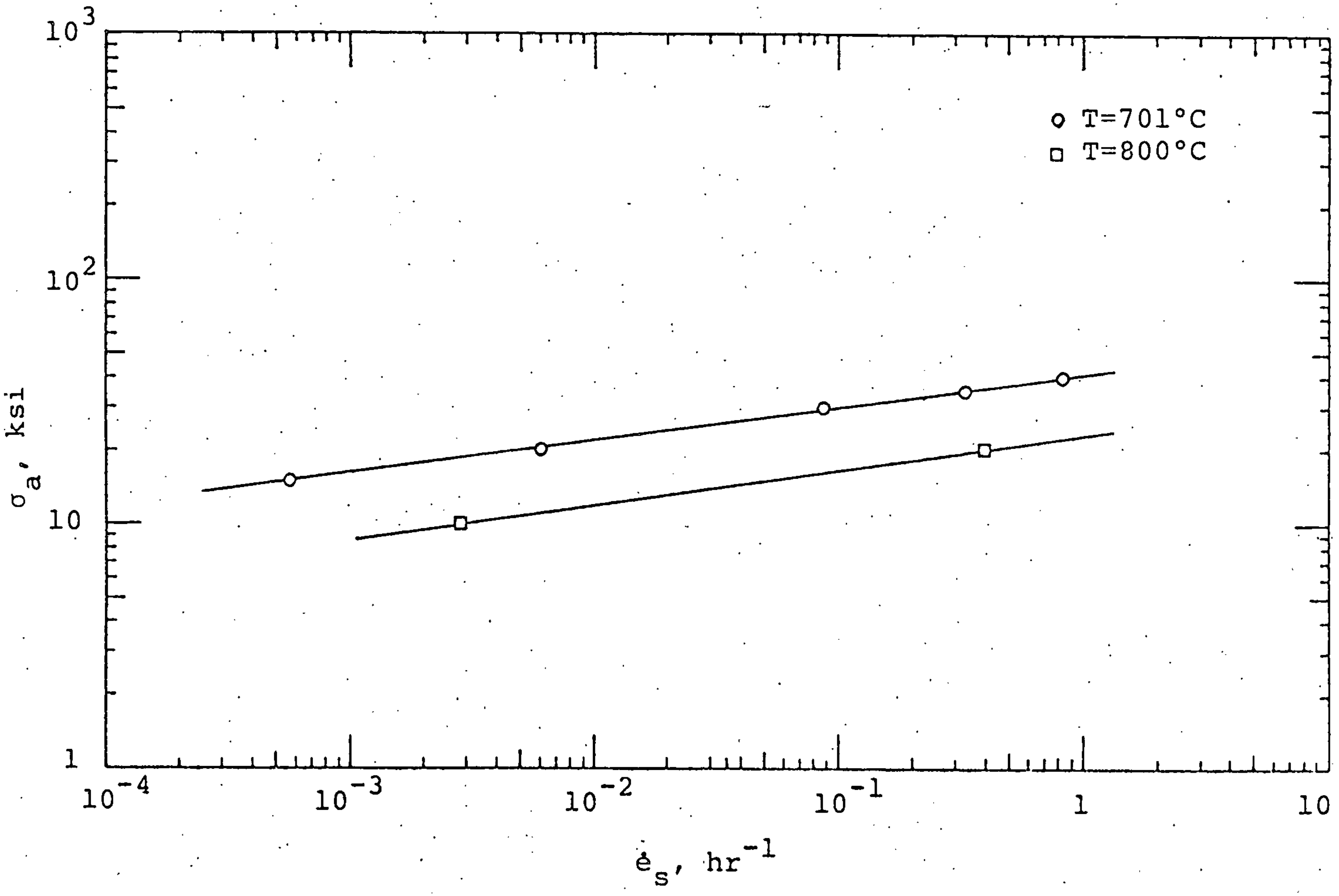

Fig. 7.9. Applied Stress, σ_a, versus Steady State Creep Rate, $\dot{e}_s$, for AISI 330 Stainless Steel Crept at Various Temperatures and Stresses.

APPENDIX E

PROGRESS REPORT FOR PERIOD ENDING JANUARY 31, 1977

7.1.1 INTRODUCTION

The objective of this program is to (a) evaluate the time, temperature and stress-dependent mechanical properties of reactor structural materials, (b) determine the relationship of these properties to the microstructure, (c) show the contribution of the microstructure to the internal stress fields and the subsequent influence on microcracking and the grain boundary sliding behavior during the normal plastic deformation at elevated temperatures and (d) demonstrate the relationship of the hot micro-hardness properties with the hot-tensile properties of a class of commercial and advanced alloys presently under investigation at other laboratories. Special consideration is being given to operating conditions typical of nuclear reactor applications, including the knowledge that radiation environment can influence the substructure of these metals, a circumstance which can lead to significant changes in the conventional mechanical property behavior.

7.1.2 EXPERIMENTAL PROGRAM

Transmission electron microscopy has been used as the primary tool to study the deformation substructure of reactor structural materials resulting from creep, fatigue and tensile testing at elevated temperatures. Complementary work using optical microscopy, scanning electron microscopy and hot-hardness testing has been performed to characterize the deformation and failure behavior. New work is underway to perform similar studies on the Commercial, the Developmental and the Fundamental alloys being evaluated in the National Alloy Developmental Program with particular attention on the application of hot-hardness measurement as a strength microprobe.

7.1.2.1 A Study on Subgrain/Cell Development During Creep Deformation (J. Foulds)

Mechanical testing: Several creep tests were run to rupture at 652°C and an applied stress of 25 ksi. A more careful and accurate measurement of specimen diameters resulted in better reproducibility than reported previously. The minimum diameter within a half inch about the center of the gage section was used in calculation of the load. Fig. 7.1 shows the creep curve and Table 7.I the raw test data for the same. The interrupted test data will be reported on completion of the tests.

Transverse sections were taken from each of the Specimens AN330-CF01 through AN330-CF07(1) and studied optically. The sections were cut adjacent to the ones being utilized for substructure development studies. Optical microscopy on these indicated no discernible variation in average grain size with a considerably non-uniform distribution (with regard to size) of equiaxed

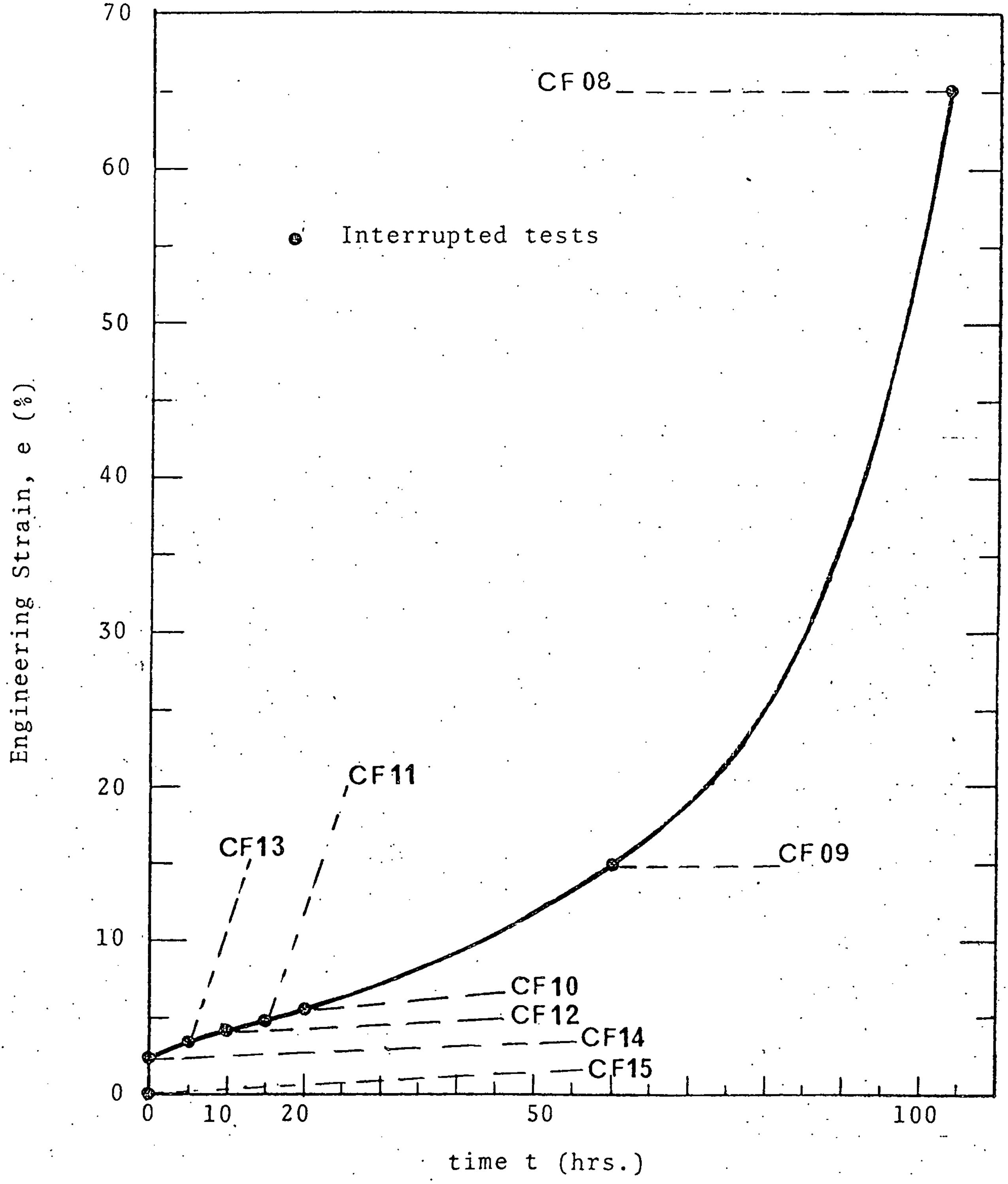

Fig. 7.1 Strain behavior of AISI 330 stainless steel at 652°C and 25 ksi applied stress.

TABLE 7.I RUPTURE DATA AT 652°C AND 25 ksi APPLIED STRESS

Sample Number	e_p %	e_t %	$\dot{e}_s$ %/hr.	t_2 hr.	e_R %	RA %	t_R hr.
N330-CF08	2.20	4.2	0.1392	20.0	65.0	66.5	103.7

e_p = plastic loading strain

e_t = cumulative strain at end of primary creep

$\dot{e}_s$ = minimum secondary creep rate

t_2 = time to reach the end of secondary creep

t_R = time to rupture

e_r = rupture strain

RA = reduction in cross-sectional area

NOTE: All values are obtained through graphical methods.

grains as observed in the as-annealed untested condition.

Cracking and Fracture: Fig. 7.2 shows a stereo pair of SEM fractographs of the specimen tested at 652°C and 35 ksi. These show a highly dimpled structure as a largely transgranular type of cracking mechanism. However, as seen in Figures 7.3 and 7.4 which are optical micrographs from a transverse section of the same specimen, there exists some intergranular cracking indicated by the formation of W-type (wedge) or triple point cracks (Fig. 7.3) and r-type cavities (Fig. 7.4) at the grain boundaries. A larger than expected concentration of W-type cracks were observed and since the rupture strain (34%) suggested a "reduction in ductility" or "embrittlement" (rupture strain = 65% for test at 652°C and 25 ksi), it appears to have been caused by the initiation of these intergranular cracks. Mainly responsible for this is an inhibited grain boundary migration. As early as 1960 grain boundary migration was found to be restricted by the presence of small closely-spaced carbide particles in some austenitic stainless steels.(2,3) Precipitates in this case have been observed along grain boundaries but have not been identified.

Thus, longer test times (as at 652°C and 25 ksi) would result in sufficient agglomeration of the second grain boundary phase to permit grain boundary migration.

icroscopy on the Specimen AN330-CF08 will confirm or rule

TABLE 7.II TENSILE PROPERTIES OF IN-718[(a)]

Temp. T,(°C)	Hardness DPH,(kg/mm^2)	Reciprocal Temp. T^{-1}(°K^{-1})	Youngs' Modulus, E(kg/mm^2)[b]	Strain Hardening Exponent, n	ULTIMATE TENSILE STRENGTH σ_u^{cal}(kg/mm^2)	ULTIMATE TENSILE STRENGTH σ_u^{exp}(kg/mm^2)[c]
20	410	3.37×10^{-3}	2.02×10^{-4}	0.164	135	135
200	371	2.11	1.94	0.146	121	
232						129
300	370	1.75	1.89	0.145	120	
315						119
400	362	1.49	1.83	0.139	117	
427						116
500	351	1.29	1.77	0.131	113	
538						113
600	338	1.15	1.70	0.117	108	
649						96.9
700	307	1.03	1.62	0.044	98.6	
760						63.9
800	224	0.93	1.53	0.022	73.5	-
900	61.0	0.85	1.43	0.007	20.5	-
1000	35.7	0.79	1.38	-	-	-

(a) Heat treatment: 955°C/1 hr./WQ + 720°C/8 hr./FC to 620°C/hold 18 hrs. total furnace time.

(b) From Reference 13.

(c) From Reference 12.

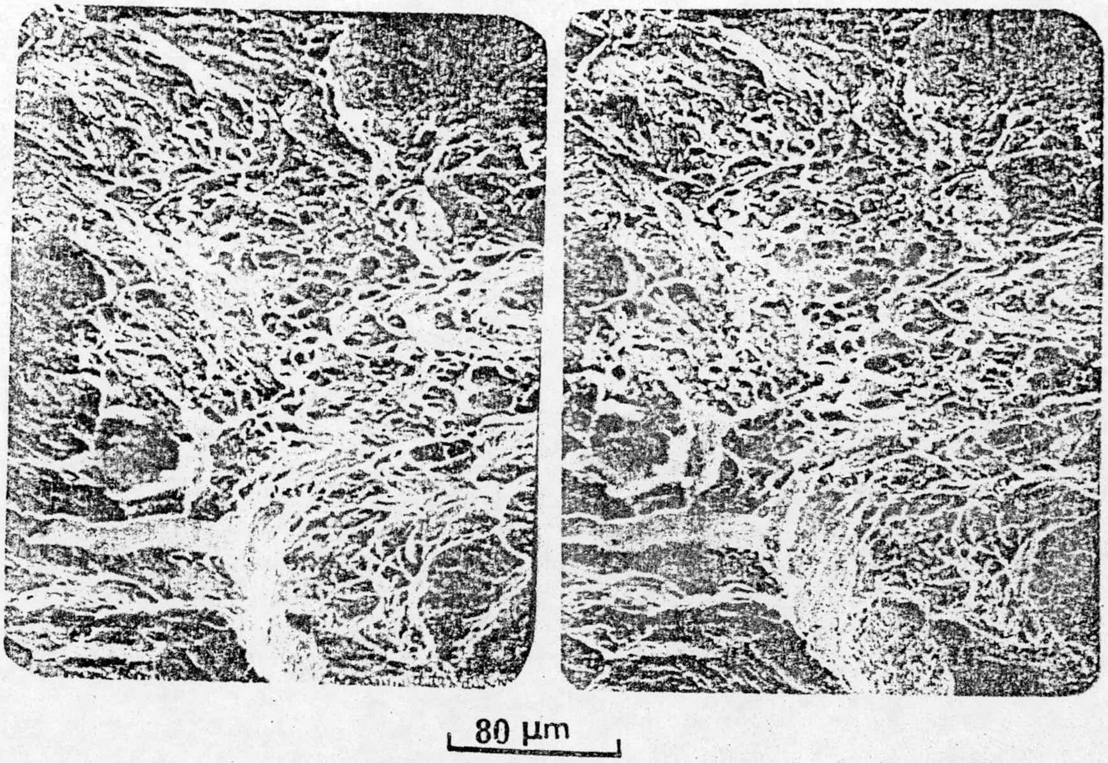

Fig. 7.2 SEM fractographic stero pair of AISI 330 SS specimen tested at 652°C and 35 ksi.

Fig. 7.3 Wedge crack in section from specimen AN330-CF01

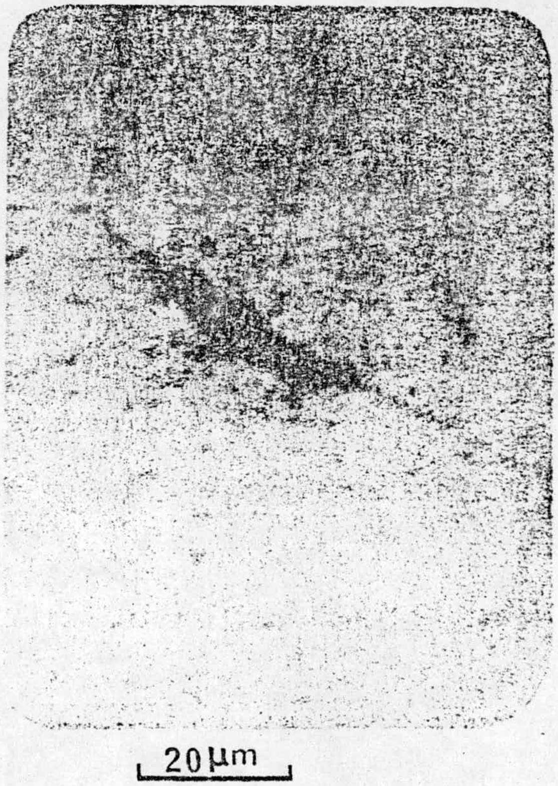

Fig. 7.4 R-type cavity in section from specimen AN330-CF01

out this possibility. This, however, still does not explain the large amount of transgranular cracking, which could only occur if grain boundary crack-propagation were arrested and the only available crack growth directions were transgranular through a "weaker" matrix during the tertiary creep stage. This investigation will continue.

Room temperature microhardness: Room temperature microhardness (DPH) measurements were made on longitudinal sections from Billings' ruptured Specimens AN330-CB01, -CB02, - CB04, - CB05. All these are ruptured specimens tested at 701°C and different applied stresses.(4) Fig. 7.5 shows the results obtained.

As expected for necking under constant load, the hardness values in each case decreased to a constant as a function of distance from the fracture surface indicating a greater degree of strain-hardening nearer the surface. It should be noted that 0.0 mm from the fracture surface corresponds to the nearest position at which measurements were possible. At least 6 measurements were made at each position along the length using a 500 g. load.

The curves obtained exhibit a certain "parallelism" indicating similar strain-hardening variations as a function of distance from the fracture surface in each case. The strain-hardening "profile" at 20 ksi shows 2 plateaus apparently due to more than one locally-necked region. Crack density measurements on this specimen will

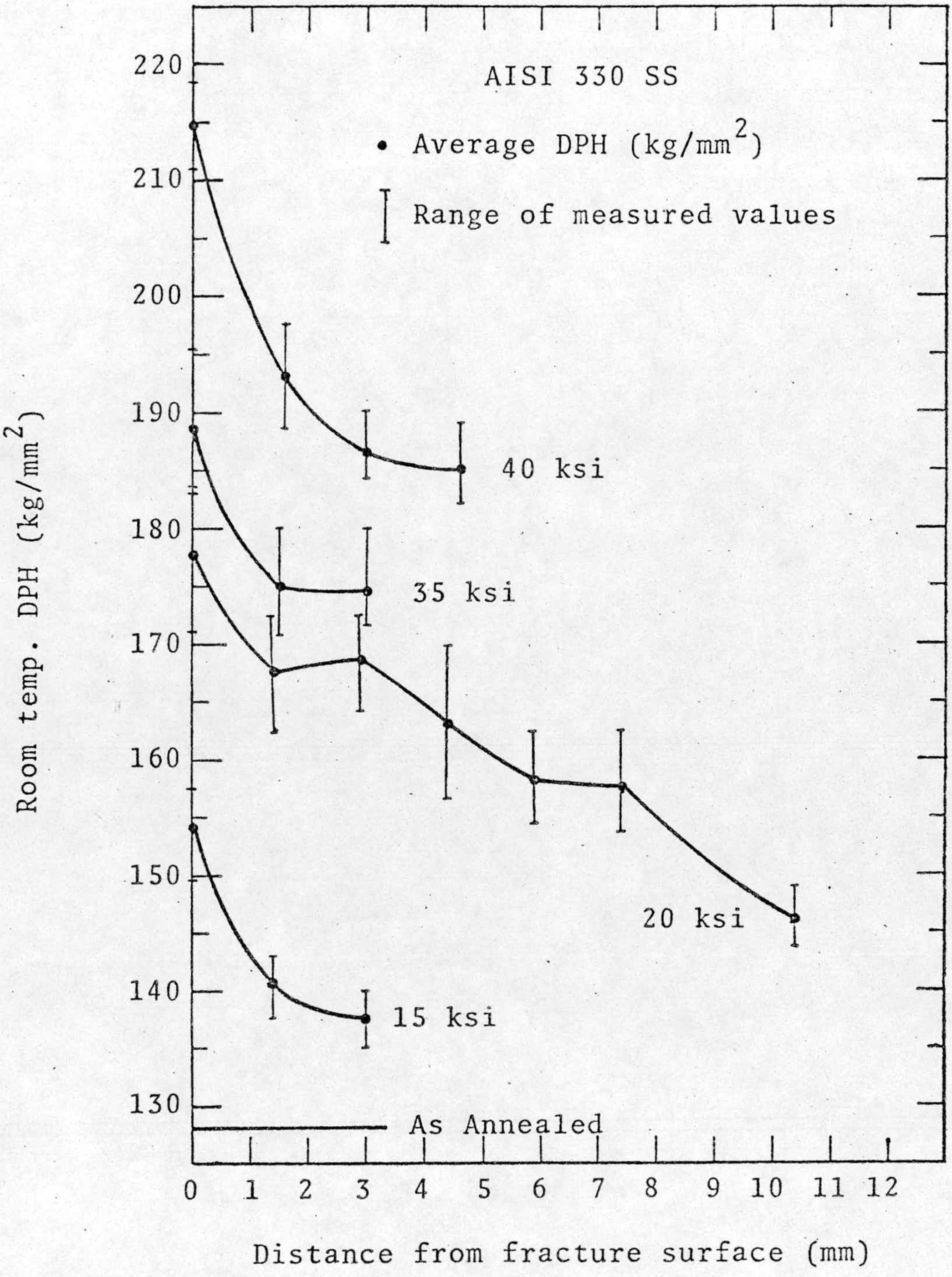

Fig. 7.5 Room temperature microhardness as a function of distance from the fracture surface for various applied stresses at 701°C.

throw more light on the subject from a 'fracture mechanics' standpoint.

Knowing that the driving force for strain hardening is an effective stress $\sigma_a - \sigma_i$ where σ_a = the applied stress and σ_i = the internal stress one does expect the observed increase in microhardness with an increasing applied stress. The disproportionate differences in DPH, however, are due to the differing extents of recovery in each case. Since the driving force for recovery is σ_i and since recovery processes predominate in the tertiary stage of creep, a variety of reasons may be presented for this effect.

Transmission Electron Microscopy: Transverse sections from the "as-annealed" material and the two ruptured specimens (AN330-CF01 and - CF08) were briefly looked at under the transmission electron microscope. Subgrains were observed in the specimen ruptured at 25 ksi and cells in the one tested at 35 ksi.

Fig. 7.6 shows a few representative micrographs. All the specimens exhibit at least one second phase yet to be identified. Fig. 7.6d shows dislocation tangles with a second phase, and Fig. 7.6a a considerable amount of precipitate associated with subgrain boundaries.

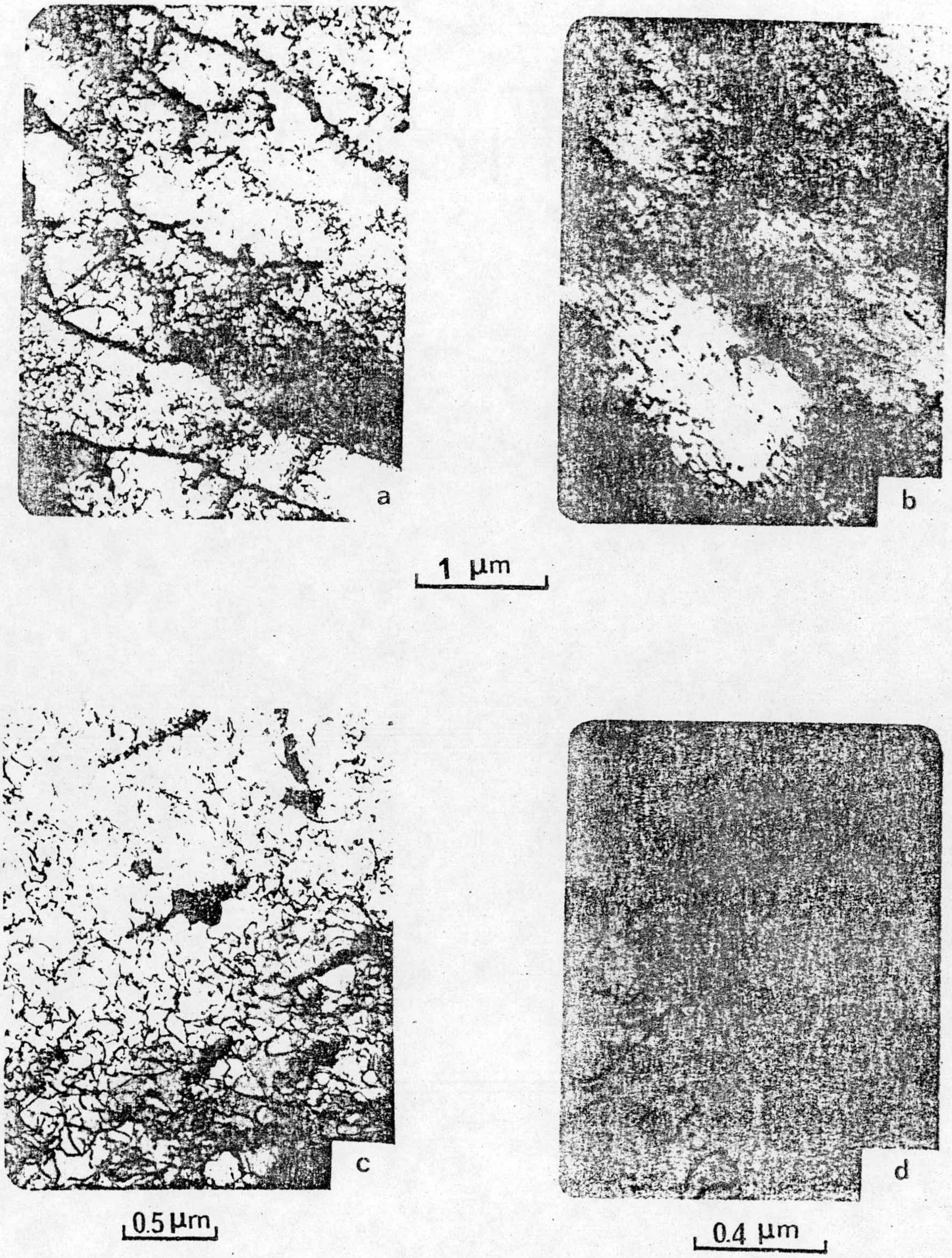

Fig. 7.6 Micrographs of AISI 330 SS specimens tested at: (a) and (c) 652°C and 25 ksi; (b) 652°C and 35 ksi; (d) "as-annealed" condition.

7.1.2.2 Stress-Temperature Effects on Substructure

(R. Billings)

No new creep rupture data is available at this time due to the long term nature of the tests presently in progress. Data on the two tests presently in progress are as follows:

Sample Number	Test Temperature, °C	Applied Stress, MPa
AN330-CB08	600	137.9
AN330-CB09	500	413.8

Strain on Loading, %	Accumulated Strain to Date, %	Test Time to Date, hrs.
1.10	2.10	2754
17.39	18.09	755

In addition to the above data, a value of $1.35 \times 10^{-6}\ \text{hr}^{-1}$ has graphically been determined for the minimum steady state creep rate of sample AN330-CB08. It appears that this sample has progressed into the tertiary region. Assuming this to be the case, the test will soon be halted due to the limited time available for this study. It has been reported in the literature that the deformation substructure in austenitic stainless steels; e.g., 304 and 316, is well developed by the end of secondary creep and essentially remains constant through the tertiary region until rupture.(5,6) Assuming this observation to also hold true for A.I.S.I. 330 Stainless Steel, it is felt that the pre-rupture termination of the AN330-CB08 test will not detrimentally affect the substructure study.

The value of the steady state creep rate has been used to modify the previously reported(7) value of the apparent activation energy for creep, ΔH_c. After Garofalo,(8) if it can be assumed that the substructure developed in the steady state creep of a material is a function of stress, independent of temperature, then the steady state creep rate is given by the equation:

$$Z = \overset{\circ}{e}_s \ \exp\,(\Delta H_c/RT) \qquad (7.1)$$

where

Z = Zener-Holloman parameter, h^{-1}

$\dot{e}_s$ = the secondary creep rate, h^{-1}

ΔH_c = apparent activation energy for creep, Kcal/mole

RT = its usual meaning.

Z, which is a function of the applied stress, takes on a constant value during steady state creep. Hence, a plot of $\ln \dot{e}_s$ versus $1/T$ should yield a straight line of slope equal to $-\Delta H_c/R$ and intercept equal to $\ln Z$. For the same material, tested over a constant temperature range, such a plot should yield parallel lines for each set of samples tested at different applied stresses. Such a plot has previously been reported for A.I.S.I. 330 Stainless Steel tested at σ_{app} = 137.9 MPa. The value for

ΔH_c calculated from this plot was ΔH_c = 100 Kcal/mole. In light of the newly determined value of $\dot{e}_s$ for sample AN330-CB08, the proper value for ΔH_c in the 600°C to 800°C temperature interval is 118 Kcal/mole. The modified ln $\dot{e}_s$ vs. 1/T plot will not be shown.

It should be noted that on 11-26-76 the University suffered a major power breakdown lasting approximately for twenty minutes. As a result, the temperature in the furnace of the AN330-CB08 test fell 50°C. The 600°C temperature was regained approximately 30 minutes after the breakdown occurred. Hence, the test of sample AN330-CB08 doesn't meet A.S.T.M. standards for creep rupture testing. However, contrary to the expected effects of the breakdown, after a short incubation period at 600°C, the measured strain values did not differ significantly from those obtained before the breakdown. In other words, the strain rates before and after the breakdown were consistent. However, the substructure, no doubt, was affected by the temperature change. The microscopy of sample AN330-CB08 will be reported later.

Optical microscopy and Transmission Electron microscopy (T.E.M.) are being performed on the ruptured specimens.

7.1.2.3 Hot-Hardness of IN-718, 706, PE-16, M-813 and Correlation with Ultimate Tensile Strength of IN-718 and PE-16 (F. Price)

Hot-hardness tests were conducted on the above alloys using a Diamond Pyramid Indentor with sapphire tip in a high purity argon atmosphere. Results are listed in Tables 7.II through 7.IV and in Figures 7.7 and 7.8.

Sample preparation involved mechanical polishing followed by electro polishing to remove any cold worked layer induced by the mechanical polish or sample cutting.

The following specimens are from Hanford Engineering Development Laboratories and include their chemical analysis (see Table V): IN-718, PE-16, M-813. The IN-706 specimen was acquired from other sources and the heat number and exact chemical composition are not known.

Apparent activation energies for indentation hardness were calculated for all specimens from the Larsen-Badse relation.(9)

$$H = Ae^{2Q^1/RT} \qquad (7.2)$$

Results are as follows:

IN-718	$T < .55\ T_m$,	$Q^1 = 100$ cal/mole
	$T > .55\ T_m$,	$Q^1 = 13.6$ Kcal/mole
IN-706	$T < .55\ T_m$,	$Q^1 = 110$ cal/mole
	$T > .55\ T_m$,	$Q^1 = 8.7$ Kcal/mole
PE-16	$T < .55\ T_m$,	$Q^1 = 70$ cal/mole
	$T > .55\ T_m$,	$Q^1 = 10$ Kcal/mole

TABLE 7.III TENSILE PROPERTIES OF PE-16$^{(a)}$

Temp. T,(°C)	Hardness DPH,(kg/mm^2)	Reciprocal Temp. T^{-1},(°K^{-1})	Strain Hardening Exponent, n	ULTIMATE TENSILE STRENGTH	
				σ_u^{cal},(kg/mm^2)	σ_u^{exp}(kg/mm^2)^b
20	263	3.37 x 10^{-3}	0.212	90.3	106
200	238	2.11	0.217	82.2	
316					96.6
350	235	1.61	0.204	80.5	
427					92.8
500	229	1.29	0.184	76.5	
538					89.5
600	230	1.15	0.141	74.7	
649					76.1
700	215	103	0.049	69.0	-
800	127	0.93	0.022	41.5	-
900	40.2	0.85	-	-	-
1000	20.7	0.79	-	-	-
1100	12.3	0.73	-	-	-

(a) Heat treatment: 1080°C/4 hrs./AC + 900°C/1 hr./AC + 750°C/8 hrs./AC.

(b) From Reference 12.

TABLE 7.IV HOT-HARDNESS OF IN-706 AND M-813

IN-706 (a)		M-813 (b)	
Temp. T, (°C)	Hardness DPH, (kg/mm^2)	Temp. T, (°C)	Hardness DPH, (kg/mm^2)
20	392	20	401
204	369	200	377
427	341	350	376
537	332	500	343
649	290	600	317
732	223	700	239
816	114	800	133
		900	36.9
		1000	18.4

(a) Heat treatment: 955°C/1 hr./WQ + 843°C/3 hrs./AC + 720°C/8 hrs./FC to 620°C/16 hrs./AC.

(b) Heat treatment: 1080°C/4 hrs./AC + 900°C/1 hr./AC + 720°C/8 hrs./AC.

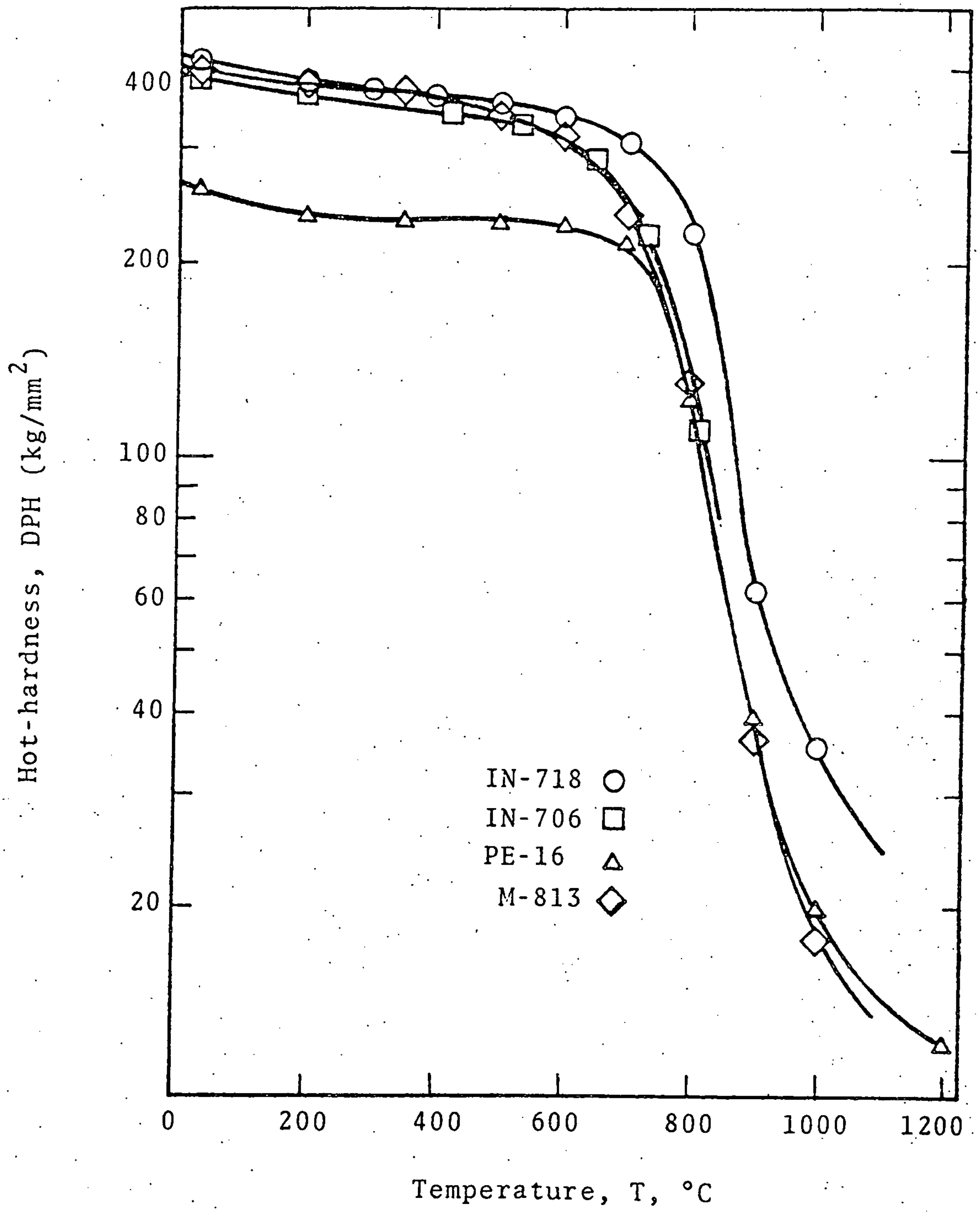

Fig. 7.7 Hot-hardness of several engineering alloys as a function of test temperature.

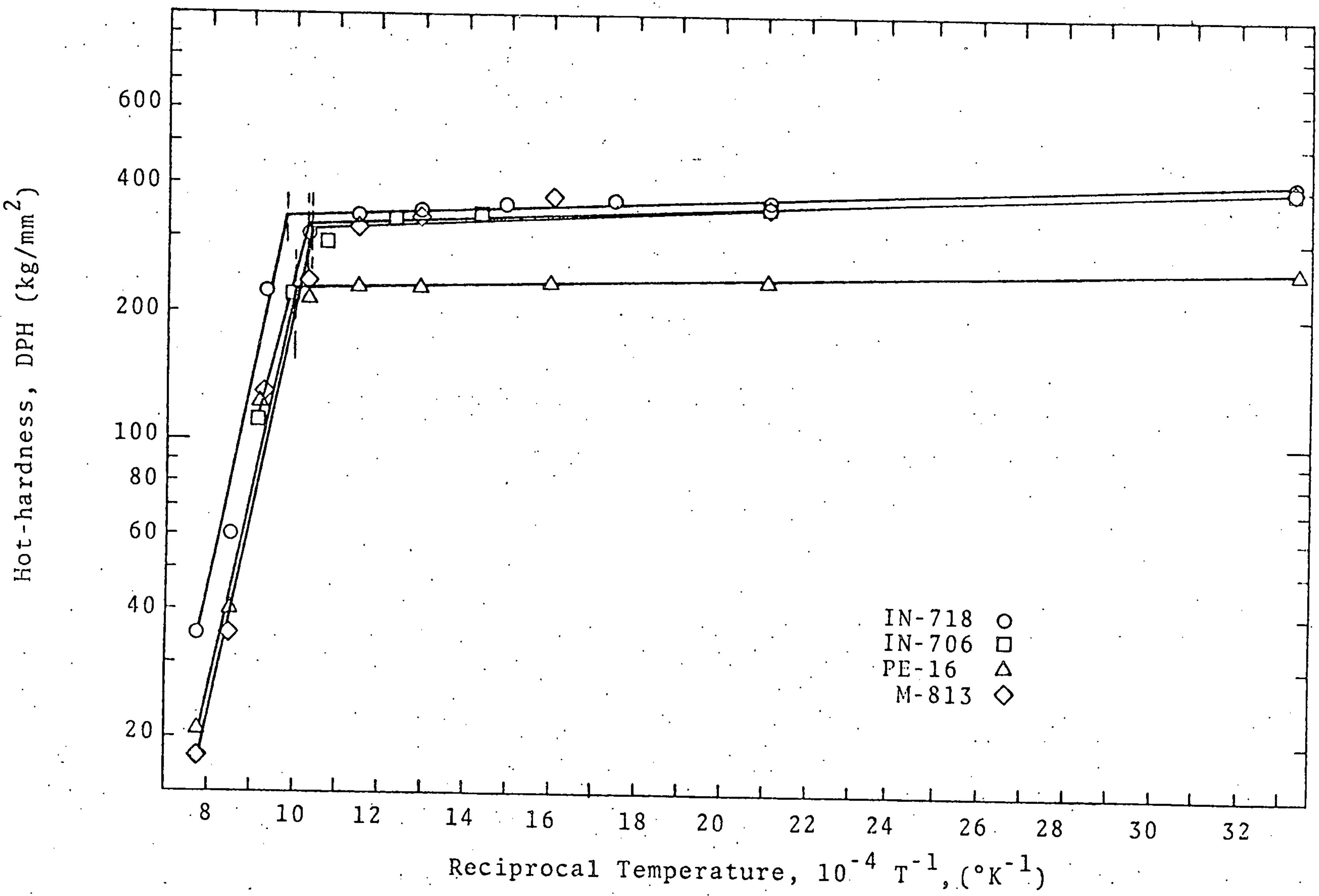

Fig. 7.8 Hot-hardness of several engineering alloys as a function of reciprocal absolute temperature.

TABLE 7.V CHEMICAL COMPOSITION OF TESTED ALLOYS
Content, Wt%

Alloy	(Heat)	C	Mn	Si	Cr	Mo	Ni	Nb	V	Ti	Ta&Nb
PE-16	(C07206)	.082	<.01	<.01	16.5	3.15	43.37	-	<.01	1.27	-
M-813	(R74073)	.041	-	-	18.64	4.21	34.50	-	-	2.45	-
IN-718	(59F1EY)	.041	.095	.41	18.50	3.54	54.30	-	-	.87	5.68

Alloy	(Heat)	B	O	Zr	S	Al	P	Sn	N	Cu	Co
PE-16	(C07206)	.0032	-	<.01	.001	1.20	.001	<.001	.002	<.01	.03
M-813	(R74073)	.011	.072	.020	-	1.42	-	-	-	-	.04
IN-718	(59F1EY)	-	-	-	-	.65	-	-	.0094	1.25	.036

M-813 $T < .55\ T_m$, $Q^1 = 90$ cal/mole

$T > .55\ T_m$, $Q^1 = 11$ Kcal/mole

The apparent activation energies for $T > .55\ T_m$ range from about 1/10 to 1/20 of the activation energies for creep or lattice self-diffusion. This may be explained as provided for by Sherby and Armstrong.(10)

They propose the expression:

$$H/_E = G\ e^{\frac{Q_L}{nRT}} \qquad (7.3)$$

Where H is the Diamond Pyramid Hardness, E is the temperature dependent elastic modulus, G is a constant, n is a number equal to 5, R is the gas constant, T is temp in degrees Kelvin, and, Q_L is the activation energy.

For IN-718:

$$Q_L = 119 \text{ Kcal/mole for } T > .55\ T_m.$$

No inflection was found in the log (H/E) versus 1/T plot (see Fig. 7.9) except at $.55\ T_m$. This is supported by earlier hot-hardness of IN-718. This leads to one of two possible conclusions:

1) The inflect was not visible in present data due to an insufficient number of data points around $.75\ T_m$; or,
2) The transition between rate controlling mechanisms in this material is sufficiently gradual so that it is not readily observable.

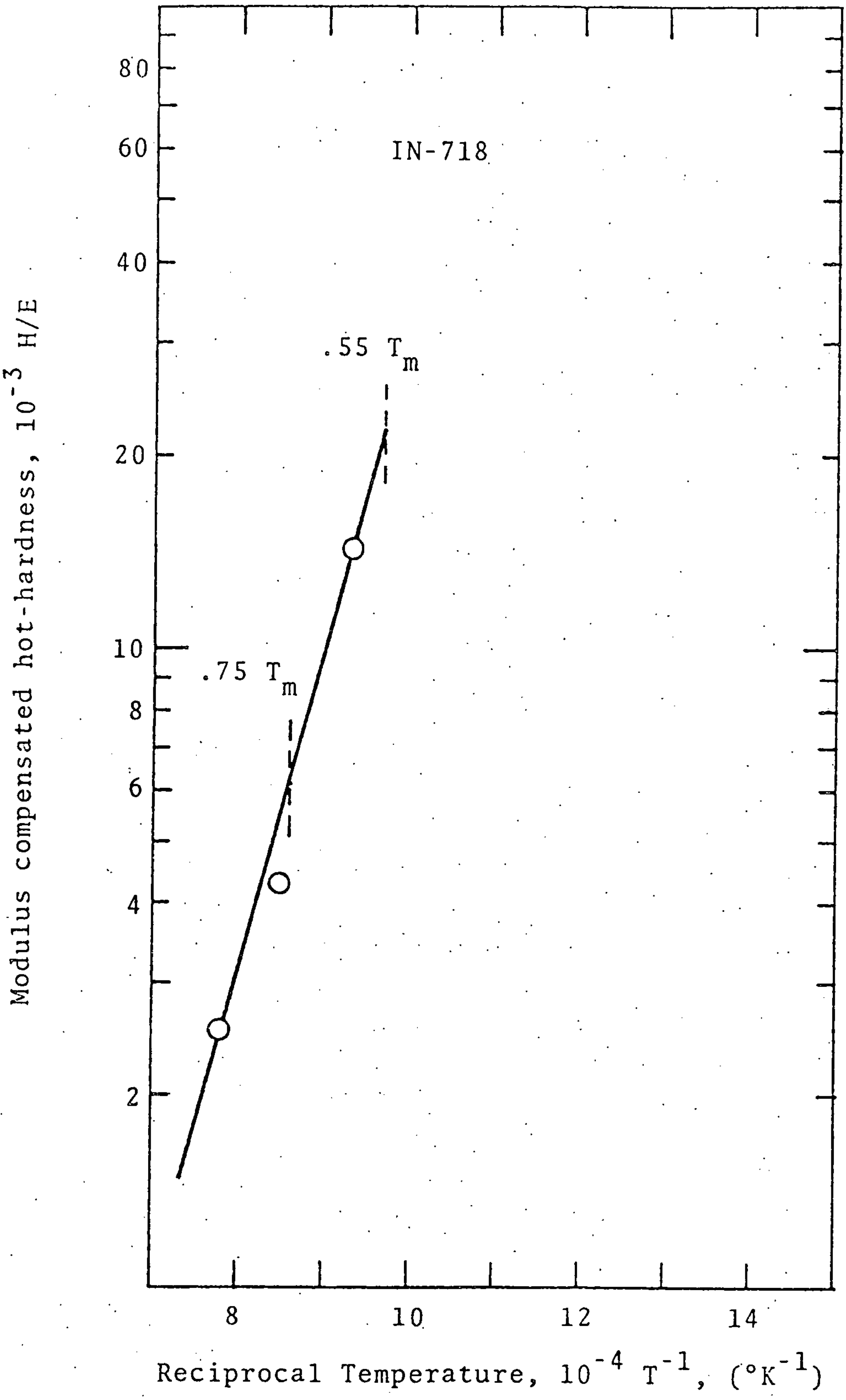

Fig. 7.9 Modulus compensated hot-hardness of IN-718 as a function of reciprocal absolute temperature.

This may imply a curve in the log (H/E) US $\frac{1}{T}$ plot for IN-718 around .75 T_m. This circumstance will be further investigated.

Comparison of Hot-Hardness with the Ultimate Tensile Strength was conducted for IN-718 and PE-16 (results are given in Tables 7.II and 7.III and Fig. 7.10). It should be noted that tensile data for the comparison was acquired from alloys belonging to different heats and having varying heat treatments.

Comparisons were carried out using an equation developed by J. R. Cahoon(11):

$$\sigma_u = \frac{H}{2.9}\left(\frac{n}{.217}\right)^n \qquad (7.4)$$

where n is the strain hardening exponent.

For IN-718 values for U.T.S. are in good agreement up to about 650°C. Here it can be seen that σ_u calculated gives a higher value than σ_u experimental.

For PE-16 the agreement is good being within 20% at the lower temperatures, and becomes better at the higher temperatures.

Considering the circumstances, though, agreement may be considered as generally good, and further investigation will be conducted using materials more nearly identical in future tensile comparisons and obtaining a strain hardening value (n) from an elevated temperature Meyer's hardness measurement.

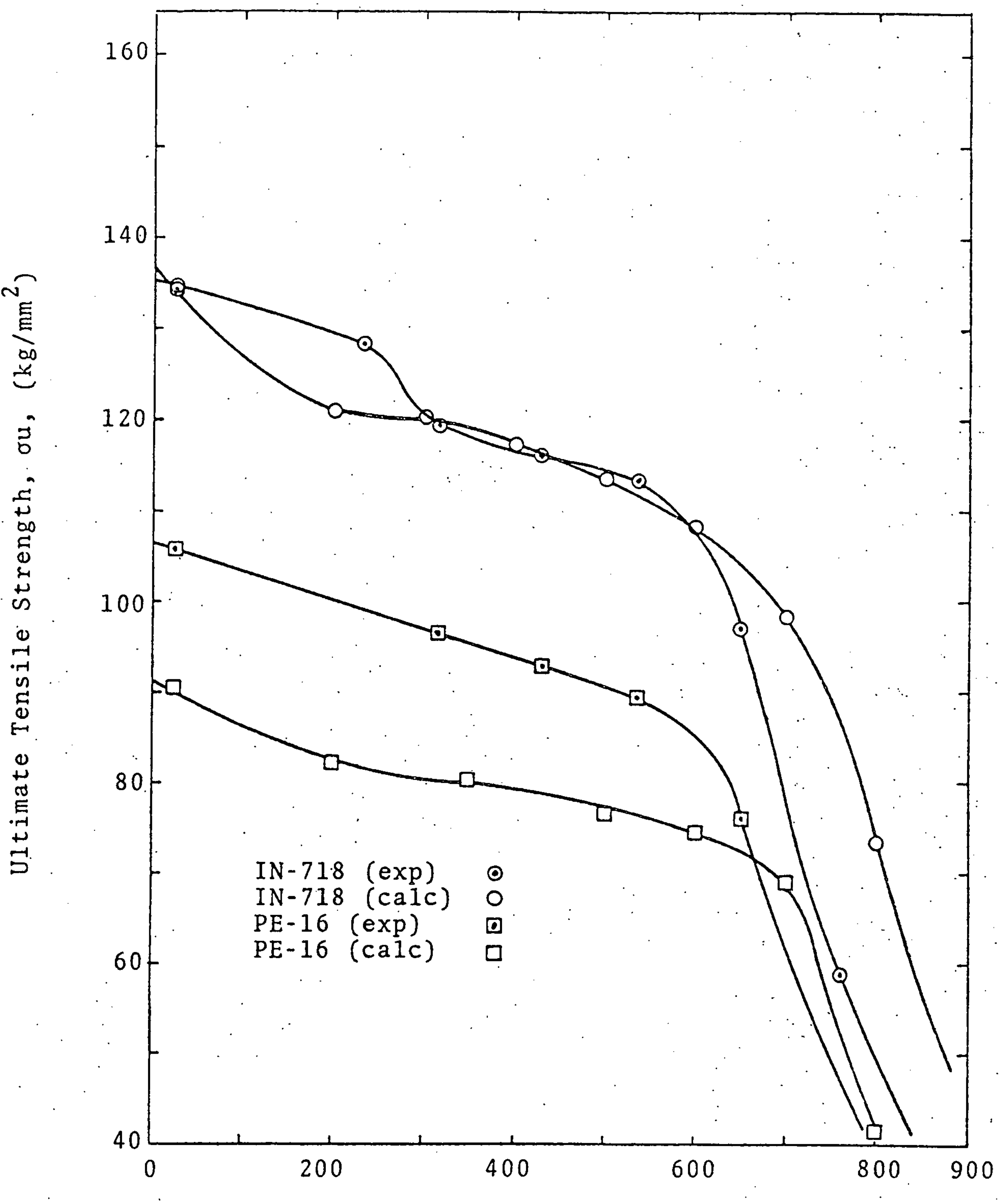

Fig. 7.10 Calculated and experimental ultimate tensile strength of IN-718 and PE-16 as a function of temperature.

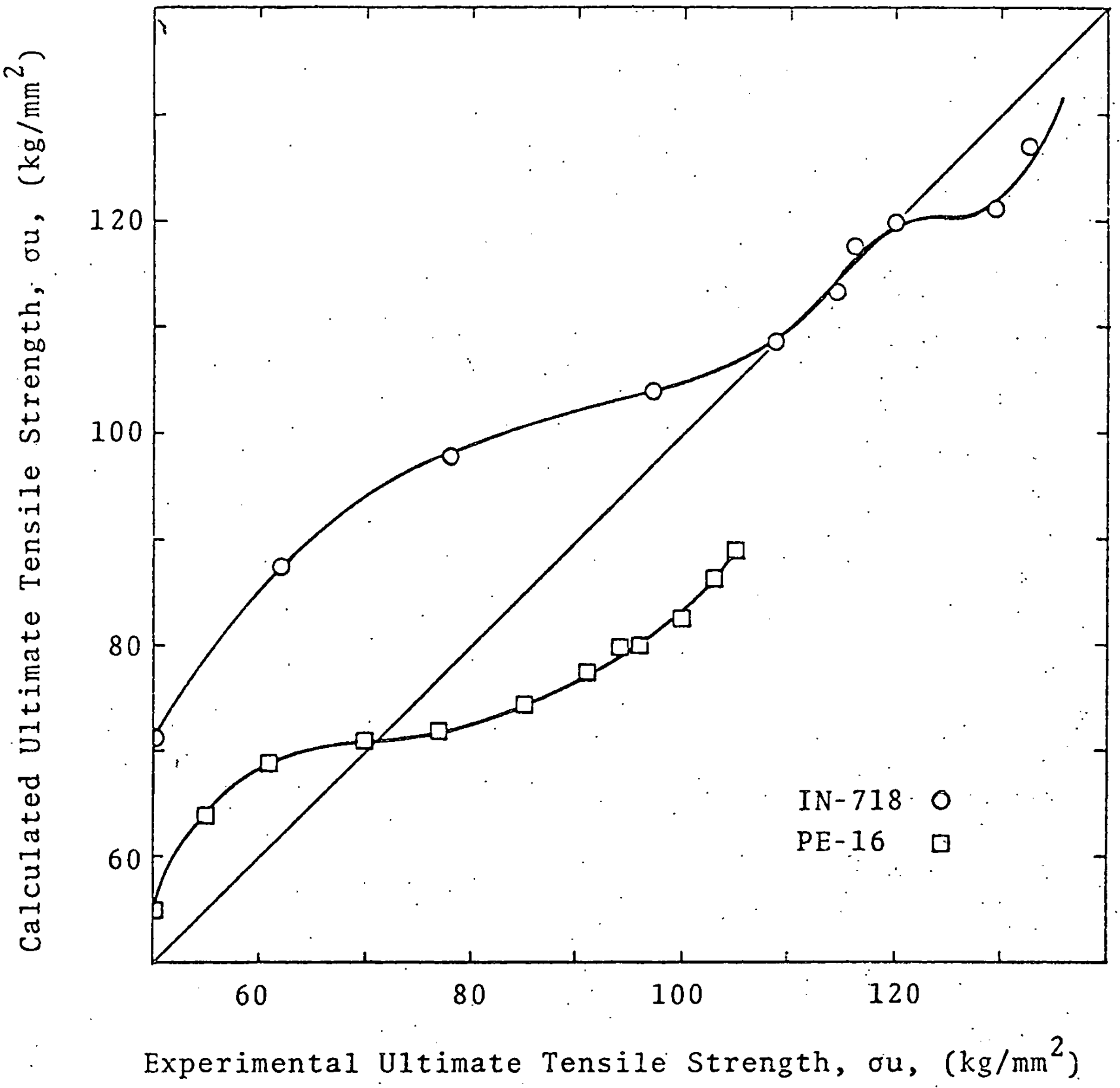

Fig. 7.11 Comparison of the calculated and experimental tensile strengths of IN-718 and PE-16 for various test temperatures.

7.1.3 REFERENCES

1. ORNL 5237, Mechanical Properties Test Data for Structural Materials Quarterly Progress Report for Period Ending October 31, 1976, pp. 315-323.

2. F. Garofalo, "Properties of Crystalline Solids," ASTM Special Technical Publication No. 283, p. 82, (1960).

3. F. Garofalo, R. W. Whitmore, W. F. Domis, and F. Von Gemmingen, Trans. AIME, 221, p. 310 (1961).

4. ORNL 5237, Mechanical Properties Test Data for Structural Materials Quarterly Progress Report for Period Ending October 31, 1976, p. 323.

5. Cuddy, L. J., Met. Trans., 1, pp. 395-401 (1970).

6. Yu, Chien-Chih, M.S. Thesis, University of Cincinnati, Cincinnati, Ohio, 1973.

7. ORNL 5237, Mechanical Properties Test Data for Structural Materials Quarterly Progress Report for Period Ending October 31, 1976, p. 328.

8. Garofalo, F., Fundamentals of Creep and Creep-Rupture in Metals, the MacMillan Company, New York, N. Y., pp. 66-73 (1965).

9. J. Larsen-Badse, Trans. JIM, 9, 312 (1968).

10. O. D. Sherby, P. E. Armstrong, Met. Trans., 2, p. 3479 (1971).

11. J. R. Cahoon, Met. Trans., 3, 3040 (1972).

12. ORNL 5150, Mechanical Properties Test Data for Structural Materials Quarterly Progress Report for Period Ending April 30, 1976, pp. 262-269.

13. Nuclear Systems Materials Handbook Part I, Group 4, Section 5, Table on Dynamic Youngs Modulus (1976).

APPENDIX F

PROGRESS REPORT FOR PERIOD ENDING APRIL 30, 1977

7.1.1 INTRODUCTION

The objective of this program is to (a) evaluate the time, temperature and stress-dependent mechanical properties of reactor structural materials, (b) determine the relationship of these properties to the microstructure, (c) show the contribution of the microstructure to the internal stress fields and the subsequent influence on microcracking and the grain boundary sliding behavior during the normal plastic deformation at elevated temperatures and (d) demonstrate the relationship of the hot micro-hardness properties with the hot-tensile properties of a class of commercial and advanced alloys presently under investigation at other laboratories. Special consideration is being given to operating conditions typical of nuclear reactor applications, including the knowledge that radiation environment can influence the substructure of these metals, a circumstance which can lead to significant changes in the conventional mechanical property behavior.

7.1.2 EXPERIMENTAL PROGRAM

Transmission electron microscopy has been used as the primary tool to study the deformation substructure of reactor structural materials resulting from creep, fatigue and tensile testing at elevated temperatures. Complementary work using optical microscopy, scanning electron microscopy and hot-hardness testing has been performed to characterize the deformation and failure behavior. New work is underway to perform similar studies on the Commercial, the Developmental and the Fundamental alloys being evaluated in the National Alloy Developmental Program with particular attention on the application of hot-hardness measurement as a strength microprobe.

7.1.2.1 Fatigue Crack Behavior of Incoloy 800 Tested in the Bend and the Push-Pull Mode (A. Ermi and H. Nahm)

Introduction: Fatigue failure is characterized by the initiation, usually at the surface, of a dominant crack and its growth to a critical size. Since the useful life of a component is also governed by crack initiation considerations, it is important that crack initiation be analyzed separately from crack propagation. Several investigators have recognized the importance of this from a design aspect [1-4] as well as a fatigue crack modelling viewpoint [5-7]. However, very few studies have been performed on high temperature alloys in which crack initiation and crack propagation were considered separately.

The present study is concerned with the crack initiation and crack growth behavior of Incoloy 800 low-cycle fatigue specimens tested at elevated temperatures ($T > 0.5\ T_m$). Both push-pull and bend fatigue specimens which were tested at various strain ranges were evaluated. It is recognized that hour-glass and bend specimens are not commonly used for studies of crack growth behavior. However, since crack initiation is accelerated when using standard notched specimens, and since most fatigue life studies do not employ notched specimens, it was decided to investigate the crack behavior of some previously tested push-pull and bend specimens which were used for fatigue life studies.

Experimental Procedures: Push-pull fatigue specimens were machined from Incoloy 800 (Heat No. HH8968A; solution annealed at 1145°C for one hour) into hour-glass shapes and bend-fatigue specimens were machined from Incoloy 800 (Heat No. HH0403A3; hot rolled and solution annealed at 1145°C for one hour) into flat bend-fatigue type configurations. Specimen geometries are shown in Figure 7.1. The chemical compositions of the two heats are given in Table 7.I.

Details of the experimental procedures for the push-pull tests are described elsewhere [8]. The bend-fatigue tests [9] were performed on a 150 in-lb Krouse Plate Bending machine which applies a fixed deflection to the specimen. The load is applied by a rotating cam resulting in a sinusoidal loading wave form. Modifications to the machine were made to provide slower speeds, resistance heating and total strain measurements. The addition of a SCR speed control DC motor, a gear reduction unit and a Graham variable speed reducer provided frequencies in the 0.0083 to 3.0 s^{-1} (0.5 to 180 cpm) range. Resistance heating with voltages of about 1 volt driving up to 1000 amps provided temperatures up to 870°C in air. A spherometer type instrument was used to measure the rise in the arc, from which the total longitudinal strain could be calculated.

The fractured surfaces of the specimens selected for this investigation were examined by scanning electron microscopy (SEM) and micrographs were taken of all specimens in order to make quantitative measurements concerning crack growth. Overlapping micrographs were taken at approximately 400X starting from the edge of each specimen and continuing in the direction of crack propagation to final fracture. For the cases in which several distinct cracks were observed (particularly at the higher strain ranges), only the largest or principal crack was considered in the analysis.

Although all specimens revealed fatigue striations, in areas of some specimens, usually near the early stage of crack growth, the striations were not always visible of clearly defined, probably due to rubbing on crack closure and oxidation which occurred during testing. On these specimens, the number of cycles versus crack length could not be determined directly from counting each striation. As an alternative, the striation density (the number of striations or cycles per unit length, dN/da) from areas in which the striations were distinguishable were plotted against crack length. By assuming a continuous crack growth behavior, a smooth curve was constructed and was graphically integrated to obtain the number of cycles at various crack lengths.

Results and Discussion: The fatigue data[10,11] for the thirteen specimens used in this study is given in Table 7.II. Montages were constructed for all but three of the specimens. The three which were not photographed displayed either erratic crack growth behavior or they contained much area in which the striations were not clearly defined. For example, at 649°C and 0.50% strain, the bend fatigue sample revealed a large number of striations on a plane normal to the fracture surface.

Typical montages for both the push-pull and bend-fatigue specimens are shown in Figures 7.2a and 7.2b respectively. The paths chosen represent areas of crack propagation in which the striations were best seen.

In general, for the push-pull specimens tested at 0.5% strain range, one principal crack initiated at the surface and propagated across the specimen until final fracture near the opposite edge (see Figure 7.2a). However, at the higher strain, 2.0%, several cracks were initiated during the test with fracture occurring at an area surrounded by various crack fronts (see Figure 7.3).

For the bend-fatigue specimens, at both 0.5% and 2.0% strain, several cracks were observed to emanate from both of the long edges and propagate toward the central neutral zone where fracture occurred (Figure 7.2b).

From the montages of the ten remaining specimens, plots of the number of cycles per unit length, dN/da, versus crack length, a, were made. These curves were integrated to obtain the number of cycles at different crack lengths. The integration method was checked on specimens in which the striations were readily countable, the difference being no more than ∿ 5%.

In some recent fatigue studies on 304 SS at 593°C, Maiya[12-14] used one approach to separate the number of cycles to failure, N_f, into the number of cycles to initiate a crack, N_o, plus the number of cycles during crack propagation, N_p. Let N_o be defined as the number of cycles to initiate a crack of the size of the grain diameter, and assume that log a (where a is the crack length) is proportional to N during the early stages of crack propagation. The curves of log a versus N can then be extrapolated to determine the number of cycles to initiate a crack of length a_o, approximately the grain diameter size.

The curves of crack length versus number of cycles are shown in Figures 7.4 and 7.5 for all of the specimens. The grain sizes for the push-pull and bend-fatigue specimens, as determined by the line intercept technique, were 0.13 mm and 0.12 mm respectively[15]. Therefore, by extrapolating the curves to $a_o = 0.1$ mm. values of N_o, and consequently N_o/N_f, the fraction of the fatigue life in crack initiation could be determined. These values are given in Table 7.III.

A comparison of Maiya's push-pull data for 304 SS at 593°C[13] with the push-pull data for Incoloy 800 from this study is illustrated in Figure 7.6, where the plastic strain range is plotted versus the fraction of the fatigue life for crack initiation. At the temperatures investigated for Incoloy 800 (all of which were greater than 0.5 T_m, T_m being the absolute melting temperature), the fraction of cycles spent for crack initiation varied only slightly with the plastic strain range, and appeared to be insensitive to temperature.

The push-pull and bend-fatigue modes are compared for Incoloy 800 in Figure 7.7. For the bend specimens, crack initiation was again insensitive to temperature at the temperatures investigated. However, the fraction of the life spent in crack initiation showed a strong dependence on the plastic strain range: at the low plastic strain ranges (.2%), crack initiation occupied 80% of the total life; at high plastic strain ranges (1.5%), virtually no time was consumed for crack initiation, a crack being immediately propagated with each cycle.

The above results are consistent with the fatigue life data for Incoloy 800 (Table II). At high strain ranges the push-pull specimens had a slightly longer fatigue life, and the fraction of time spent for crack nucleation reflects this. At low strain ranges the fatigue lives of the bend-fatigue specimens were nearly double those of the push-pull, and from Figure 7.7, it is seen that a significantly longer time is spent in crack nucleation for the bend tests.

Summary: Scanning electron microscopy was used to investigate crack initiation and crack propagation in Incoloy 800 push-pull and bend specimens fatigued at elevated temperatures (> 0.5 T_m). Observations indicated that:

(1) Growth rates throughout the tests with the exception of the constant growth rates displayed at the lower strain.

(2) Initially, but decreasing growth rates after some time.

(3) For a fixed strain range, the fraction of fatigue life to initiate a 0.1 mm crack appeared to be insensitive to the temperatures investigated for both push-pull and bend modes.

(4) The fraction of fatigue life to initiate a 0.1 mm crack varied only slightly with the plastic strain range for the push-pull specimens, but was strongly dependent on the strain for the bend specimens.

7.1.2.2 A Study of the Plastic Zone Around a Fatigue Crack in 304 SS (A. Ermi)

The plastic zone around the fatigue crack of a 304 SS compact tension specimen is being studied by microhardness measurements, SEM and TEM. The specimen, machined from a 0.5 inch (nominal) plate was solution annealed, and tested at 538°C. The test was run at a stress ratio R

(R = σ min/σ max) of 0.05 and at a frequency of 0.067 5' (4 cpm). Further details of the material and testing can be found elsewhere(16). The results of the fatigue crack growth rate (da/dN) versus the stress intensity factor range (ΔK) are presented in Figure 7.8.

Microhardness measurements were made on an electropolished region surrounding the crack tip, part of which is shown in the SEM micrograph of Figure 7.9. A hardness value ($DPH_{200\ gm.}$) was assigned to each indent position by averaging the hardness at that position with its four nearest neighbors (except at the edge of the crack where the values were determined by the single indents). When these values were plotted, hardness contours could be easily drawn in the crack tip vicinity as in Figure 7.10.

The specimen is currently being prepared for transmission electron microscopy of various sections near the crack tip.

7.1.2.3 Stress-Temperature Effects on Substructure

(R. Billings)

Experimental Results on Mechanical: A summary of fourteen creep-rupture tests is presented. The purpose of this investigation was to determine the stress-temperature-strain rate-substructure interrelationships developed during creep of A.I.S.I. 330 Stainless Steel. All creep-rupture tests were the conventional constant load type conducted in an air atmosphere at elevated temperatures. The details of the testing apparatus and specimen geometry have been reported elsewhere.(17) The specimens were subjected to one of two different pre-test solution anneals after machining. The difference between the two annealing treatments was that one treatment ended with a fast furnace cool at vacuum in a vacuum furnace. The other involved sealing the specimens inside evacuated quartz tubes, heating the sealed tubes in an air atmosphere furnace followed by a water quench. It is estimated that the fast furnace cooling rate is comparable to a normal air cooling rate. The temperature, duration, and vacuum pressure were identical for both treatments: 1100°C ± 10°C, 1800S, 1.33 E-03 Pa, respectively.

Table 7.IV presents the raw creep-rupture data generated in this study. All strain and strain rate values were determined graphically from creep curves generated by either a dial indicator or a linear variable differential tranducer placed in the load train of the creep stand. Either method yields strain values accurate to 0.02%. It can be seen from Table 7.IV that A.I.S.I. 330 Stainless Steel exhibits tendencies commonly found in most other stainless steels during high temperature creep deformation. For constant test temperature the strain on loading and the minimum creep rate both decrease with a decrease in the initial applied creep stress. For constant initial applied creep stress the minimum creep rate and the time to rupture increase and decrease respectively with an increase in test temperature. These trends are in agreement with the creep

behavior of many metals. In the present study no unclassical creep behavior has been observed.(21)

Figures 7.11 and 7.12 quantitatively present the relationships discussed in the preceding paragraph. Figure 7.11 shows the logarithm of the applied creep stress plotted versus the logarithm of the resulting minimum creep rate at various constant test temperatures. The figure demonstrates the strong stress dependence of the minimum creep rate for constant test temperature. Small changes in the applied creep stress cause large changes in the resulting minimum creep rate. Although the axes of Figure 7.11 have been compressed such that this stress dependency is not readily apparent, this is the case.

The data utilized to construct Figure 7.11 can be adequately described by the equation:

$$\dot{e}_s = A'\sigma_a^{\,n} \qquad [7.1]$$

where $\dot{e}_s$ = minimum creep rate, s^{-1}

σ_a = initial applied creep stress, MPa

A' = a constant dependent on temperature and structures, s^{-1} MPa^{-n}

n = dimensionless stress exponent (>0).

Table 7.V presents the values for A' and n at various test temperatures obtained from a least squares fit of the stress, strain rate data. Because of the small data base no statistical confidence limits are given in the table. Their values would be statistically meaningless. However,

trends do exist such that A' increases and n decreases with increasing test temperature. These n values are higher than those values reported in the literature for similar alloys.(18,19,20)

Figure 7.12 is a graph of the logarithm of the applied creep stress versus the logarithm of the time to rupture. A power law relationship is observed in this figure and can be described by the equation:

$$t_R = A''\sigma_a^{n'} \qquad [7.2]$$

where t_R = time to rupture, s

σ_a = applied creep stress, MPa

A'' = pre-exponential constant, $sMPa^{-n'}$

n' = dimensionless stress exponent (< 0).

Table 7.V gives the values for A" and n' obtained from a least squares fit of the stress, time to rupture data base. Confidence limits were not calculated for the reasons already mentioned. The value of A" essentially remains constant over the range of test temperatures. The value of n' decreases with increasing temperature.

Figure 7.13 is the logarithm of the time to rupture plotted against the logarithm of the minimum creep rate, after Garofalo et. al.(22) Note that the data for all can be fit by one equation of the form:

$$t_R = \left(\frac{C}{\dot{e}_s}\right)^m \qquad [7.3]$$

where t_R = time to rupture, s

$\dot{e}_s$ = minimum creep rate, s^{-1}

c = a constant, s^{1-m}

m = dimensionless exponent.

The curve in Figure 7.13 represents the equation determined through a least squares fit of the data. The value obtained for C is .25 $s^{0.05}$ and that for $m = 0.95$.

Experimental Results on Substructure Evaluation: This phase of the program utilizes Transmission Electron Microscopy (T.E.M.) to determine the average cell or subgrain size, the mobile dislocation density, the misorientation angle between subgrains, and the types of precipitates found in the ruptured creep specimens. Samples used in T.E.M. were sectioned from the creep-ruptured specimen to an initial thickness of 0.5 mm, ground by hand on wet 600 grit SiC polishing paper to an approximate thickness of 0.2 mm, and finally electropolished in a Fischione Twin Jet Electropolishing Apparatus. The resultant sample for T.E.M. has a tiny pinhole in its center surrounded by an area of thin material transparent to the electron beam in the electron microscope. This thickness is approximately 0.2μm. After much trial and error work it was found that polishing conditions of 15 volts and 2.5 amps/mm^2 yielded optimum results when used in conjunction with an electrolyte consisting of 6% Perchloric acid, 35% Butyl Cellusolve, and 59% methanol, by volume.

Insufficient T.E.M. analysis has been completed to allow significant trends in the cell or subgrain size, the mobile dislocation density, or the misorientation angle to be presented at this time. However, representative T.E.M. micrographs is presented for creep-ruptured samples tested at 701°C under various applied stresses.

Figure 7.14 presents the basic substructures developed in specimens crept to rupture under various applied creep stresses at a test temperature of 701°C. Cells developed in the specimens crept at 241.3 MPa and 206.8 MPa. Subgrains developed in the specimen crept at 137.9 MPa. The tendency for a material to form a cellular substructure at higher creep stresses and to form a subgranular substructure at lower creep stresses for constant test temperature is well documented in the literature.(18,19,20,22)

Figure 7.15 shows the typical mobile dislocation structure and precipitate morphology for the same set of creep ruptured specimens. The mobile dislocation structures consists of a complex array of tangles, dipoles, and forest dislocations. Three different recurring precipitate shapes have been observed during T.E.M. analysis; cubic, spherical, and rod-like. It should be noted that matrix precipitates were not observed in large amounts in as-annealed material. After rupture, precipitates have been found in the grain and twin boundaries as well as peppered through the matrix.

<u>Discussion on Mechanical Properties</u>: Solution Anneal Treatments: The previously mentioned pair of pre-test solution anneal treatments used in this study gave rise to material exhibiting remarkedly similar creep behavior for

identical test conditions, as shown in Table 7.IV and Figures 7.11 and 7.13. This observation was unexpected because the final as-annealed microstructures attained by each of the differently annealed materials showed a striking difference. Optical microscopy revealed that in the furnace cooled material a continuous network of second phase, most probably $M_{23}C_6$ carbide, had formed in all grain and twin boundaries. Selected area diffraction has partially confirmed that the precipitates are in fact $M_{23}C_6$. On the other hand the water quenched material exhibited a slight degree of this precipitation but no continuous network has been observed. The network of carbides was not unexpected, however. Austenitic stainless steels are known to become sensitized at temperatures close to 650°C.(23) Sensitization is defined as the formation of a network of chromium carbides throughout the grain and twin boundaries.(23) The nominal composition of A.I.S.I. 330 Stainless Steel indicates that only negligible amounts of the stabilizing elements Ti and Cb are present in the material. These elements are strong carbide formers. When present in sufficient amounts, these stabilizers form their respective carbides in the matrix tying up the carbon so that the $Cr_{23}C_6$ carbides can not form in the boundaries of the material. Because of the 330 composition, the slower cooling rate experienced by the furnaced cooled samples, and the temperatures involved, the furnaced cooled samples became sensitized. Apparently, the water quenched samples become sensitized to some degree during creep testing. Therefore the two different solution anneals lead to similar creep behavior.

Mechanical Properties: As seen from Figures 7.11 and 7.13, the high temperature creep behavior is fairly well described in the 500°C to 800°C temperature range for stress levels of 68.9 MPa through 413.7 MPa by the equations:

$$\dot{e}_s = A' \sigma_a^n$$

$$t_R = A'' \sigma_a^{n'}$$

$$t_R = \left(\frac{C}{\dot{e}_s} \right)^m$$

The creep behavior of this material is strongly stress dependent for constant temperature. It is strongly temperature dependent for constant applied creep stress, also. The minimum creep rate changed by six orders of magnitude for a 300°C temperature change. The time to rupture changed by four orders of magnitude for the same temperature interval.

It is well known that in creep, high test temperatures and low stress levels enhances subgrain formation. The deformation rate is low in general and the test time is long. The dislocations in the material feel an effective stress resulting from the difference in the applied stress and the internal stress generated in the material by the elastic interactions between the mobile dislocations and the barriers to their motion e.g. forest dislocations, tangles, precipitates.(24) This internal stress is a measure of the strain hardening-recovery balance in the material. The effective stress is the thermal component of the stress which drives the dislocation glide mechanism for deformation. Subgrains develop when the degree of work hardening is low and the temperature is high. Large effective stresses arise for these conditions and the dislocations move easily to lower their energy. They form low angle boundaries within the grains. These are the subgrain boundaries.

By comparison, material tested at lower temperatures and higher stresses tend to form a cellular substructure. Under these conditions the degree of work hardening is increased and the effective stress is reduced. The dislocations cannot move as easily to lower their energy. Localized tangles of dislocations form. These tangles are the usually poorly defined cell boundaries.

In general, cells are smaller in size than are subgrains. In the present study the cells developed during creep at 701°C are observed to be highly elongated along one axis, most probably the macroscopic stress axis. See Figure 7.15. The subgrains observed are more regular in shape.

Inspection of Table 7.V shows an apparent change in creep mechanism occurring at temperatures of close to 650°C. The values for the stress exponents n and n' in the power law equations were found to be much higher for the 600°C temperatures than the values obtained at higher temperatures. At the higher temperatures, the stress exponent values are quite similar. It is known that stress-enhanced diffusional mechanisms become operative at temperatures above $0.5T_m$ (half the melting temperature).(25) Apparently, in the present study as the test temperature is increased, the importance of stress in determining the resultant creep behavior decreases. It is quite possible that a diffusionally controlled creep mechanism becomes the rate controlling mechanism. Recovery through the climb of dislocations would become a predominent mechanism at the expense of the lower temperature dislocation-glide type processes. However, more work is needed to verify this idea.

Discussion on Substructure: Although a qualitative discussion has been utilized to aid in describing the creep-rupture properties of A.I.S.I. 300 Stainless Steel, a thorough discussion of the deformation substructure will be forgone until further T.E.M. analysis is completed.

7.1.2.4 Hot Hardness Testing Program (F. Price)

Instrument Disposition: The recent oxide films, found on hardness samples, and cracks in the Tantalium heating element in the testing furnace have prompted an overhaul on the Hot Microhardness Tester. Due to this activity causing extensive down time on the instrument, no new data is available for this quarter's report.

The overhaul has generally been confined to the vacuum system with some attention given to aligning and lubricating the indentor mechanism.

Results: The vacuum in the pressure vessel, using the aluminum cover plate instead of the indentor assembly, now reaches 3.0 E-04 Pa in contrast to 6.6 E-02 Pa previous to the overhaul.

Complete realignment and lubrication of the indentor mechanism has produced a much smoother and more consistent operation. This will surely lead to extended indentor life.

Completion of the project is expected shortly. For project status refer to Table 7.VI.

7.1.2.5 Substructural Development in Hot Tensile Testing of 304 Stainless Steel (A. Ermi and J. Foulds)

Tensile tests were run on 304 S.S. at 650°C (923°K) and at a strain rate of 3.17 E-04 s^{-1}. Specimens 6.35mm (1/4 inch) in diameter and 50.8mm (2 inches) gauge length were machined from 15.9mm (5/8 inch) rod (Heat 9T2796) and solution annealed at 1093°C for 30 minutes.

One specimen was run to failure and three others tested to true strains of 2.8, 8.5 and 17.4%. All the tests showed good reproducibility.

Microhardness measurements, optical and transmission electron microscopy results will be reported in the future.

7.1.2.6 A Study on Subgrain/Cell Development During Creep Deformation (J. Foulds)

Mechanical Test Data: Interrupted tests were completed on 330 S.S. specimens tested at 652°C (925°K) and 172.4 MPa (25 ksi) as planned in the previous report(21). The strain-time curves obtained were reproduced in each case. Table 7.VII contains the data for the interrupted tests.

Transverse sections were taken from each of the specimens AN330-CF08 through to AN330-CF14 and studied optically. As for the set of specimens tested at 652°C and 241.3 MPa (35 ksi)[1] no appreciable grain size variation occurred.

Cracking and Fracture: Figure 7.16 shows a stereo pair of SEM fractographs of the specimen tested at 652°C and 172.4 MPa. These indicate that a large amount of transgranular cracking was responsible for failure. However, unlike as in the test-run at 241.3 MPa, the number of triple point cracks observed on the ruptured longitudinal and transverse sections was low. As has been suggested, grain boundary migration at longer test times is less inhibited. Cracks were observed to form later in the tertiary creep stage for the longer test time. Also, the intergranular form of cracking appeared to occur more than for the specimen tested at 241.3 MPa (compare with figure 7.2, p. 337 of previous report).

As expected, optical microscopy showed a large number of R-type cavities for the specimen tested at the lower stress (172.4 MPa) compared with the one tested at the higher stress (241.3 MPa).

Room Temperature Microhardness: Microhardness measurements (DPH) were made on longitudinal sections of specimens ruptured at 652°C and 172.4, 206.9, and 241.3 MPa. The results were plotted along with the data in the last report.(21) (See figure 7.17).

The large difference between the work-hardening at lower temperatures (652°C) and that at higher temperatures (701°C) for the same applied stress is obvious. The curves, however, still exhibit the same "parallelism" observed earlier, indicating similar work-hardening characteristics along the section.

Transmission Electron Microscopy: TEM studies are underway on transverse sections of specimens AN330-CF01 through to AN330-CF15 to aid in substructural development analysis for the two cases. All micrographs will be reported along with a final analysis.

7.1.3 REFERENCES

1. S. S. Manson, International Journal of Fracture Mechanics, 2, (1966) 327.
2. P. J. E. Forsyth, Acta Metallurgica, 11, (1963) 703.
3. C. Laird and G. C. Smith, Philosophical Magazine, 8, (1963) 1945.
4. A. J. McEvily and R. C. Boettner, Acta Metallurgica, 11, (1963) 725.
5. B. Tomkins, Journal of Engineering Materials and Technology, (Oct. 1975) 289.
6. H. D. Solomon, General Electric TIS Report, 71-C-327 (Nov. 1971).

7. S. P. Lynch, Metal Science, 9, (1975) 401.

8. T. Slot, P. H. Stenz and J. T. Berling, ASTM STP-465 (1969) 100.

9. T. H. Bassford, Private Communication, Huntington Alloy Division, International Nickel Company, Huntington, West Virginia.

10. J. B. Conway, J. T. Berling and R. H. Stenz, Metallurgical Transaction, 3, (1972) 1633.

11. J. B. Conway, General Electric Company, Nuclear Systems Program, Cincinnati, Ohio, Report Number GEMP-732 (1969).

12. P. S. Maiya and D. E. Busch, Metallurgical Transactions, 6A, (1975) 1761.

13. P. S. Maiya, Scripta Metallurgica, 9, (1975) 1141.

14. P. S. Maiya, Scripta Metallurgica, 9, (1975) 1277.

15. H. Nahm, Ph.D. Thesis, University of Cincinnati, Cincinnati, Ohio (1975).

16. L. A. James, "The Effect of Frequency upon the Fatigue-Crack Growth of Type 304 Stainless Steel at 1000F," Stress Analysis and Growth of Cracks, Proceedings of the 1971 National Symposium on Fracture Mechanics, Part I, ASTM STP 513, American Society for Testing and Materials, 1972, pp. 218-229.

17. Oak Ridge National Laboratory, Mechanical Properties Test Data for Structural Materials Quarterly Progress Report for Period Ending April 30, 1976, ORNL-5150 pp. 375-379.

18. F. Garofalo, Fundamentals of Creep and Creep-Rupture in Metals, The Macmillan Co., N.Y., 1965.

19. Chien-Chih Yu, The Effects of Stress on Creep Properties and the Correlations With Substructures of A.I.S.I. 304 and 316 Stainless Steels, Master of Science Thesis, University of Cincinnati, 1973.

20. R. Bhargava, Ph.D. Dissertation, University of Cincinnati, 1975.

21. Oak Ridge National Laboratory, Mechanical Properties Test Data for Structural Materials Quarterly Progress Report for Period Ending January 31, 1977, ORNL-5255, pp. 144.

22. F. Garofalo et.al., Creep and Creep-Rupture Relationships in an Austenitic Stainless Steel, Trans. of Met. Soc. of A.I.M.E., Vol. 221, April 1961, pp. 310-319.

23. J. G. Parr, A. Hanson, An Introduction to Stainless Steel, American Society for Metals, 1965, pp. 55,56.

24. O. Chopra, K. Natesan, Interpretation of High-Temperature Creep of Type 304 Stainless Steel, Met. Trans., Vol. 8A, April 1977, pp. 633-638.

25. H. Frost, M. Ashby, Deformation Mechanism Maps for Pure Iron, Two Austenitic Stainless Steels, and a Low-Alloy Ferritic Steel, private communication.

7.1.4 ACKNOWLEDGMENTS

This work was supported by the U. S. Energy Research and Development. Administration under Contract No. Ey-76-S-02-2107.A001, 189A CX 008. The University would like to thank T. H. Bassford of Huntington Alloys for providing the tested bend fatigue Incoloy 800 specimens and Lee James of the Westinghouse Hanford Company for providing the tested 304 SS Compact Tension Specimen.

INDEX

TABLE 7.I

CHEMICAL COMPOSITION* OF INCOLOY 800

Element	Heat HH8968A (Push-Pull)	Heat HH0403A3 (Bend-Fatigue)
Iron	44.38	45.06
Nickel	31.41	32.40
Chromium	21.61	20.26
Manganese	0.84	0.73
Aluminum	---	0.45
Copper	0.45	0.29
Silicon	0.29	0.29
Sulfur	0.008	0.007
Carbon	0.05	0.07

---

*Values given in weight percent.

TABLE 7.II

SUMMARY OF LOW CYCLE FATIGUE DATA FOR INCOLOY 800

Test Mode	Specimen Number	Test Temp. °C	Total Strain Range, $\Delta\varepsilon_t$, %	Plastic Strain Range, $\Delta\varepsilon_p$, %	Stress Range $\Delta\sigma$ MPa(psi)		Fatigue Life, N_f, Cycles
Push-Pull	2G55	649	0.49	0.19	471.8	(68430)	11000
	2I57	704	0.49	0.20	440.9	(63950)	6055
	2W23	760	0.49	0.24	365.2	(52970)	4046
	2A73	649	1.98	1.47	781.8	(113390)	507
	2U21	704	1.97	1.53	671.0	(97320)	407
	2B26	760	1.97	1.61	531.1	(77030)	420
Bend-Fatigue	H-12-1-2	649	0.50	0.18(1)	NA(2)	NA	22025
	H-12-2-1	704	0.50	0.20	NA	NA	15100
	H-12-3-3	760	0.50	0.23	NA	NA	7375
	H-12-2-2	704	1.00	0.60	NA	NA	1045
	H-12-1-3	649	2.01	1.5	NA	NA	470
	H-12-2-3	704	2.00	1.5	NA	NA	260
	H-12-3-1	760	2.00	1.6	NA	NA	340

MATERIAL: Solution Annealed Incoloy 800

STRAIN RATE: 4. E-03 S^{-1}

(1) Plastic strain range for bend-fatigue specimen estimated from data for push-pull mode.

(2) NA: Not Available

TABLE 7.III

FATIGUE CRACK INITIATION(1) DATA FOR INCOLOY 800

Test Mode	Test Temp. T, °C	Plastic Strain Range, $\Delta\varepsilon_p$, %	Fatigue Life N_f, Cycles	Crack Initiation N_o, Cycles	Fraction N_o/N_f
Push-Pull	649	0.19	11000	4400±700	0.40±0.06
	704	0.20	6055	2000±300	0.33±.05
	760	0.24	4046	2000±100	0.49±.03
	649	1.47	507	180±10	0.35±.02
	704	1.53	407	80±10	0.195±.025
Bend-Fatigue	704	0.20	15100	12000±200	0.79±0.02
	760	0.23	7375	6000±100	0.81±0.02
	704	0.60	1045	650	0.62
	649	1.5	470	1	0.002
	704	1.5	260	1	0.004

(1) Assuming an initial crack length of $a_o = 0.1\text{mm}$ and $N_f = N_o + N_p$.

TABLE 7.IV - SUMMARY OF THE RAW CREEP-RUPTURE DATA GENERATED FOR A.I.S.I. 300 STAINLESS STEEL CREPT AT VARIOUS TEMPERATURES

SAMPLE CODE	APPLIED STRESS MPa	TEST TEMPERATURE °C	e_p %	e_t[a] %	$\dot{e}_s$ S^{-1}	1/r S	t_2 S	t_R S	e_R %	ε_f %	R.A. %
AN330-CB09	413.7	500	17.39	17.90	1.74 E-09	3.78 E+05	N.A.	3.47 E+06[b]	19.6[b]	16.5[b]	15.2[b]
AN330-CB13	275.8	600	10.09	10.80	3.97 E-07	4.32 E+03	9.25 E+04	2.06 E+05	33.4	40.2	33.1
AN330-CB08	137.9	600	1.10	1.87	3.75 E-10	1.80 E+06	N.A.	1.08 E+07[b]	2.7[b]	2.6[b]	2.5[b]
AN330-CB10	206.8	652	2.14	3.29	2.24 E-06	1.44 E+03	2.20 E+04	8.28 E+04	51.7	74.2	52.4
CBF01	206.8	652	0.61	2.40	2.15 E-06	2.88 E+03	4.18 E+04	9.79 E+04	54.8	69.3	50.0
AN330-CB01	275.8	701	5.00	12.00	2.32 E-04	3.60 E+01	5.40 E+02	9.00 E+02	60.0	58.2	44.1
AN330-CB03	241.3	701	2.70	6.00	9.25 E-05	6.84 E+01	6.12 E+02	2.45 E+03	65.0	77.9	54.1
AN330-CB02	206.8	701	1.50	2.70	2.45 E-05	1.08 E+02	3.06 E+03	1.04 E+04	64.0	83.0	56.4
CBF02	206.8	701	0.85	3.25	2.06 E-05	4.32 E+02	2.41 E+03	1.03 E+04	53.0	63.5	47.0
AN330-CB04	137.9	701	0.19	0.95	1.68 E-06	1.98 E+03	1.80 E+04	1.21 E+05	62.3	87.9	58.5
AN330-CB05	103.4	701	1.13	3.50	1.58 E-07	2.05 E+04	1.49 E+05	9.04 E+05	62.5	73.8	52.2
AN330-CB11	206.8	750	0.52	1.00	5.73 E-05	1.80 E+01	7.02 E+02	3.35 E+03	48.4	87.9	58.5
AN330-CB06	137.9	800	0.45	3.50	1.10 E-04	1.48 E+02	7.20 E+02	2.7 E+03	70.5	92.1	60.2
AN330-CB07	68.9	800	0.09	1.55	7.89 E-07	1.04 E+04	8.93 E+04	2.34 E+05	30.3	37.1	31.0

NOTES:

a - values represent cumulative strain at the end of primary creep
b - values obtained from interrupted tests; not ruptured
N.A. - not applicable
e_p - strain on loading
e_t - cumulative strain at end of transient stage
$\dot{e}_s$ - minimum creep rate

1/r - time to reach 63% of e_t
t_2 - time to end of secondary stage (0.2% offset)
t_R - time to rupture
e_R - engineering rupture strain
ε_f - true fracture strain calculated as $\varepsilon_f = \ln (100/(100 - \%\ R.A.)$
R.A. - reduction in cross sectional area

TABLE 7.V

VALUES FOR THE STRESS EXPONENTS AND PRE-EXPONENTIAL TERMS APPEARING IN THE POWER LAW EQUATIONS DESCRIBING THE CREEP BEHAVIOR OF A.I.S.I. 330 STAINLESS STEEL CREPT AT VARIOUS TEMPERATURES.

Equation / Temperature °C	$\dot{e}_s = A'\sigma_a^n$		$t_R = A''\sigma_a^{n'}$	
	A' S^{-1} $MPa^{n^{-1}}$	n	A'' S $MPa^{n'}$	n'
600	3.04 E-31	9.87	9.95 E+18	-5.60
652	1.19 E-24[a]	7.87	1.29 E+17	-7.03
701	4.77 E-22	7.23	5.31 E+19	-6.83
800	1.85 E-21	7.89	3.08 E+18	-7.08

NOTE:

a - data base for this calculation neglects the sample crept at an applied stress of 241.3 MPa.

TABLE 7.VI

STATUS OF HOT-HARDNESS MATERIALS TESTING PROGRAM

MATERIAL	HEAT NO.	HARDNESS TEST DATA	ANALYSIS OF DATA	
		STATUS	OBJECTIVES	STATUS
IN 706	4865 HK	Incomplete	a,b,c	-
	Other	Complete	a,b,c	b
IN 718	59 FIEY	Complete	a,b,c	a,b,c
M 813	R 74073	Complete	a,b,c	b
PE 16	CO 7206	Complete	a,b,c	a,b
AISI 330SS	14189 (1)	Complete	a,b,c	b,c
	14189 (2)	Incomplete	a,b,c	-
	14189 (3)	Incomplete	a,b,c	-
A-286	C-66251-K2	Incomplete	a,b,c	-
AISI 304 SS	ORNL 5-C, 7-B 1-C, 6-B 813, 796K	Incomplete	a,b,c,d	-

Heat Treatments

(1) 1100°C/1/2 HR in Vacuum/rapid FC

(2) 1065°C/1 HR/AC

(3) 1065°C/1 HR/NQ + 20% CW

(a) Correlation of hot hardness to tensile strength.

(b) Calculation of Effective Activation Energy of Indentation.

(c) Calculation of Effective Activation Energy of Creep.

(d) Evaluation of changes in hot-hardness properties with trace variations in Nb content.

TABLE 7.VII

INTERRUPTED DATA AT 652°C AND 172.4 MPa APPLIED STRESS

SPECIMEN NO.	e (%)	t(sec)	RA %	Expected e (%)
AN330-CF14	1.1	00.0 E03	0.90	2.2
AN330-CF13	1.8	18.0 E03	1.82	3.5
AN330-CF12	3.0	36.0 E03	3.02	4.2
AN330-CF11	3.4	54.0 E03	3.31	5.0
AN330-CF10	4.9	72.4 E03	4.42	5.5
AN330-CF09	30.7	90.0 E03	26.00	22.0

e = Engineering strain
t = time of test
RA = reduction in area

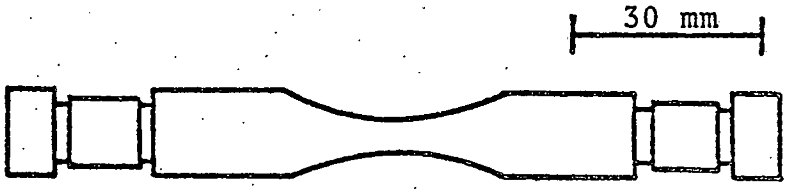

(a) PUSH-PULL SPECIMEN

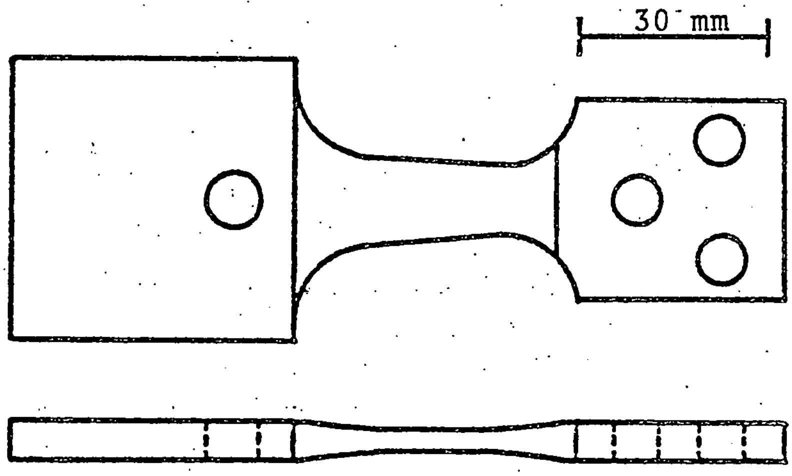

(b) BEND-FATIGUE SPECIMEN

Figure 7.1 Incoloy 800 Specimen Geometries

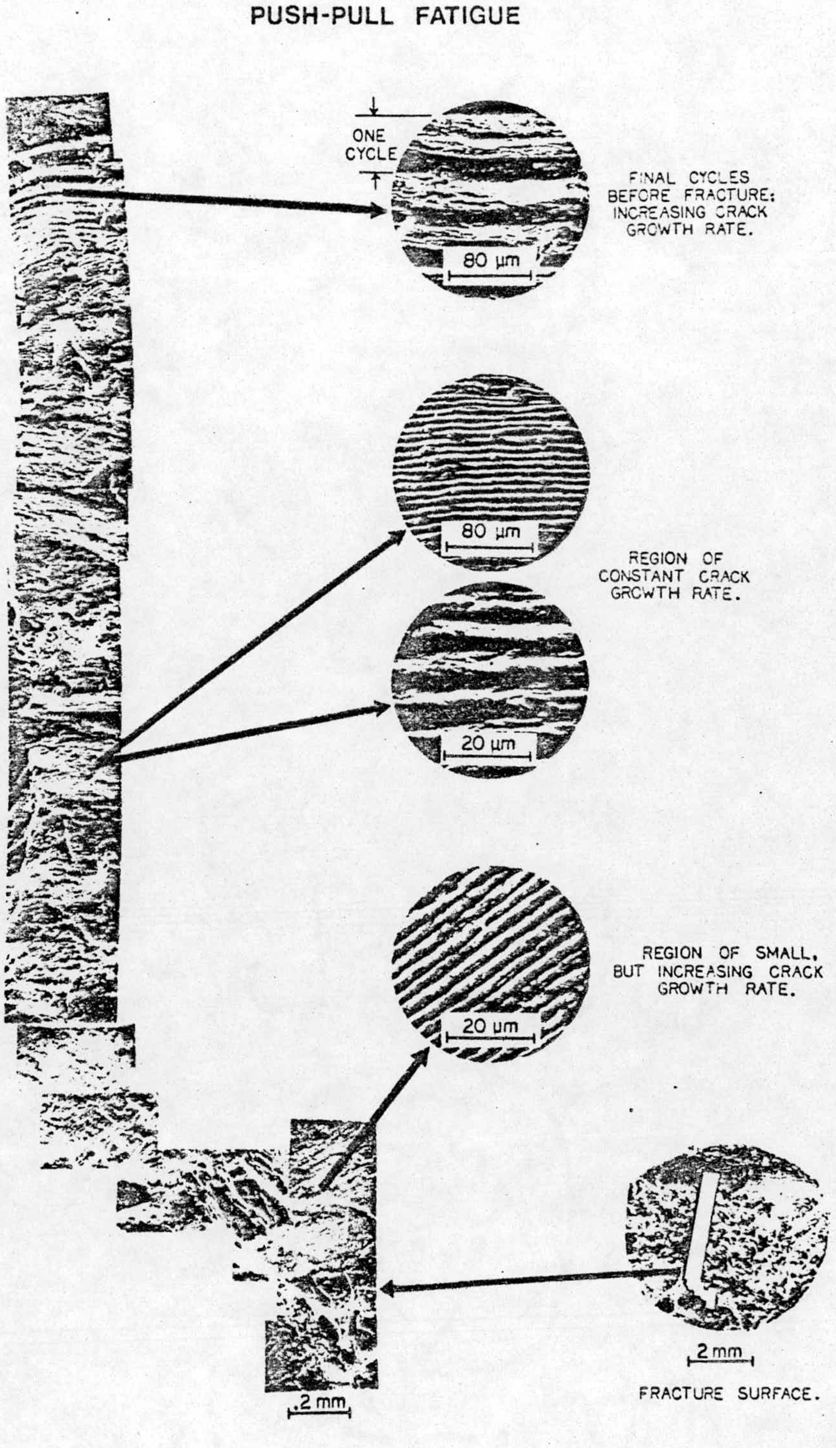

Figure 7.2a Montage of the Push-Pull Specimen No. 2W23; Incoloy 800, 760°C, 0.5% Strain Range.

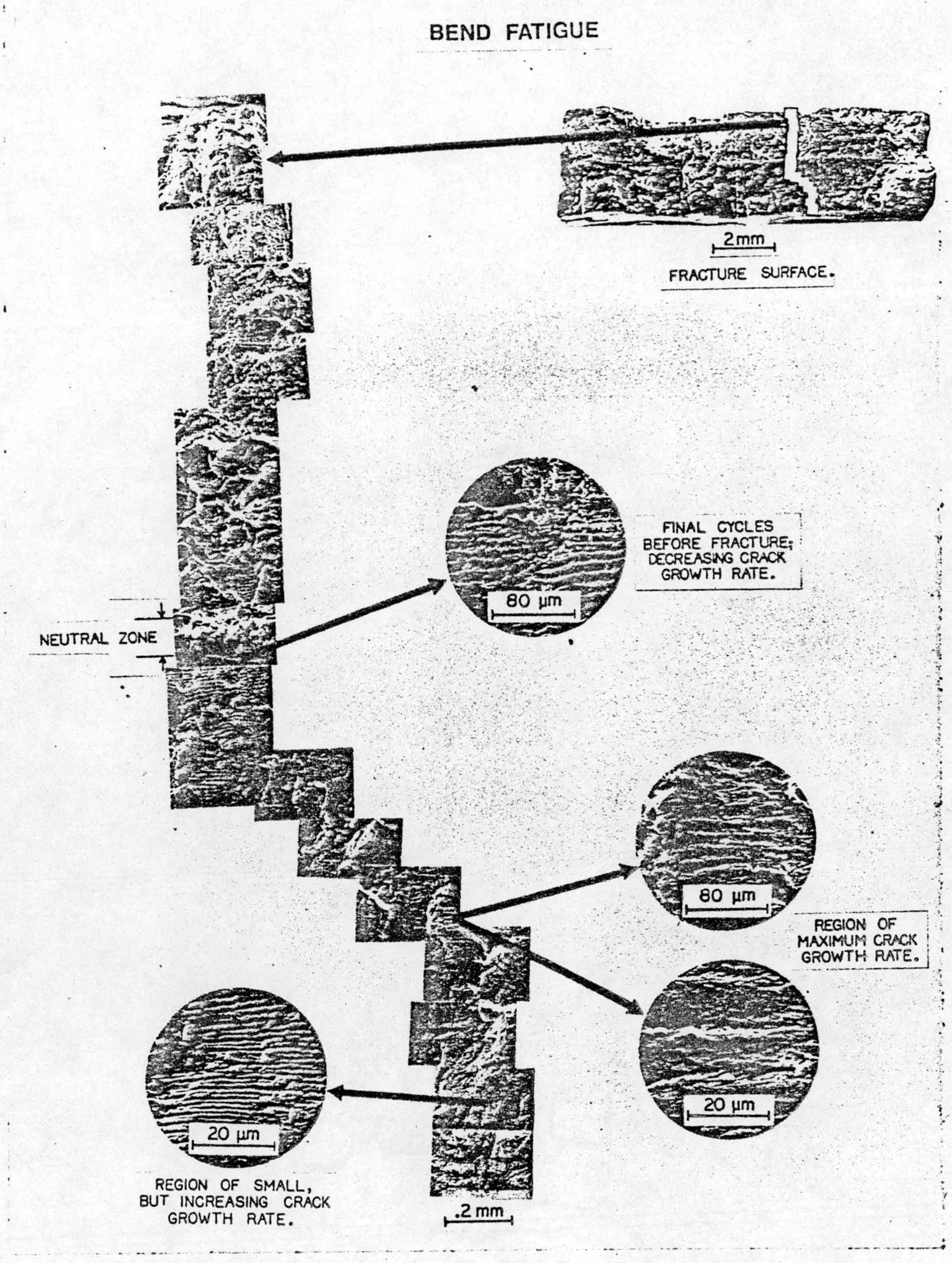

Figure 7.2b Montage of the Bend-Fatigue Specimen No. H-12-2-3; Incoloy 800, 704°C, 2.0% Strain Range.

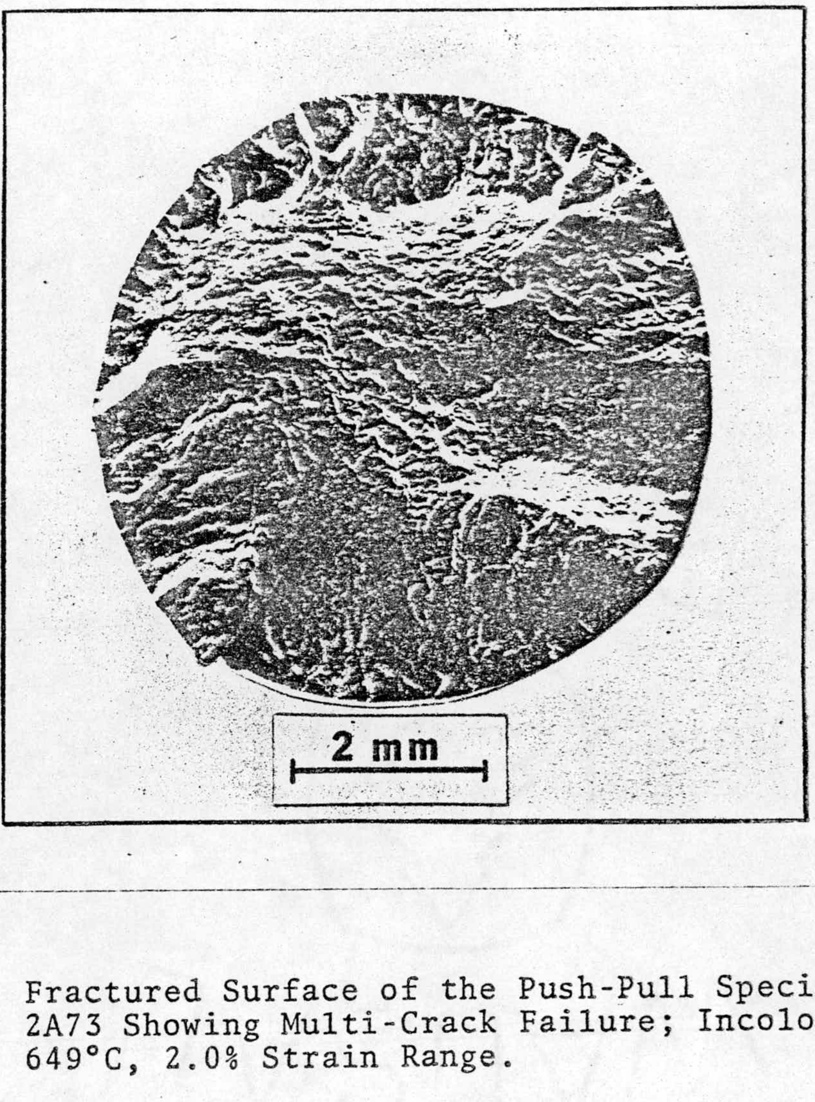

Figure 7.3 Fractured Surface of the Push-Pull Specimen No. 2A73 Showing Multi-Crack Failure; Incoloy 800, 649°C, 2.0% Strain Range.

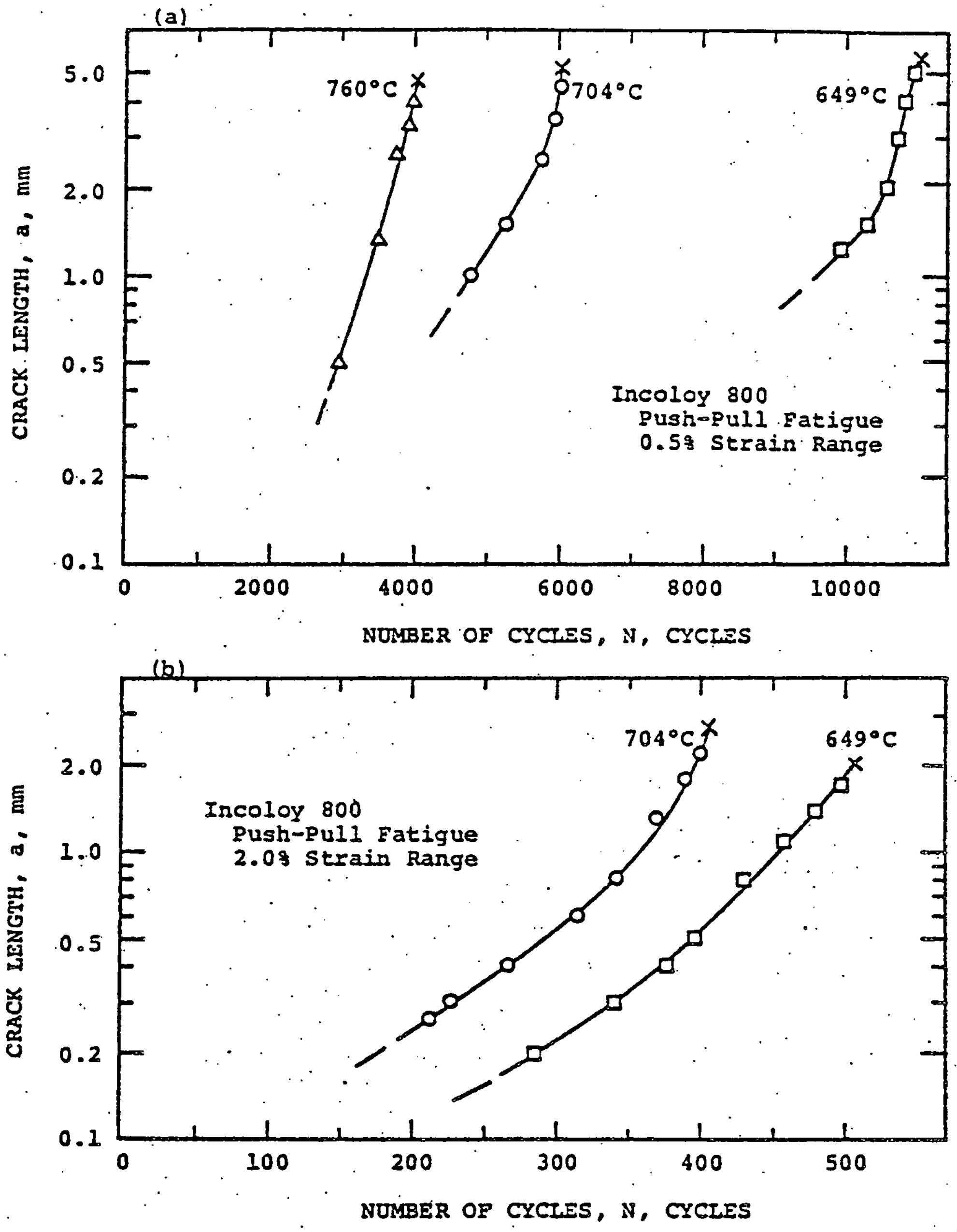

Figure 7.4 Crack Length vs. Number of Cycles for Incoloy 800 Push-Pull Specimens at (a) 0.5% Strain Range and (b) 2.0% Strain Range.

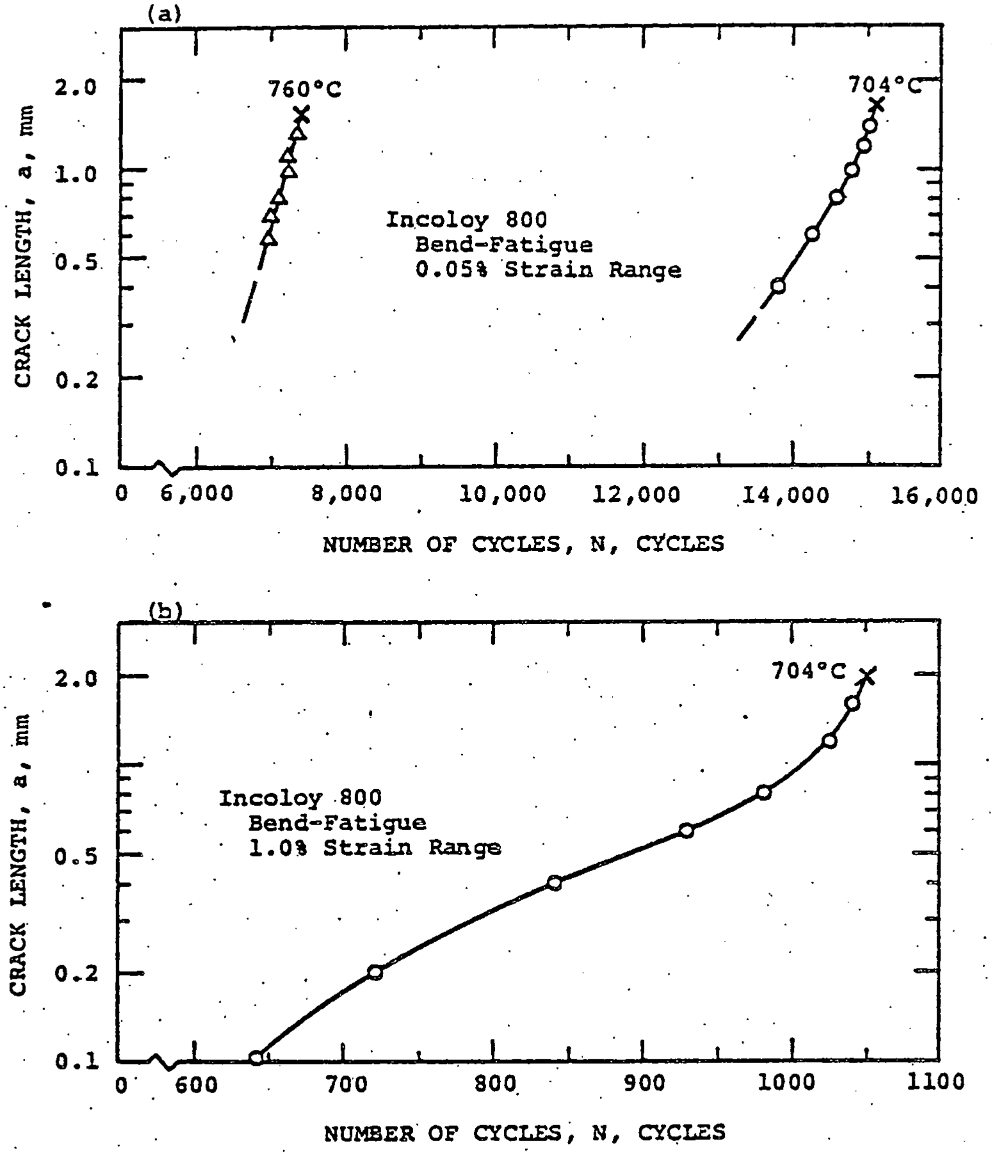

Figure 7.5 Crack Length vs. Number of Cycles for Incoloy 800 Bend Specimens at (a) 0.5% Strain Range, (b) 1.0% Strain Range, and (c) 2.0% Strain Range.

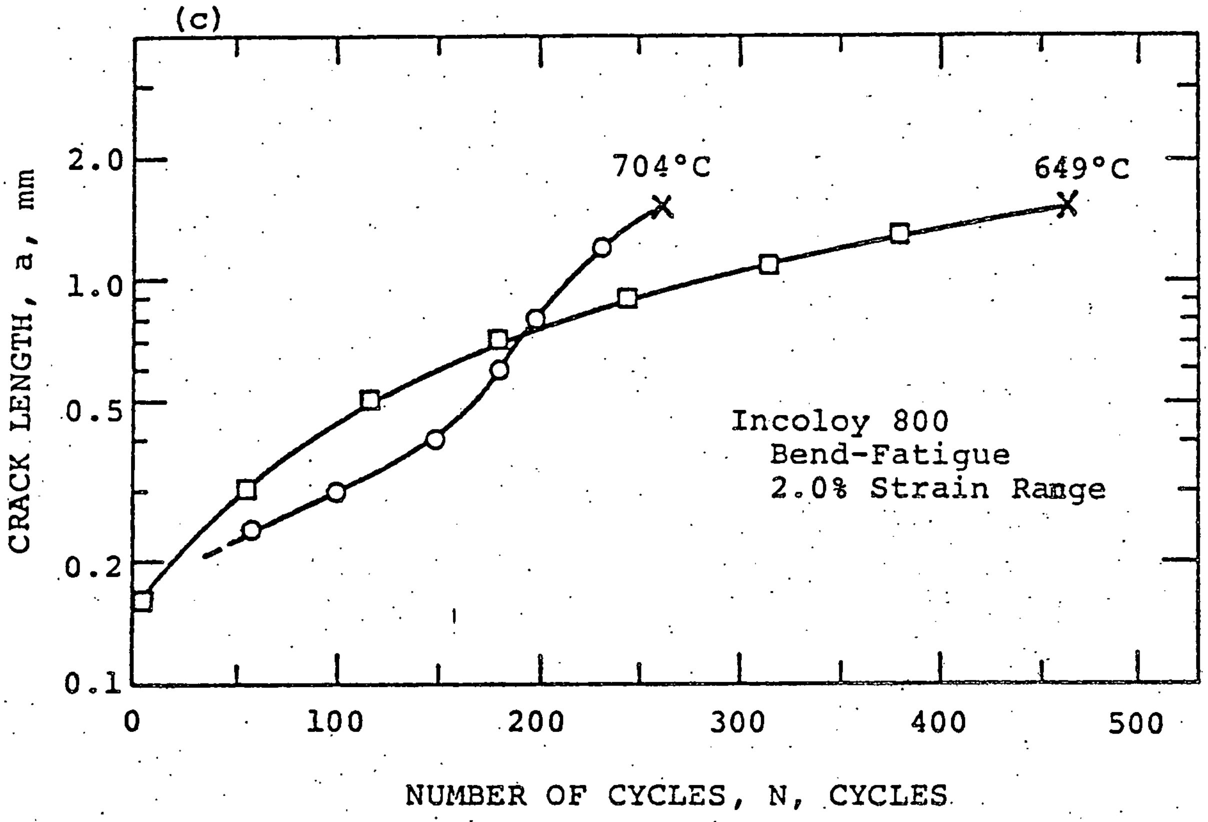

Figure 7.5 (Continued)

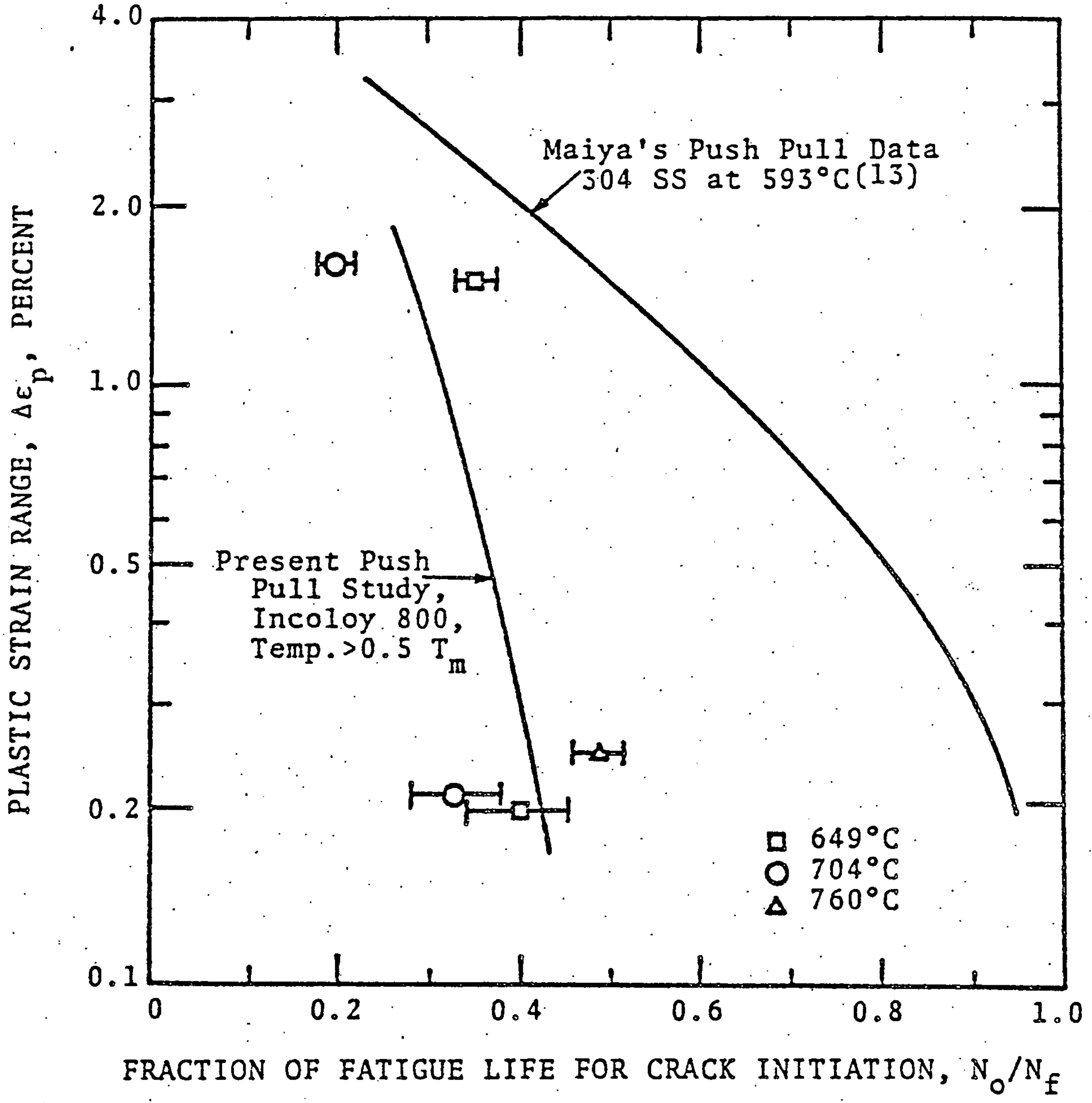

Figure 7.6 Plastic Strain Range vs. Fraction of Fatigue Life for Crack Initiation, Assuming an Initial Crack Length of 0.1 mm.

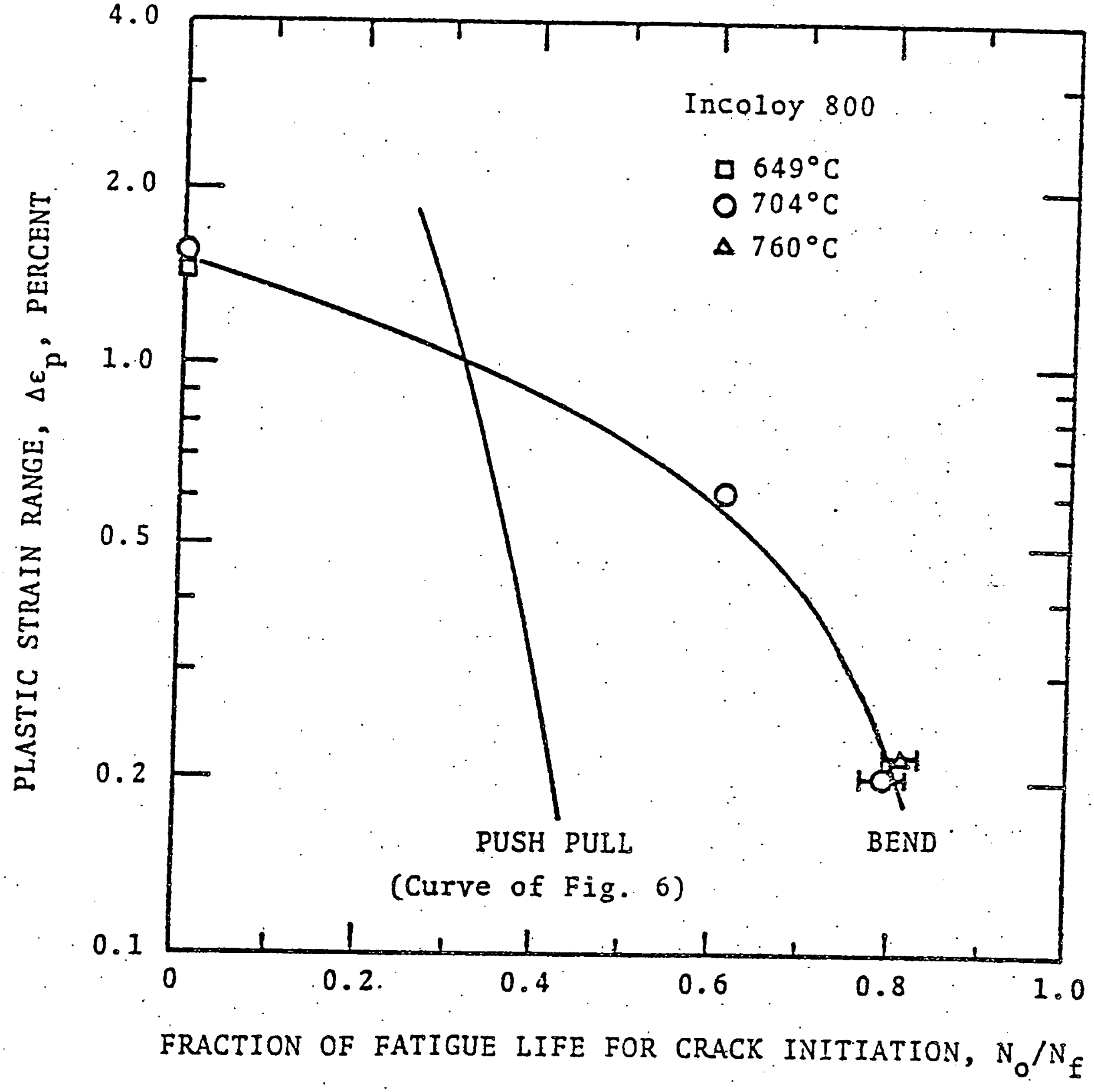

Figure 7.7 Plastic Strain Range vs. Fraction of Fatigue Life for Crack Initiation for Incoloy 800, Assuming an Initial Crack Length of 0.1 mm.

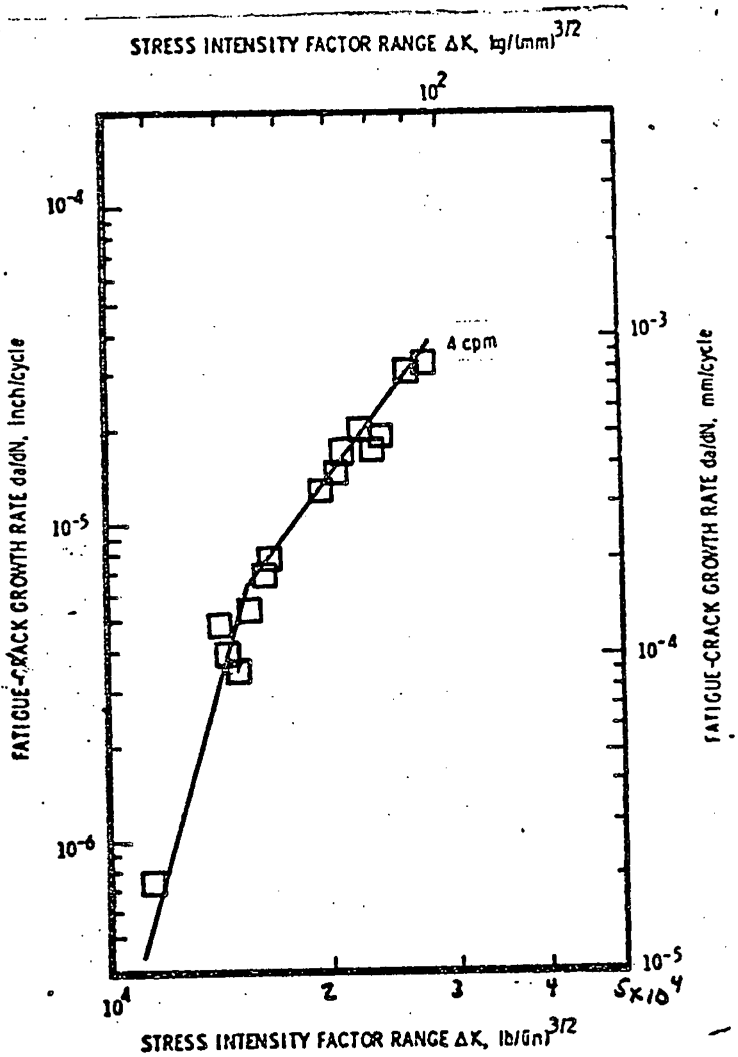

Figure 7.8 The Effect of Frequency on the Crack Growth Behavior of Solution-Annealed Type 304 Stainless Steel at 1000 F.

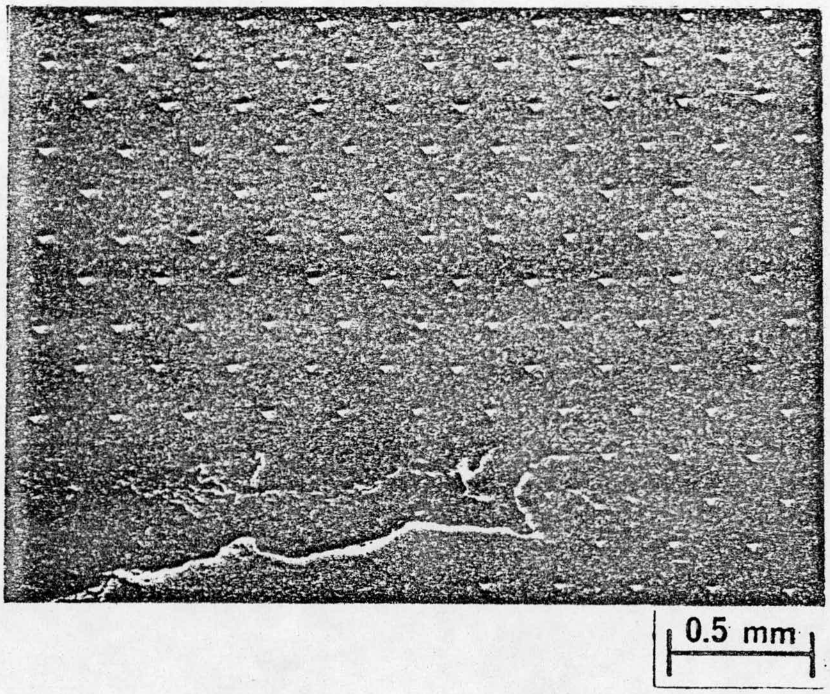

Figure 7.9 Micro-Hardness indents (DPH, 200 gm.) near the crack tip of a 304 SS specimen used for elevated temperature fatigue crack growth study.

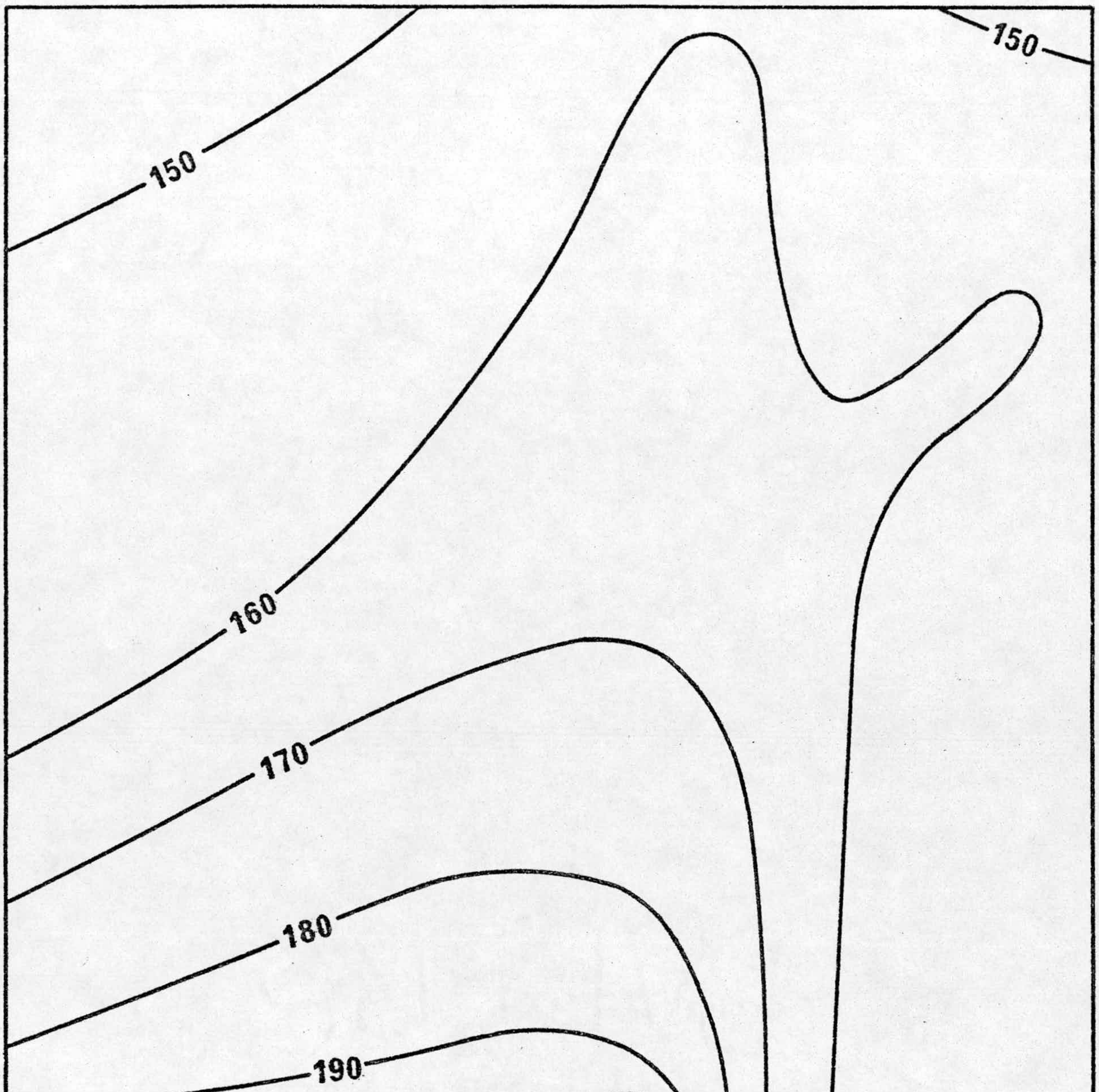

FIGURE 7.10 Room Temperature Hardness (Kg/mm^2) Contours in the Vicinity of a Crack Tip of 304 SS.

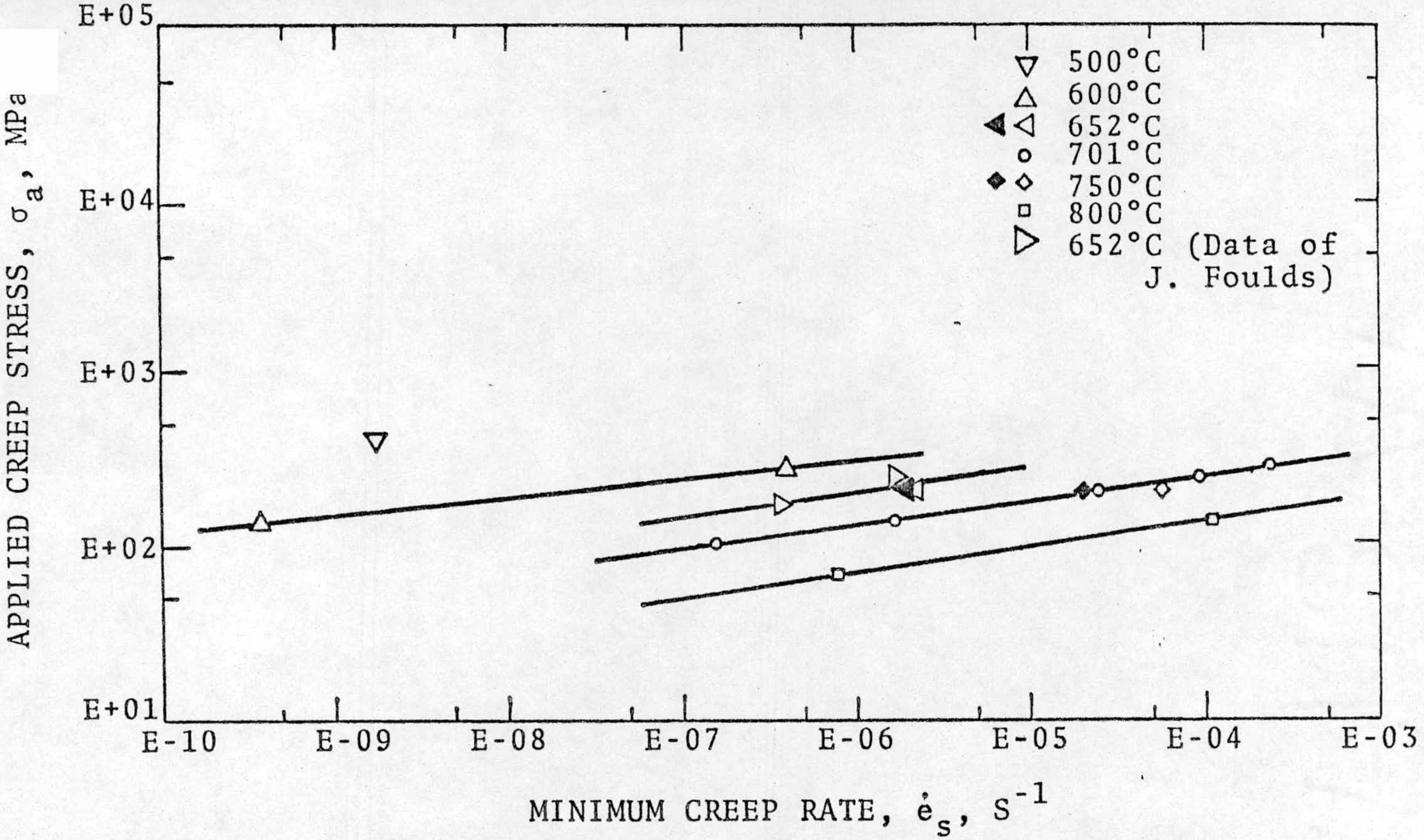

Figure 7.11 Log Applied Creep Stress versus Log Minimum Creep Rate for A.I.S.I. 330 Stainless Steel Crept at Various Temperatures. Pre-test solution heat treatments: 1100°C, 1800_s, 1.33 E-03 Pa, fast furnace cool, (open symbols) or 1100°C, 1800_s, 1.33 E-03 Pa, water quench (closed symbols).

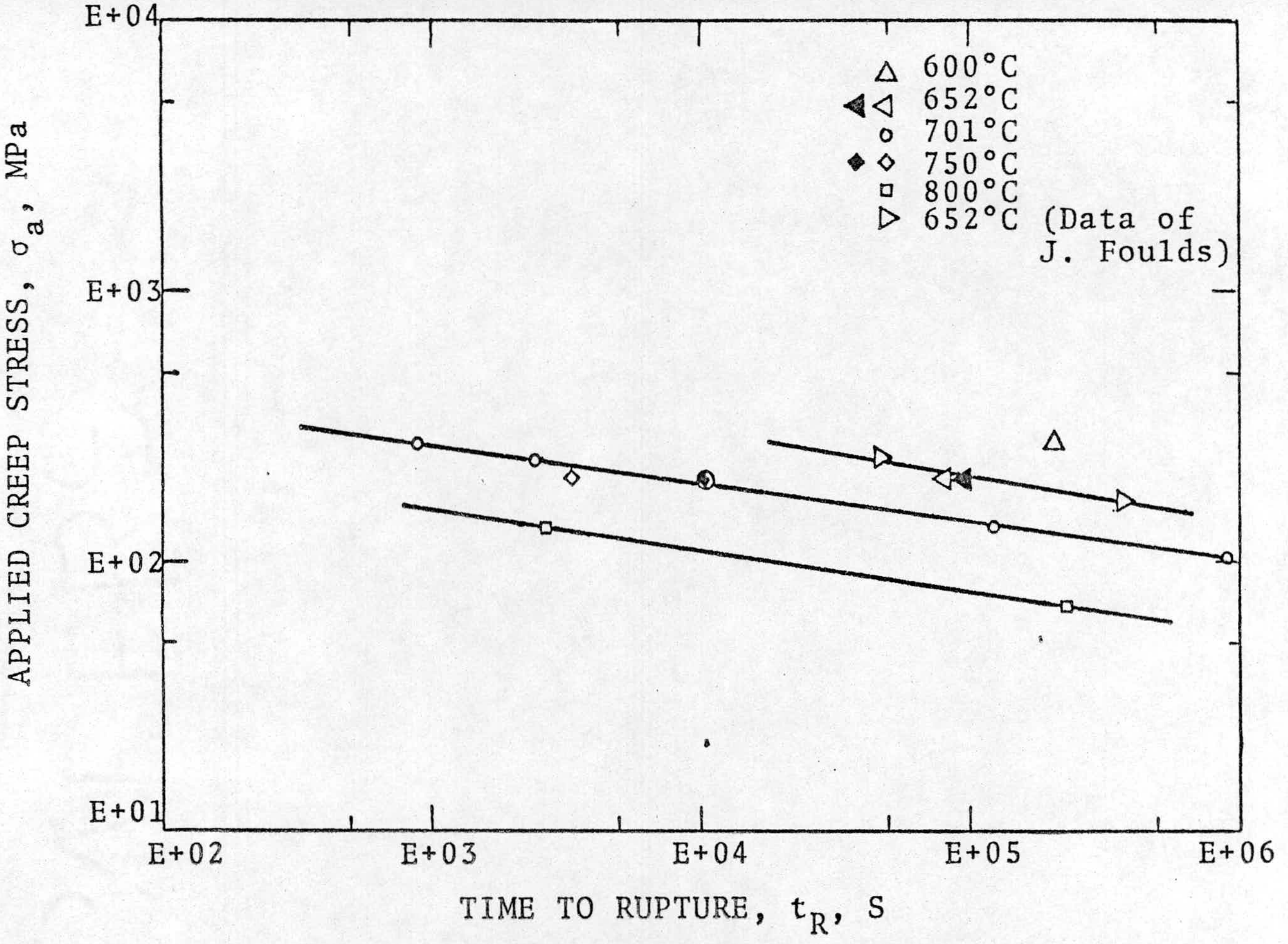

Figure 7.12 Log Applied Creep Stress versus Log Time to Rupture for A.I.S.I. 330 Stainless Steel Crept at Various Temperatures. Pre-test solution heat treatments: 1100°C, 1800_s, 1.33 E-03 Pa, fast furnace cool (open symbols) or 1100°C, 1800_s, 1.33 E-03 Pa, water quench (closed symbols).

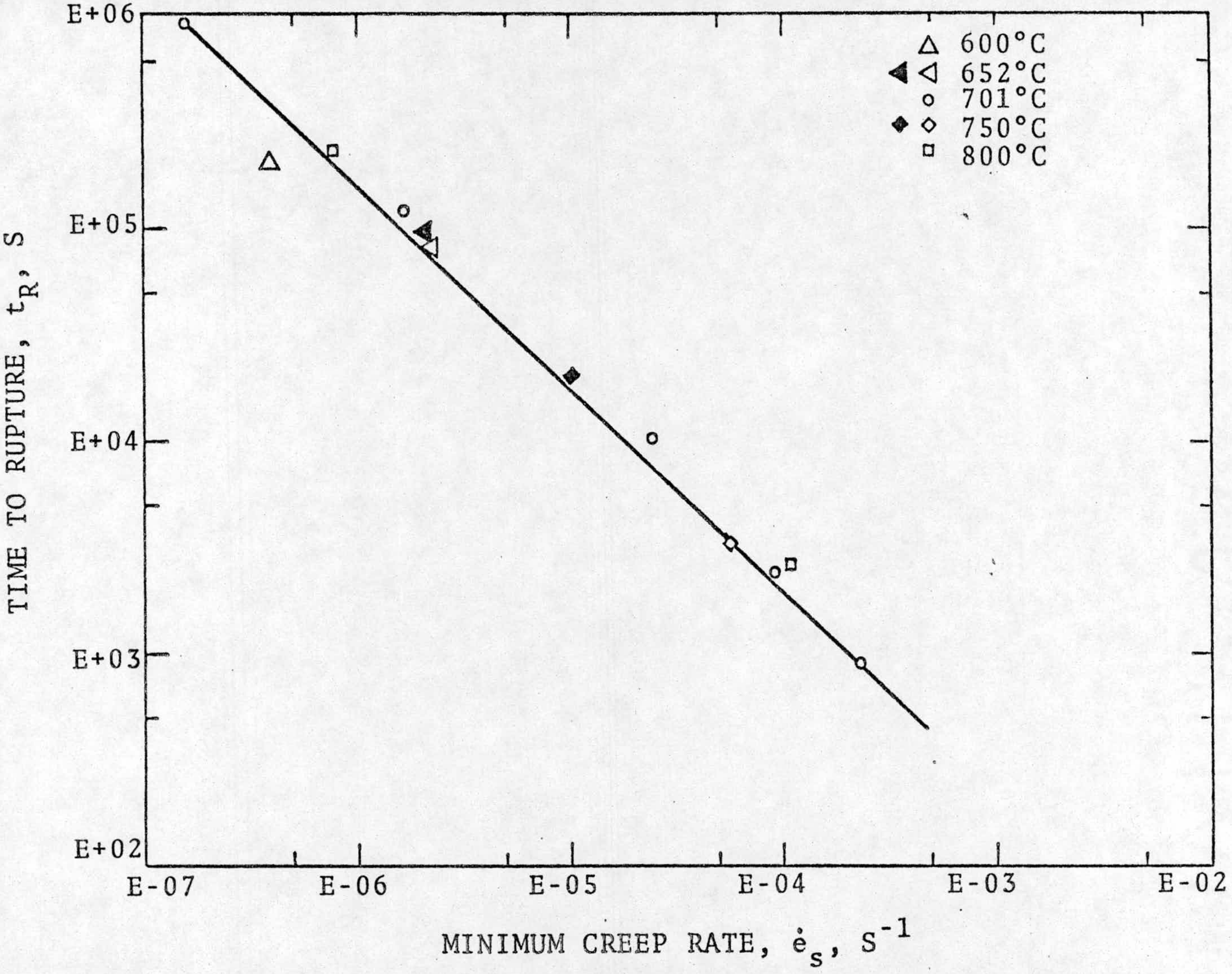

Figure 7.13 Log Time to Rupture versus Log Minimum Creep Rate for A.I.S.I. 300 Stainless Steel Crept at Various Temperatures. Pre-test solution heat treatment: 1100°C, 1800_s, 1.33 E-03 Pa, fast furnace cool (open symbols) or 1100°C, 1800_s, 1.33 E-03 Pa, water quench (closed symbols).

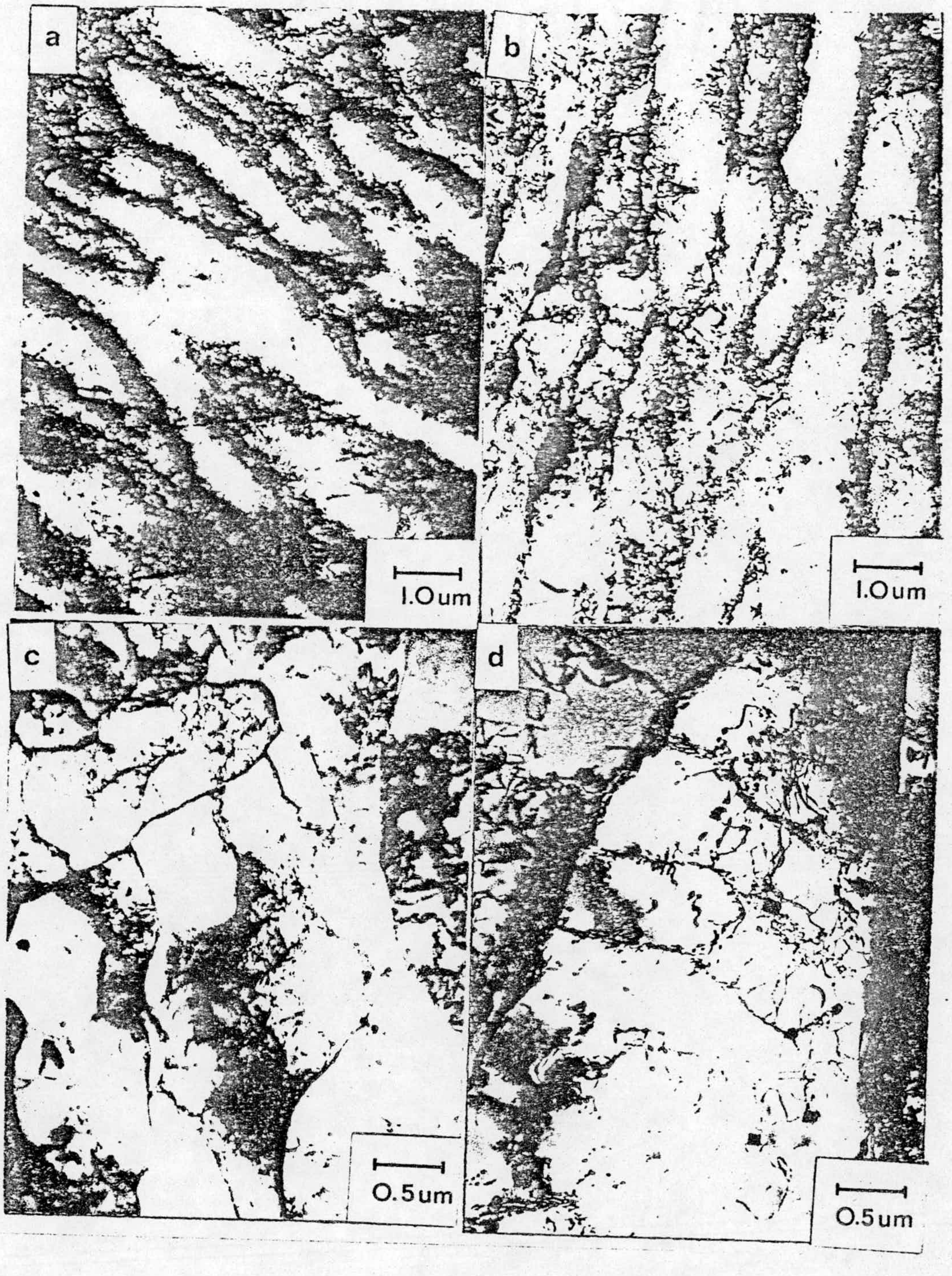

igure 7.14 Representative Micrographs of Substructures Developed During Creep-Rupture of A.I.S.I. 330 Stainless Steel Crept at 701 C at Various Stresses. a) 241.3 MPa b) 206.8 MPa c),d) 137.9 MPa.

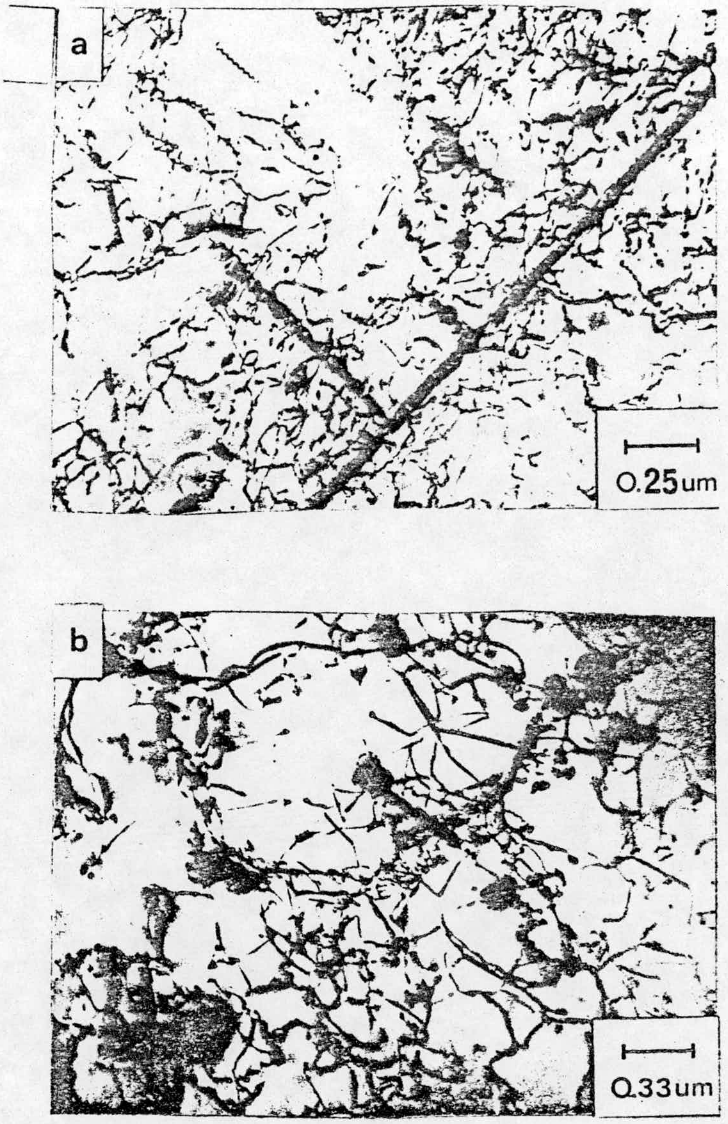

Figure 7.15 Mobile Dislocation Structure and Precipitate Morphology in A.I.S.I. 300 Stainless Steel Crept at 701 C for Two Stresses. a) 241.3 MPa b) 103.4 MPa.

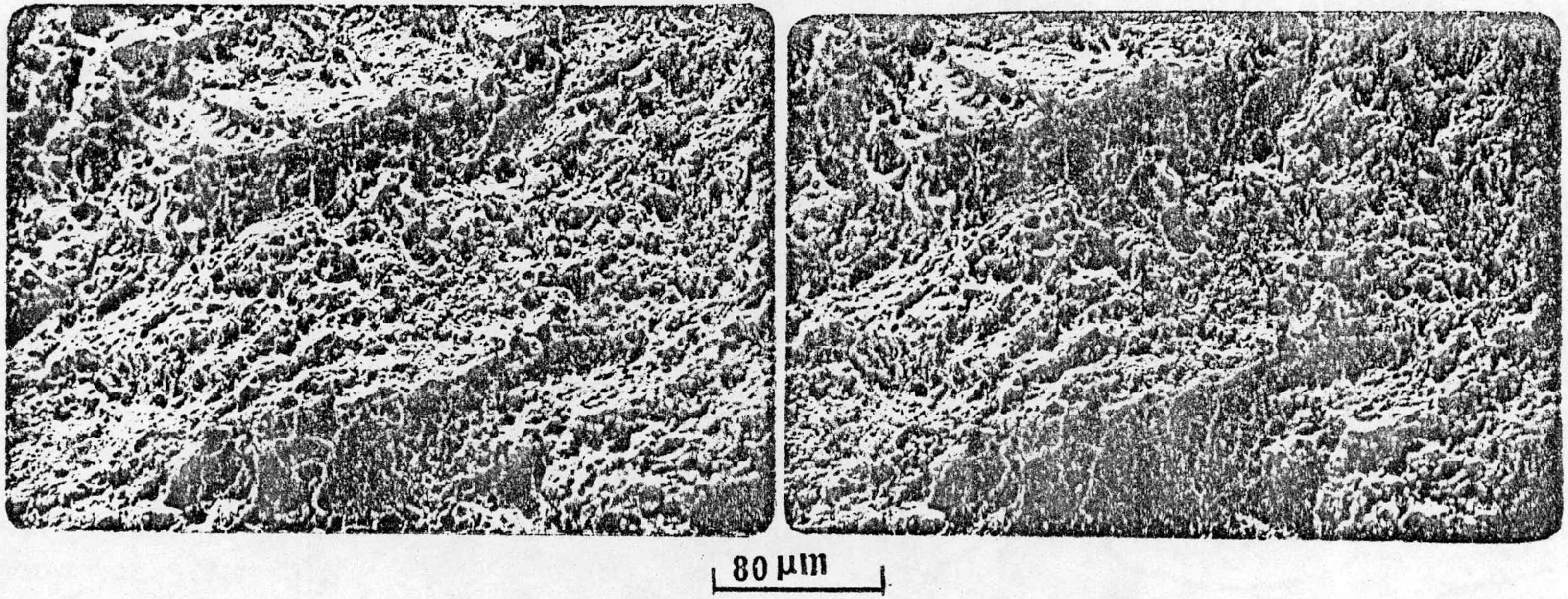

Figure 7.16 SEM fractographic stereo pair of A.I.S.I. 330 Stainless Steel specimen tested at 652°C and 172.4 MPa (25 ksi).

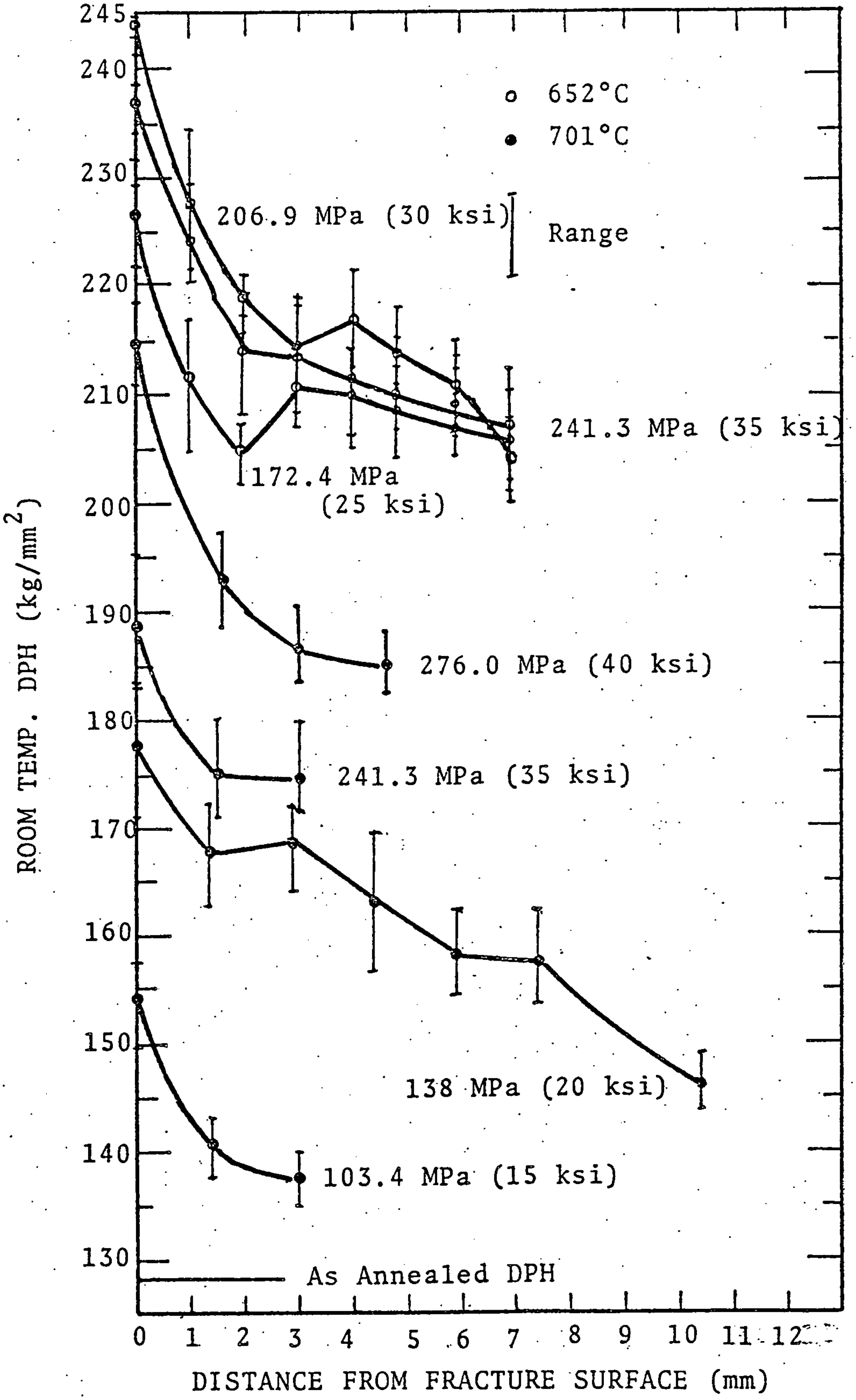

gure 7.17 Room temperature microhardness as a function of distance from the fracture surface for various applied stresses at 652°C and 701°C.